Title
Image-Based Modeling of Bridges and Its Applications to Evaluating Resiliency of Transportation Networks

Author
Cetiner, Barbaros

Publication Date
2020

Peer reviewed|Thesis/dissertation

UNIVERSITY OF CALIFORNIA

Los Angeles

Image-Based Modeling of Bridges and Its Applications to Evaluating Resiliency of Transportation Networks

A dissertation submitted in partial satisfaction
of the requirements for the degree
Doctor of Philosophy in Civil and Environmental Engineering

by

Barbaros Cetiner

2020

ABSTRACT OF THE DISSERTATION

Image-Based Modeling of Bridges and Its Applications to Evaluating Resiliency of Transportation Networks

by

Barbaros Cetiner
Doctor of Philosophy in Civil and Environmental Engineering
University of California, Los Angeles, 2020
Professor Ertugrul Taciroglu, Chair

Modern urban areas are heavily dependent on transportation networks to sustain their economic life. Hence, when vital components of a regional network are disrupted, economic losses are inevitable. As evidenced by 1989, Loma Prieta, and 1994, Northridge earthquakes, the seismic damages experienced by bridges alone result in extensive traffic delays and rerouting, not only hindering emergency response but also causing indirect economic losses that far surpass the direct cost of damage to infrastructure. Nevertheless, in many areas of the U.S., transportation networks lack the resilience required to sustain the potential demands of natural hazards.

Traditional hazard assessment methods, in theory, provide the tools required for predicting the vulnerabilities associated with natural hazards. Nonetheless, due to their abstractions of the complex infrastructure and the coupled regional behavior, they often fall short of that expectation. This study proposes a semi-automated image-based model generation framework for producing structure-specific models and fragility functions of bridges. The framework effectively fuses geometric and semantic information extracted from Google Street View images with centerline curve geometry, surface topology, and various relevant metadata to construct extremely accurate geometric representations of bridges. Then, using class statistics available in the literature for bridge structural properties, the framework

generates structural models. Both the performance of the geometry extraction procedure and the structural modeling method proposed here are validated by comparison against the structural model of a real-life bridge developed based on as-built drawings.

In principle, these models can be utilized to assess physical damage for any type of hazard, but in this study, the focus is limited to seismic applications. Thus to relate the damage resulting from seismic demands from ground shaking, bridge-specific fragility functions are developed for 100 bridge structures in the immediate surroundings of Ports of Los Angeles and Long Beach. Using these fragility curves, the physical damage resulting from a magnitude 7.3 scenario earthquake on Palos Verdes fault is predicted. Subsequently, the effects of the bridge infrastructure damage to the transportation patterns in the Los Angeles metropolitan area are investigated in terms of various resilience metrics.

The dissertation of Barbaros Cetiner is approved.

Jonathan P. Stewart

Yousef Bozorgnia

Jr DeShazo

Ertugrul Taciroglu, Committee Chair

University of California, Los Angeles

2020

To my beloved Jaclyn, dearest sister, and devoted mom ...

without you, I could never become who I am today.

TABLE OF CONTENTS

LIST OF FIGURES

LIST OF TABLES

VITA

2008	B.S. in Civil Engineering, Istanbul Technical University, Turkey.
2008	B.S. in Civil and Environmental Engineering, State University of New York at Buffalo, New York, USA.
2013	M.S. in Earthquake Engineering, Bogazici University, Turkey.
2014	M.S. in Civil and Environmental Engineering, University of California, Los Angeles, California, USA.
2014–present	Ph.D. Candidate in Civil and Environmental Engineering, University of California, Los Angeles, California, USA.

PUBLICATIONS

B. Cetiner, E. Koc, A. Rose, L. Soibelman, E. Taciroglu, and D. Wei. CRAFT: Comprehensive Resilience Assessment for Transportation Systems in Metropolitan Areas. *Advanced Engineering Informatics* (In Review)

D. Feng, B. Cetiner, M. Kakavand, and E. Taciroglu. A Data-Driven Approach to Predict the Plastic Hinge Length of Reinforced Concrete Columns and Its Application. *Journal of Structural Engineering* (In Review)

Y. Xu, X. Lu, B. Cetiner, and E. Taciroglu. A Real-time Long Short-Term Memory Framework for Regional Seismic Damage Assessment. *Computer-Aided Civil & Infrastructure Engineering* (In Review)

CHAPTER 1

Introduction

1.1 Background

1.1.1 Post-Disaster Functionality of Engineering Systems

Quantifying the effects of natural hazards on engineering systems has long been the focus of civil engineers. As a result of this continued attention, considerable research has been performed in developing methods to simulate the engineering demands caused by natural hazards, as well as establishing modeling techniques required for accurate representations of the capacity of civil engineering systems.

In earthquake engineering, three developments have been crucial. Probabilistic seismic hazard maps created an effective way of summarizing in detail the expected earthquake shaking based on region-specific geologic and seismic information (e.g., United States National Seismic Hazard Maps [69]). Comprehensive ground motion databases, such as NGA West2 Database [4], provided earthquake engineers with extensive catalogs of recorded seismic waveforms for use in simulating expected earthquake loading. Lastly, the performance-based earthquake engineering (PBEE) methodology [60] created a way to incorporate seismic hazard, system response, component-level damage, and system-level decision variables with explicit consideration to their uncertainties.

For characterizing tsunami hazard, tsunami propagation procedures, such as the National Oceanic and Atmospheric Administration (NOAA)'s Method of Splitting Tsunamis (MOST) [91], have been widely instrumental. Tsunami propagation methods enabled calculation of the hydrodynamic forces resulting from tsunami-induced inundation by determining the

tsunami height and horizontal components of tsunami wave velocity. Then, to define the tsunami demands, depending on the desired level of refinement, these hydrodynamic forces are modeled as wave patterns in three dimensions or static lateral loads [5].

For identifying the wind-borne hurricane hazards, storm track simulation methods coupled with wind field and gust factor models have been of critical importance. The hurricane demands on individual elements of a structure are identified using the pressure fields calculated from these simulations for multiple return periods of interest.

One thing common to the procedures mentioned above is that they all offer means of determining the demands anticipated on engineering systems for distinct hazard types. Demands, however, are just one of the two high-level inputs required for assessing the response of structural or geotechnical systems to natural hazards. Assessing the ability of a system to resist demands from relevant hazards requires comparing its capacity against the corresponding demands. Based on the complexity of the hazard input, a system's capacity is quantified through models as simple as linear elastic or as intricate as complex nonlinear representations. As long as accurate information on the system's geometric and material properties exists, appropriate models can be established, and the system capacity can be calculated with minimal uncertainty.

This process is equally applicable to evaluating the performance of individual systems or entire regions comprised of a large number of distinct systems. Nonetheless, traditionally, at the level of detail specified earlier, it has been mainly utilized for single systems. On a regional scale, only simplistic implementations of the discussed principles were performed. Expectedly, as a consequence of their rather crude consideration of either the hazard, physical inventory, or both, they result in predictions far from reliable (see, for instance, the study by Kircher et al. [46]). However, in reality, the post-disaster functionality of an engineering system is remarkably dependent on the systems surrounding it. For instance, in densely urbanized areas, the seismic demands on a building can be considerably altered by the interactions of the neighboring structures with the free-field motion [41]—likewise, the arrangement of structures surrounding a building can largely influence the wind load

demands on that building [45].

Most of the preceding discussion assumes that the key determinant of a system's functionality is physical damage. If functionality is perceived from a broader perspective as a system's ability to perform as intended and any reductions to it are tied to macro-level metrics such as economic losses, then shifting from the individual- to regional-level assessments becomes even more critical in evaluating post-disaster performance. After a natural hazard, the capability of an engineering system to restore its operations in full is linked to the infrastructure serving it. In other words, if the objective is to determine the high-level impacts of disasters, a greater extent of interconnectedness exists between engineering systems, and this dependence can be hardly ignored. Modern-day examples supporting this understanding are countless. The annual direct cost of damage to power lines, utility poles, and transmission towers due to hurricanes or other extreme weather events is estimated at around tens to hundreds of millions of dollars [104]. However, according to Campbell [16], the annual cost of power outages resulting from these physical damages is estimated somewhere between 25 to 70 billion USD. Electrical grids consist of a large number of interdependent elements. Even damage to a small fraction of their elements may result in notable reductions to functionality at the network level. As a result, considerable downstream economic losses may be incurred. A somewhat less obvious example is how the performance of port facilities is highly reliant on the functionality of the infrastructure serving them. The property losses due to the 1995 Hanshin-Awaji (Kobe), Japan earthquake is estimated at 100 billion USD [36]. The earthquake devastated Kobe's infrastructure in large, yet the damages to its container port (then the world's sixth-largest) were particularly critical. The business interruptions caused by the facilities' downtime and the decline in their accessibility is believed to result in total losses on the order of 200 billion USD [20]. In the case of cargo ports, the number of goods that can be conveyed through the facilities is affected by the functionality of connecting infrastructure, and the port itself. Hence, in evaluating the effects of potential hazards to a port, if assessments of damage are limited to individual elements alone, results would have a minimal resemblance to the actual consequences. A similar situation was observed in 2005,

in the aftermath of Hurricane Katrina, one of the costliest natural disasters in the history of the United States. The total losses due to the hurricane are believed to be around 200 billion USD [23], while the associated property damage is approximately 96 billion USD [105]. Katrina flooded most of New Orleans, incapacitated a remarkable portion of its infrastructure, and crippled almost the entire area. A direct result of the widespread decline in infrastructure functionality was economic losses that far exceeded the costs required to prevent these functionality decreases. For instance, after the hurricane, many of the high rise buildings in Downtown New Orleans remained unscathed from wind and flood hazards [26]. Still, they could not be used because the utility and transportation infrastructure that they depended on were barely operational.

In short, the post-disaster functionality of an engineering system is highly dependent on the infrastructure surrounding it. Consequently, in evaluating the potential impacts of naturals hazards on a system regional-level interactions must be considered to attain accurate results incorporating limited uncertainty. Implementations at regional-level, nevertheless, command an added level of complexity both from the computational and modeling aspects. While the computational requirements of regional-level considerations are largely satisfied with the wide availability of web-based high-performance computing platforms—e.g., NSF's Natural Hazards Engineering Research Infrastructure (NHERI) cyberinfrastructure [78], Google Cloud Platform, etc.—the modeling front mostly remains in its infancy. There is a lack of dependable inventory data at the regional level. Hence, for representing capacity, the existing methods heavily rely on abstractions of the archetype system classifications based on public-domain metadata (see, for instance, HAZUS [25], PAGER [99], etc.).

1.1.2 Beyond Archtype Classifications: Existing 3-D Reconstruction Methods

Recent advancements in point cloud-based modeling offer a promising alternative to the traditional archetype-based representations of engineering systems. Although these developments are mainly limited to geometry extraction, they still constitute a critical step towards

collectively establishing the regional-scale inventories required for detailed modeling.

Point clouds obtained from Light Detection and Ranging (LIDAR) sensors and imagery, via structure from motion (SfM) [94] or semiglobal matching (SGM) stereo methods [35], are the two primary data sources for most 3-D reconstruction applications. Hence, for brevity, here, the algorithms and systems for producing 3D models at the regional scale are summarized for only these two input types.

At the highest level, 3D reconstruction using point clouds involves three principal steps: 1) preprocessing, 2) classification/segmentation, and 3) modeling. Preprocessing consists of the removal of outliers (Figure 1.1a) and noise (Figure 1.1b) from data. In LIDAR point clouds, the former of these two artifacts result from sensor imperfections, while the latter is due to occlusions in the captured scene (e.g., Figure 1.1c). Segmentation refers to the grouping of points into segments with shared characteristics (Figure 1.2b), whereas classification is the process of determining the labels of each segment according to a range of criteria (Figure 1.2c). In many 3D reconstruction applications, initial segmentation can be as simple as separating ground points from the points that belong to the above-ground objects using principal component analysis [37]. Similarly, the classification for such a setup can merely comprise establishing the labels for ground and above-ground (other) points. Lastly, modeling involves terrain generation by meshing of ground points, extraction of infrastructure elements through processes such as boundary extraction, shape fitting, and refinement (Figure 1.3).

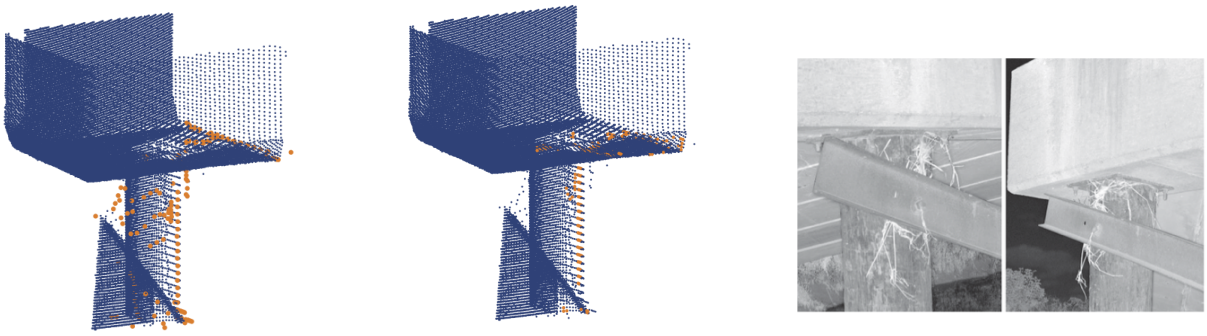

(a) Outliers (b) Noise (c) Occlusions

Figure 1.1: Point cloud data captured from a bridge bent. The outliers (a) and noise detected after preprocessing (b) are marked in orange. Vegetation that produced the noise is shown in (c) (Adapted from Walsh et al. [100]).

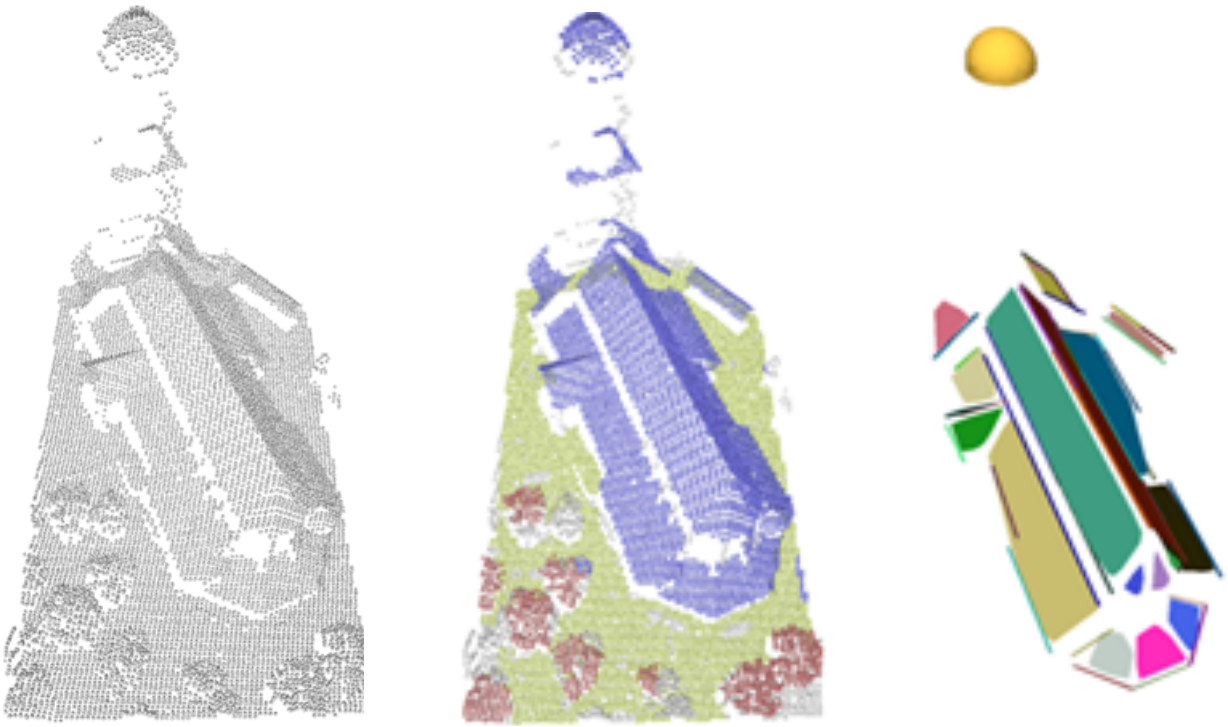

(a) Input (b) Classification (c) Segmentation

Figure 1.2: Point cloud data (a) after segmentation (b) and classification (c). In classification results, yellow, blue, red, and white colors denote ground, building, vegetation, and other points, respectively. (Adapted from Lafarge and Mallet [49]).

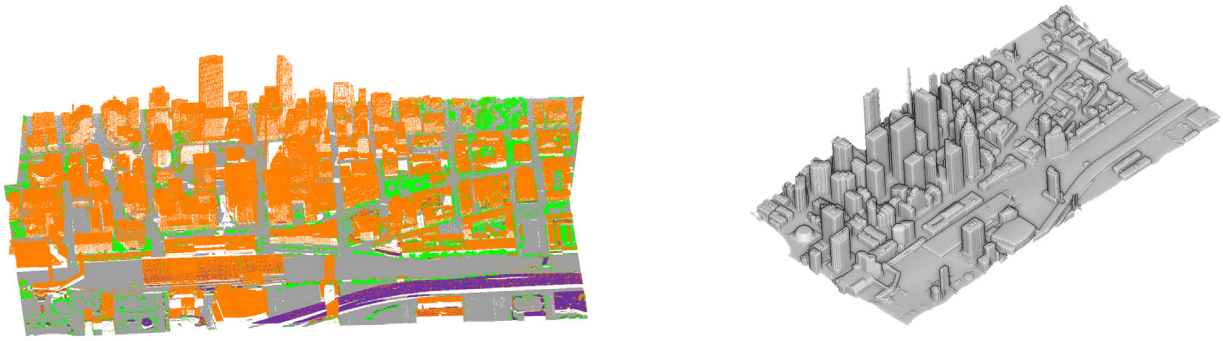

(a) Classification results

(b) 3-D urban model

Figure 1.3: Point cloud data for a section of Toronto, Canada after segmentation (a) and the corresponding urban reconstruction (b). In classification results, green, gray, purple, and orange colors signify vegetation, ground, bridge, and building points, respectively. (Adapted from Zhang et al. [109]).

The traditional approach in outlier filtering is to define a local outlier parameter based on statistics such as nearest-neighbor distance, local density [3], or eigenvalues of the local covariance matrix [101]. Then, by thresholding or making an assumption about the statistical distribution of this parameter, identifying and discarding the nonconforming points. With the growing popularity of machine learning methods, data-driven solutions similar to the deep learning model proposed by Rakotosaona et al. [75] are expected to become more prevalent in outlier filtering. Noise removal approaches also investigate the neighbourhood of each point at a local level, but the removal consists of a smoothing operation. Generally, to prevent over-smoothing sharp local features such as corners, etc., anisotropic filtering is preferred for noise removal. Filtering can be based on a number of parameters including mean curvature [50] and the normals of the points [102, 38]. L_0-minimization is another method that is found to work particularly well in denoising point sets with sharp features [89].

Point cloud segmentation is typically performed using model fitting-, region growing-, or clustering-based techniques. Most model fitting algorithms are powered by the basic principles of Hough Transform (HT) [29] or Random Sample Consensus (RANSAC) [9] methods.

HT is an effective way to extract planes [98], spheres, and cylinders [74] from point cloud data. RANSAC offers more possibilities for the extraction of parametrized geometric shapes, i.e., cylinders, spheres, cones, torus, planes, and cubes. Some popular modifications of RANSAC in the Point Cloud Library (PCL) [79] are the Progressive Sample and Consensus (PROSAC) [19], Maximum Likelihood Estimation Sample and Consensus (MLESAC), and M-estimator Sample and Consensus (MSAC) [92] methods. One of the primary advantages of model-fitting methods is that their segmentation quality is not significantly affected by the presence of outliers. Notwithstanding, model fitting algorithms are computationally demanding, and their performance is sensitive to data characteristics. Region-based algorithms are an alternative to model-based segmentation. The central idea of region-growing segmentation is identifying seed points in point cloud regions with distinct characteristics (such as point curvature and area of the local plane) and growing regions from those seeds based on various criteria (e.g., surface planarity and inter-point distances) [12]. The two-step segmentation procedure suggested by Ning et al. [64] and the voxel-based procedures by Wang and Tseng [103] and Ahn-Vu et al. [97] are some examples of the procedures that were successfully applied to urban environments. The main benefit of region-growing segmentation routines is that they are only nominally affected by noise. Nonetheless, their segmentation quality is dependent on the initial seeds (at the moment, no universally accepted standards exist for selection of seeds) and the accuracy of computed normals and curvatures of points (particularly complicated to correctly calculate near region boundaries.) Another segmentation approach is the clustering of point clouds based on their features using hierarchical or partitioning clustering. The hierarchical algorithms can be bottom-up (agglomerative) or top-down (divisive). The bottom-up algorithms assume that every individual data point in feature space is a separate cluster, then recursively joins data points within a certain distance threshold to the same clusters until the distance between clusters is higher than a prescribed threshold level. The top-down algorithms, on the other hand, start with the entire feature space, then successively splits the space into individual clusters until a certain number of clusters is attained. Partitioning methods do not involve aggregation or division of clusters; they iteratively move data points among a number of distinct clusters until the

greatest separation between the clusters is reached (e.g., k-means, mean-shift, spectral clustering). Many different attributes, including planarity [106], kernel density [21], eigenvalues, and eigenvectors of the graph Laplacian [48], height difference relative to neighboring points, unit normal vector [13], are used to define the feature space in clustering. Depending on the quality of the attributes included that make up the feature space, clustering methods can be quite robust and flexible. The primary limitation to clustering-based segmentation is that their computational performance is highly dependent on the point cloud density, generally requiring long computational times for dense sets.

Classification, also known as semantic segmentation, of point clouds is performed either through a model trained using a large annotated dataset (supervised approach), or automatically partitioned into segments obtained using an unsupervised approach, without the need for labeled datasets. Supervised classification techniques use a variety of procedures ranging from random field-based frameworks [84, 82, 63] to deep learning methods, with the latter approach generally yielding better accuracies. The first deep learning approach for point cloud classification, PointNet [73], is a fully-connected deep learning network that is capable of classification (as well as segmentation) of point clouds by operating on just the 3-D point coordinates. PointNet, by design, cannot capture local structures in the space of points, thus it extracts patterns with limited success. An improvement to PointNet, a deep learning procedure based on a hierarchical neural network called PointNet++ [72], rectifies this problem. Even after preprocessing, point clouds may include outliers and noise. These artifacts render the application of spatial convolutions particularly complicated. To address this issue, Hermosilla et al. [33] proposed a hierarchical deep learning approach that first represents the convolution kernel as a multilayer perceptron, then expresses the convolution as a Monte Carlo integration problem and subsequently uses Poisson disk sampling for hierarchical feature learning. PointCNN [51] applies convolutions on raw point cloud data by first utilizing a k-nearest neighbors procedure to find the local point neighborhoods. Then using a multilayer perceptron on the spatially local points, PointCNN constructs a transformation to weight and permute the input features. If trained with a sufficiently large

dataset, all of these deep learning methods are very effective in the classification of point cloud datasets. Currently, a vital impediment to their practical implementation is the lack of adequate, publicly available, high-quality training sets, and manual labeling of point clouds is both technically challenging and laborious. Current unsupervised classification techniques exclusively consist of end-to-end autoencoder neural networks. The basic premise of these procedures is that, while reconstructing point clouds whose parts have been randomly re-arranged, they learn from representations of the data that capture the semantic properties of the point set. The studies by Achlioptas et al. [2], Zamorski et al. [108], and Sauder and Sievers [81] are some examples of the autoencoder networks proposed for point cloud classification.

Once the point cloud is segmented and classified, 3-D models can be generated. Ground modeling for point clouds involves a rather standardized procedure. First, a smooth uniform grid is matched onto the ground points. Then, a height value is assigned to each cell based on the z values of the points within cell boundaries. With this approach, some cells in the uniform grid will be empty since, typically, the point cloud sampling for uneven objects is non-uniform. The height values for the empty cells are determined by performing membrane interpolation according to Laplace's equation, $\nabla^2 z = 0$, where the boundary conditions for an empty cell are defined using the nearest-neighbor non-empty cells. The boundaries of the ground points generally are not straight lines. Hence, as the last step in ground modeling, the uniform grid used for membrane interpolation is partitioned into a mesh of triangles via Delauney triangulation such that the boundary cells align with the desired bounds. In generating building models, the 2.5-D dual contouring method [111] is a widely accepted method, especially for point clouds generated from aerial surveys. The pipeline for 2.5-D dual contouring consists of a three-step tree structure process. First, the point cloud is overlaid with a uniform 2-D grid to form the lowest level of the auxiliary quadtree, and Hermite data samples are generated/estimated at grid points and edges. Second, in each quadtree, a hyperpoint that minimizes a 2.5-D quadratic error function is computed, and by adaptive geometry simplification, subtrees are collapsed and quadratic error for

each associated leaf cell is added. Subsequently, a watertight mesh model is obtained by connecting hyperpoints with surface and boundary polygons. Another group of techniques perform reconstruction based on segmentation results. The method by Sampath and Shan [80] intersects segmented patches and identifies the connectivity among the planar segments through an adjacency matrix to model buildings. Zhou and Neumann [110] carry out building modeling by first snapping the edges of segmented planes to principal directions, then joining the neighboring segments according to their spatial relationships. Yi et al. [107] determine the upward direction of each building, block-partitions point data aligned with it into a series of consecutive blocks, extract contours of each block, and trough operations, including extrusion, lofting, and sweeping combines these blocks to generate a model.

The focus of the processes discussed so far was on 3-D reconstruction from point cloud data, without making a distinction between the source of the input (i.e., LIDAR or imagery). Given most existing photogrammetric reconstruction techniques for modeling engineering systems first generate point clouds from collections of images then apply the techniques summarized above, such an approach is appropriate. These two data types are handled identically for modeling purposes. The primary difference between the reconstruction procedures for LIDAR and image data as a whole is that obtaining point cloud data from images requires an additional step of processing (point clouds are a direct output of LIDAR surveys). Structure from motion (SfM) [94] and semiglobal matching (SGM) stereo methods [35] are the two methods that were found to be reliable tools for generating point cloud data from image sets. The more popular of the two, SfM, consists of a four-step procedure. The first step of SfM involves extracting keypoints in each image using Scale Invariant Feature Transform (SIFT) object recognition algorithm [52]. In the second step, individual camera positions, orientations, focal lengths, and the links between keypoints detected in each image are established. Camera parameter detection step is performed using Bundle Adjustment [93], while feature matching is established using RANSAC. At the end of the second step, a sparse point cloud is obtained. Next, a denser point cloud and corresponding 3-D surfaces are produced using a Multiview Stereo Matching (MVS) algorithm. The point clouds obtained

subsequent to this step are defined in a metric coordinate system of arbitrary scale. These point clouds are registered to world coordinates by a series of rigid body transformations and linear scaling using the location information from image geotags.

The methods described above enable automated or semi-automated geometric reconstruction of engineering systems, opening up exciting new avenues for regional-level inventory development. Nonetheless, they share a standard limitation; they all require the manual collection of LIDAR or image data. Currently, performing LIDAR surveys is a time-consuming and costly task. Photogrammetric surveys are a low-cost alternative to LIDAR surveys, yet with the restrictions placed on flying unmanned aerial vehicles in dense urban areas, collecting image data at the regional scale is challenging. In short, scaling these methods to regional scales is problematic unless required datasets are already established, which is rarely the case aside from a few exceptions [24].

Several publicly available datasets that can satisfy the data need for regional studies exist. The author believes that the largest and the most extensive of these sets, Google Street View images, in particular, is a strong candidate for satisfying the data needs for regional studies. The existing literature on geometry reconstruction from Google Street View is scarce and so far concentrated on building modeling only. The seminal work on geometry extraction from Google Street View images by Micusik and Kosecka [59] made an attempt at recovering the building facades on a few building blocks by exclusively utilizing SfM methodology. The distinctive aspects of their study are the modeling of the camera setup as an omnidirectional camera, the execution of feature detection/matching step using the speeded up robust features (SURF) algorithm [10] and the use of superpixels for the MVS stage. Although the results were promising, the use of superpixels for dense matching was recognized to be a limitation at places that are not well described by local planar patches. In another study, Diaz and Arguello [22] proposed an algorithm to estimate building heights from Street View images. Using a central projection camera model, they developed height estimations based on camera height and vanishing points identified for each image. Their algorithm produced fairly accurate results whenever the ground line and crown line for a

building could be accurately identified. However, whenever their algorithm failed to detect one of these lines correctly, the height measurements were also highly affected. Lastly, Bruno and Roncella [15] applied SfM to Google Street View images converted to pinhole projection by using a spherical camera model and compared their results to ground truth measurements and found that Street View images yield reasonably accurate results.

1.2 Objectives and Scope

The objective of this study is to establish a comprehensive image-based method for semi-automated modeling of bridge structures. The proposed approach uses Google Street View images as well as several relevant metadata to generate geometric models of bridges. Then, by assigning structural properties based on class statistics available in the literature, the method converts geometric objects into structural models. Here, all of the critical steps of this process are defined in detail. Furthermore, the developed methodology is verified through geometric and structural performance comparisons to a real-life bridge.

Although the models generated through this approach can be employed for various applications (for instance, if coupled with video-based vibration data, system identification of bridges is possible) and different hazard types (e.g., tsunami and flood), the focus of this study will be the role of the developed models in regional-scale seismic assessments and resilience. To this end, image-based models of bridges in the immediate surroundings of the Ports of Los Angeles and Long Beach are modeled, and their fragility functions were developed for the five damage states defined in the PBEE methodology. These fragility curves were then coupled with the ground shaking intensities resulting from a M_w 7.3 scenario earthquake on the Palos Verdes fault to assess the physical damage to the transportation network surrounding the port complex. Next, the physical damage results were combined with a regional scale transportation network analysis to test the resilience of the Los Angeles metropolitan area. The intermediate and final results of the performed analyses are presented.

1.3 Organization of This Document

Chapter 2 explains the structural modeling procedures utilized to compute bridge fragility functions. Chapter 3 provides an in-depth discussion of the seismic assessment and resilience framework proposed in this study. Chapter 4 describes in detail the case study performed for the Ports of Los Angeles and Long Beach. Chapter 5 draws conclusions from the performed investigation and offers a summary of the future directions for this work.

CHAPTER 2

Structural Modeling of Bridges for Fragility Calculations

2.1 Overview

The algorithms described in the previous chapter form the backbone of the image-based geometric modeling procedures. However, these models alone are not useful for civil engineering applications; they need to be populated with appropriate structural information to obtain structural models. This chapter first describes the material and component models, as well as the mass and damping calculation procedures utilized to establish the bridge structural models. The ability of these modeling procedures to satisfactorily capture bridge response is dependent on the quality of the modeling properties used in defining the structural models. In determining appropriate modeling parameters, the author strongly benefited from the existing literature, in specific [55]; hence these findings are briefly discussed. Particularly when modeling uncertainties are explicitly considered, defining the connection between seismic demands and structural damage is most easily established through fragility functions. Hence, lastly, the procedure utilized for calculating fragility curves at an individual bridge level is discussed.

The bridges considered consist of reinforced concrete structures with prestressed concrete decks supported by seat, diaphragm, or cantilever abutments. Most long-span bridges also incorporate in-span hinges. All of these details are explicitly considered in obtaining structural models from image-based geometric models.

The primary motivation behind this research is to develop a set of tools that can be

easily applied to regional studies. For this purpose, a program that automatically generates structural models from the geometric information was devised. The program exclusively uses OpenSees [57]. Although the details of the program are not discussed here, when appropriate, reference is made to OpenSees commands specific to the performed implementation.

2.2 Material Models

2.2.1 Column Concrete

In defining the stress-strain behavior of core and cover concrete, the concrete model proposed by Mander et al. [54] is used. The confined and unconfined concrete is defined in OpenSees using Popovics concrete with degraded linear unloading/reloading stiffness [70],[42], `Concrete04`, and linear tension softening concrete material, `Concrete02`. Following Caltrans Seismic Design Criteria (SDC) [65], for the unconfined (cover) concrete, the ultimate stress f'_{co}, corresponding compressive strain ε'_{co}, and the ultimate strain ε'_{sp} values are defined as equal to the expected compressive strength of unconfined concrete f'_{ce}, 0.002, and 0.005, respectively, where

$$f'_{ce} = \max\left(1.3f'_c, 5000\text{psi}\right) \tag{2.1}$$

given f'_c denotes the specified compressive strength of unconfined concrete.

The ultimate stress of the confined concrete is determined using the relationship

$$f'_{cc} = f'_{co}\left(-1.254 + 2.254\sqrt{1 + \frac{7.94f'_l}{f'_{co}}} - 2\frac{f'_l}{f'_{co}}\right) \tag{2.2}$$

The equation that defines the effective lateral confining pressure on concrete f'_l is determined by the shape of the cross section. For circular sections with hoop- or spiral-type transverse reinforcement,

$$f'_l = \frac{1}{2}k_e\rho_s f_{yh} \tag{2.3}$$

where ρ_s signifies the ratio of volume of transverse confining steel to volume of confined (core) concrete, f_{yh} denotes the yield strength of transverse reinforcement, and k_e is the

confinement effectiveness coefficient. ρ_s is defined in terms of transverse reinforcement area A_{sp}, transverse reinforcement diameter d_b, and center-to-center spacing (pitch) of transverse reinforcement s as $\rho_s = 4A_{sp}/d_s s$. The confinement effectiveness for circular sections confined by circular hoops is determined as

$$k_e = \frac{\left(1 - \frac{s'}{2d_s}\right)^2}{1 - \rho_{cc}} \tag{2.4}$$

Similarly, the confinement effectiveness for sections confined by circular spirals is defined as

$$k_e = \frac{1 - \frac{s'}{2d_s}}{1 - \rho_{cc}} \tag{2.5}$$

where s', d_s, and ρ_{cc} denote clear spacing between hoops (or spiral), diameter of hoops (or spiral), and ratio of total longitudinal steel area to area of concrete core, respectively. Figure 2.1 outlines the geometric paramaters required for specifying the behavior of confined core in circular sections.

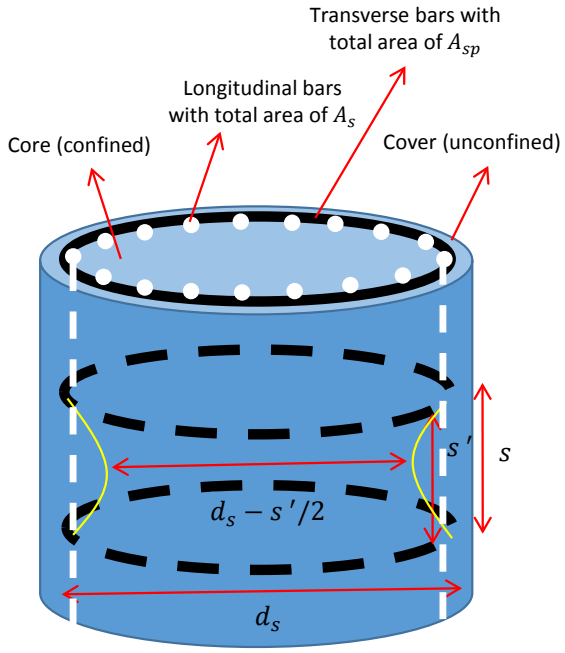

Figure 2.1: Geometric paramaters used in defining confined behavior for circular sections

For rectangular sections, due to potential differences in geometric configuration along the length (x-direction) and width (y-direction) of the section, a distinction is made in

calculating for calculating f_l' in x- and y-directions as

$$f_{lx}' = k_e \rho_x f_{yh} \tag{2.6}$$

$$f_{ly}' = k_e \rho_y f_{yh} \tag{2.7}$$

where ρ represents the total area of transverse bars running in the x- and y-directions, calculated as in terms of total areas of transverse reinforcement parallel to x- and y-axis A_{sx}, A_{sy}; center-to-center spacing of transverse reinforcement s; concrete core dimensions to center line of perimeter hoop in x- and y-directions b_c, d_c as

$$\rho_x = \frac{A_{sx}}{s d_c} \tag{2.8}$$

$$\rho_x = \frac{A_{sy}}{s b_c} \tag{2.9}$$

Note that $b_c \geq d_c$. The confinement effectiveness for rectangular sections is calculated using the relationship

$$k_e = \frac{\left(1 - \sum_{i=1}^{n} \frac{w_i'^2}{6 b_c d_c}\right)\left(1 - \frac{s'}{2 b_c}\right)\left(1 - \frac{s'}{2 d_c}\right)}{1 - \rho_{cc}} \tag{2.10}$$

where w_i is the ith clear transverse spacing between adjacent longitudinal bars, s' is the clear spacing between hoop bars and n is the number of transverse bars. Figure 2.2 displays the geometric paramaters defined in determining the confined concrete core behavior in rectangular sections.

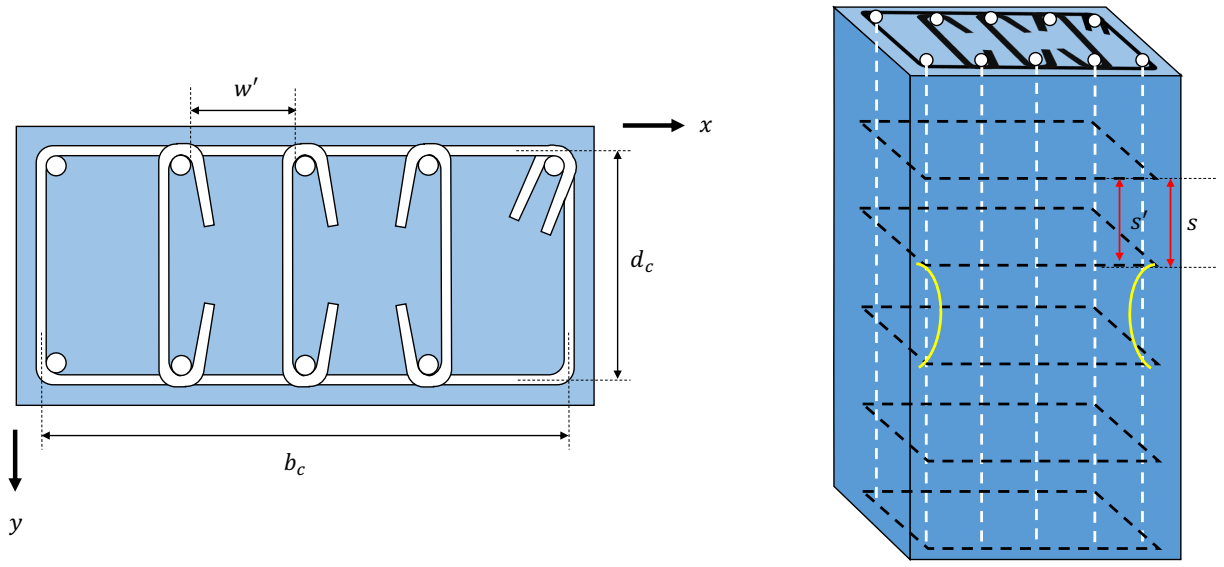

Figure 2.2: Geometric paramaters used in defining confined behavior for rectangular sections

The compressive strain at f'_{cc} is calculated using the relationship

$$\varepsilon_{cc} = \varepsilon_{co}\left[1 + 5\left(\frac{f'_{cc}}{f'_{co}} - 1\right)\right] \tag{2.11}$$

The compressive strain value where strain energy equilibrium between the concrete and the confinement steel is reached, i.e., ε_{cu}, is defined as 0.025.

Lastly,the modulus of elasticity for concrete is defined using the relationship

$$E_c = 33w^{1.5}\sqrt{f'_{ce}} \tag{2.12}$$

where w denotes the unit weight of concrete in lb/ft^3, and E_c and f'_{ce} are as previously defined, in units of psi. Furthermore, the shear modulus of concrete is calculated as

$$G_c = \frac{E_c}{2(1 + v_c)} \tag{2.13}$$

where $v_c = 0.2$. Figure 2.3 provides a summary of the characteristics specified for simulating concrete behavior.

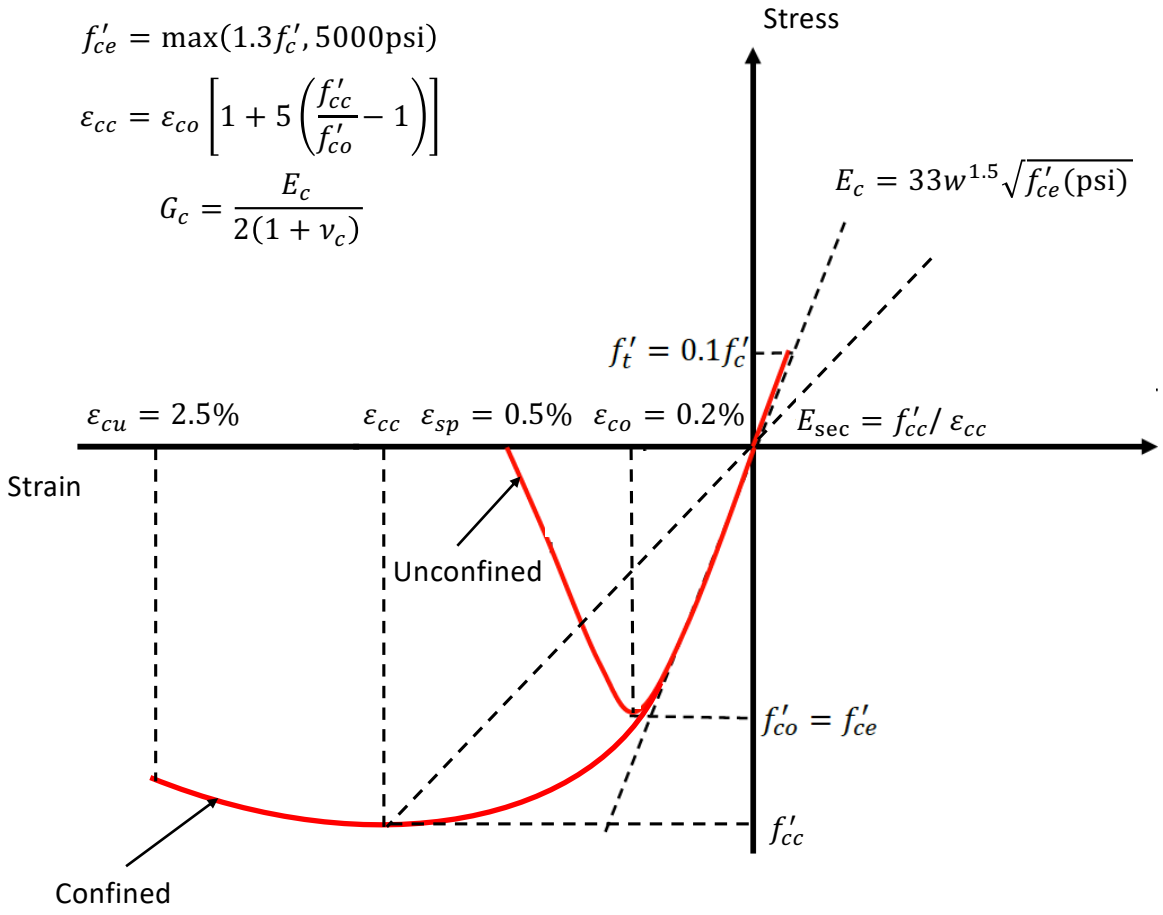

Figure 2.3: Material used in defining the concrete behavior

2.2.2 Steel Reinforcement

ASTM A706 Grade 60 steel reinforcement is used in modeling the reinforcement. The stress-strain behavior of Grade 60 steel is displayed in Figure 2.4. In OpenSees, this material is implemented using the Chang and Mander [18] uniaxial steel model, i.e., the `ReinforcingSteel` object.

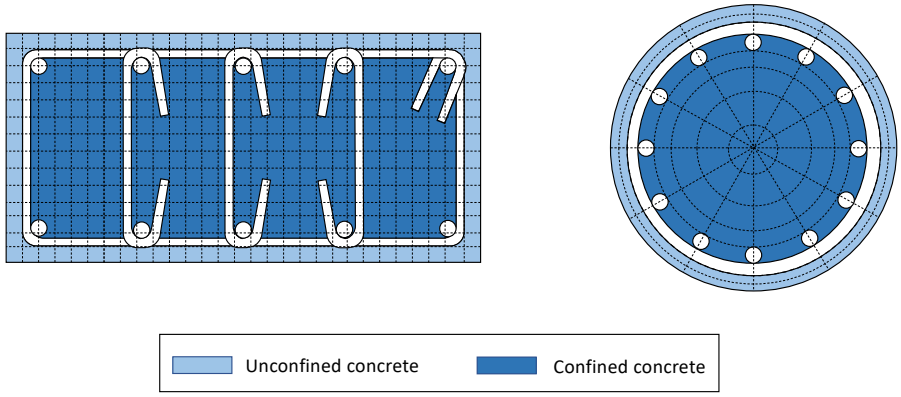

Figure 2.4: Stress-strain curve for the reinforcement steel

Table 2.1 shows the material properties for ASTM A706 Grade 60 steel. Other than the expected tensile strength f_{ue}, all material traits of the reinforcing steel are defined according to Caltrans SDC requirements. f_{ue} is randomly sampled from existing class statistics for California bridges as described in Model Properties.

2.3 Component Modeling

2.3.1 Columns

Columns are critical to the load-carrying capacity of bridge structures after an earthquake. Hence, carefully quantifying their performance is essential for accurate simulations of bridge behavior under earthquake excitations. Column seismic response is an aggregate of axial-flexural, shear, and torsional behavior; thus, considering each of these effects in detail is vital to estimate post-earthquake damage susceptibility of columns.

The axial-flexural behavior of columns is largely inelastic, where the levels of transverse reinforcement determine the extent of inelasticity. In this study, the inelastic column behavior due to flexural loading, spreading of plasticity across the column cross-section and length are computed using fiber sections where moment-curvature and axial force-deformation characteristics and their interaction are explicitly considered. For this purpose, each column is

Table 2.1: Material properties of the reinforcing steel adopted in bridge models

Property	Value
Modulus of Elasticity, E_s	29,000 ksi
Expected yield strength, f_{ye}	Discussed in detail in Model Properties
Expected tensile strength, f_{ue}	95 ksi
Expected yield strain, ε_{ye}	0.0023
Ultimate tensile strain,ε_{su}	0.120 for #10 bars and smaller 0.090 for #11 bars and larger
Reduced ultimate tensile strain, ε_{su}^{R}	0.090 for #10 bars and smaller 0.060 for #11 bars and larger
Strain at onset of strain hardening, ε_{sh}	0.0150 for #8 bars 0.0125 for #9 bars 0.0115 for #10 & 11 bars 0.0075 for #14 bars 0.0050 for #18 bars

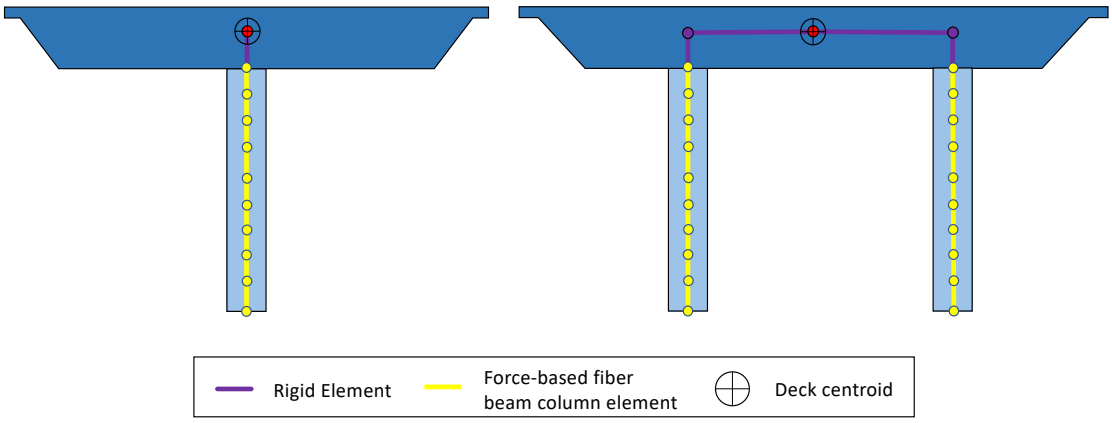

Figure 2.5: Fiber discretization of rectangular (left) and circular (right) reinforced concrete column sections

modeled using a beam-column element based on force-based formulation. As discussed by Neuenhofer and Filippou [62], force-based elements utilize exact force interpolation functions, hence their solution is only susceptible to a numerical integration error. This error is minimized for a column by increasing the number of elements, or integration points used to define that column. Consequently, given reducing the number of elements results in a more computationally efficient implementation, here, each column is represented with a single element with ten integration points. In OpenSees fiber section definitions are performed using the `fiberSec` object and `patch` commands. The cover concrete and core concrete are assigned unconfined and confined concrete properties defined in Section 2.2.1, respectively, as shown in Figure 2.5. The force-based beam-column elements are implemented in OpenSees via `forceBeamColumn` object with Gauss-Radau plastic hinge integration method [34].

The column shear deformations are considered in the analyses using an elastic material with shear stiffness of kG_cA_c, where A_c is the cross-sectional area of the column, and k denotes the shear correction factor determined based on the cross-sectional shape. The torsional column deformations are also incorporated using an elastic material. The torsional stiffness of the material is calculated using the relationship $0.2GcJc$, suggested by Aviram et al. [7], where Jc is the second moment of area of the column section, and 0.2 is the

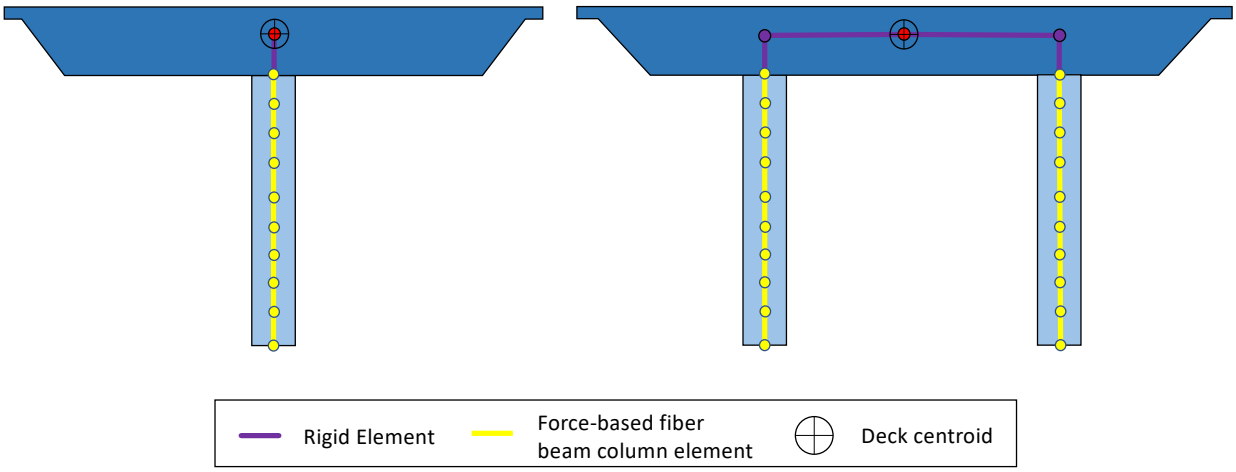

Figure 2.6: Beam-column/rigid link assemblies used in modeling single-column (left) and multi-column (right) bridge bents

stiffness reduction factor that takes into account section cracking. Lastly, to compute the combined column force-deformation behavior, the individual force-deformation responses of the defined fiber, shear, and torsional materials are aggregated. In OpenSees this aggregation is performed using the `Aggregator` construct.

The parts of columns embedded in the superstructure are modeled by defining a weightless rigid element from the top of the nonlinear beam-column element to the geometric centroid level of the superstructure. In the case of multi-column bridges, the rigid elements between the top node of columns to the centroid level of the superstructure are also connected using weightless rigid links. This horizontal connection between columns is fully restrained to the superstructure using diaphragm constraint and facilitates the transfer of force and moment between the column elements. Figure 2.6 shows typical beam-column/rigid link assemblies for single column and multi-column bridges.

Column foundations are modeled using linear translational and rotational springs—with stiffnesses K_t and K_r, respectively—aligned with the directions longitudinal and transverse to the bridge deck. Figure 2.7 shows the geometric representation of a foundation spring assembly for a bridge segment containing a single-column bridge bent. In OpenSees, foundation springs are generated using a `zeroLength` element containing all four springs in the

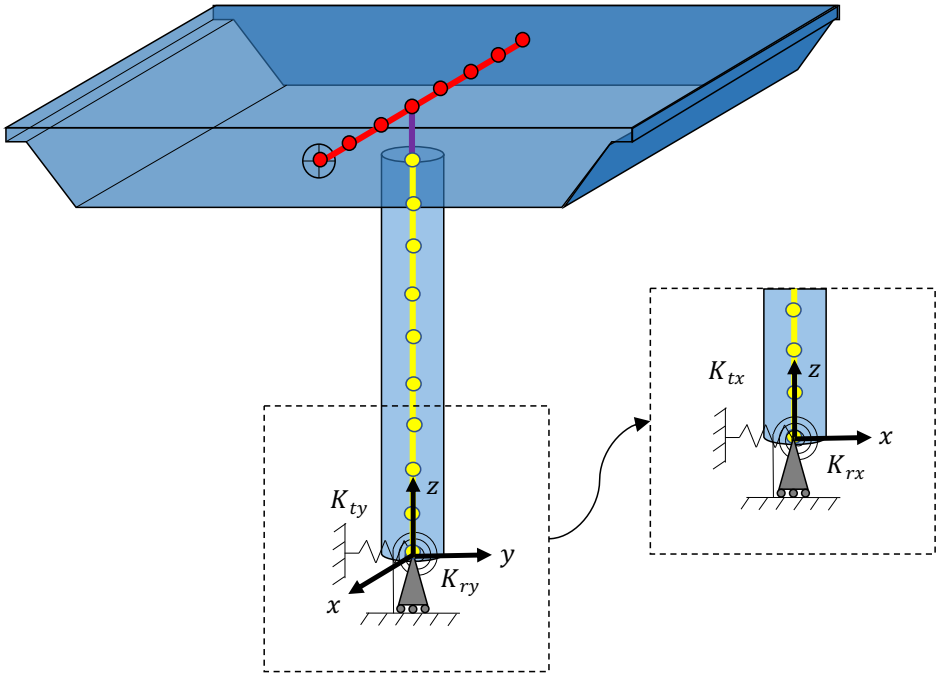

Figure 2.7: Spring idealization of soil-foundation interaction at the base of bridge columns

foundation assembly.

2.3.2 Superstructure

According to AASHTO specifications [66], superstructures of non-seismically isolated reinforced concrete bridges are designed as capacity protected members. Hence, their seismic response is essentially elastic. Consequently, for computational efficiency, reinforced concrete decks can be idealized as a linear assembly of elastic beam-columns elements running through the geometric centroid of the deck, as previously shown in Figure 2.7. In modeling regular reinforced concrete deck sections, to correctly determine the vibration periods and the seismic demands, cracked (effective) section moment of inertia I_{eff} of $0.75I_g$ is utilized [43]. For prestressed superstructure constructions, stiffness reduction is not performed, as per Caltrans SDC [65] recommendations.

2.3.3 In-Span Hinges

In long and continuous RC box-girder bridges, potential stresses due to temperature variations, creep, and shrinkage are reduced by the use of in-span hinges. In-span hinges effectively divide a structure into shorter frames by permitting relative displacements between adjacent deck segments in longitudinal and transverse directions. In an in-span hinge, the vertical forces between adjacent deck segments are transferred by supporting the long cantilever segment of the span on the short cantilever through a number of bearings. Under operational conditions, in-span hinges are expected to develop a minimal amount of stress in transverse and longitudinal directions. However, during severe earthquakes, out-of-phase vibrations may be induced in adjoining frames; consequently, large relative displacements may occur. Internal shear keys and elastomeric bearings provided in in-span hinges limit these large displacements in the transverse direction. In the longitudinal direction, relative movement is restrained by the lateral resistance of the bearings and shear keys, as well as the resistance of the hinge back wall. Figure 2.8a shows the side view of a typical in-span hinge connection. From a modeling perspective, the interactions between adjacent frame segments due to in-span hinge behavior can be simulated by coupling the end nodes of each deck segment to the respective nodes of a zero-length element (`zeroLength` in OpenSees) assembly, as shown in Figure 2.8a. Figure 2.8b provides a schematic view of the principal load-resisting components of an in-span hinge.

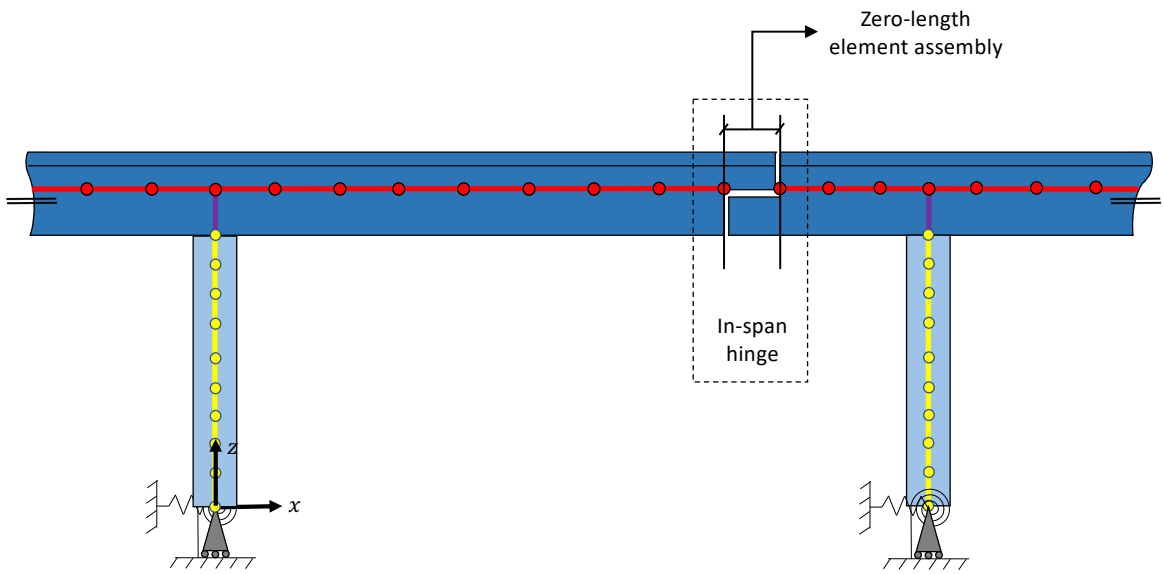

(a) Elevation view of a bridge in-span hinge

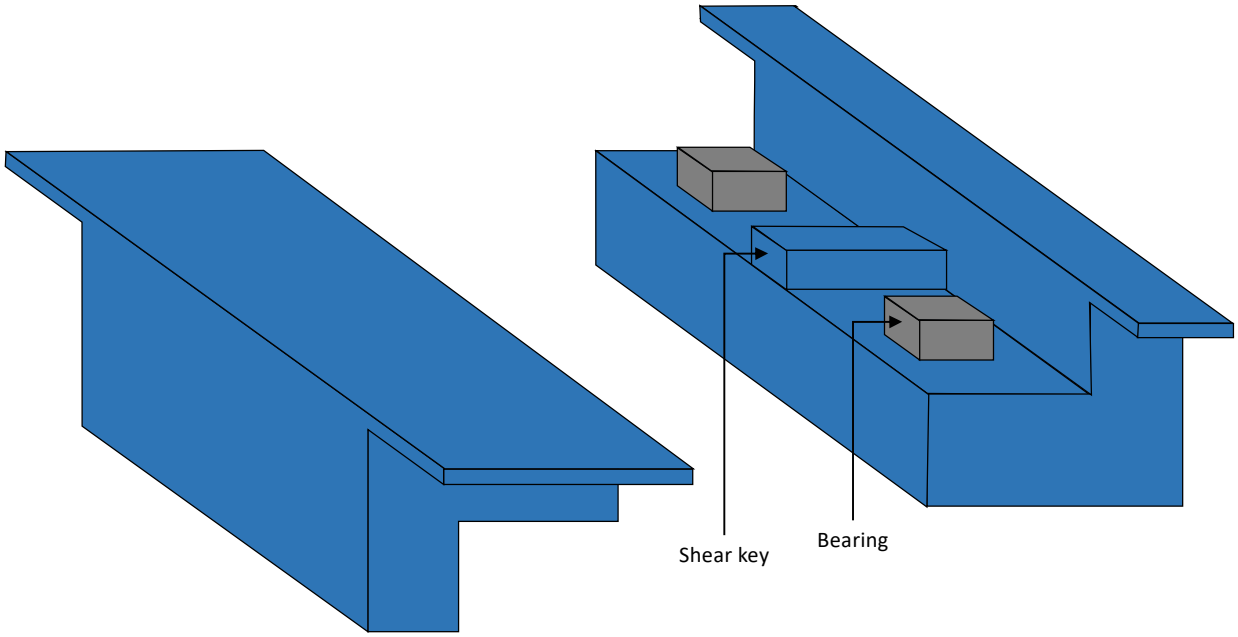

(b) Schematic view of a typical in-span hinge

Figure 2.8: (a) Elevation and (b) schematic views of a bridge in-span hinge

2.3.3.1 Longitudinal Resistance of In-Span Hinge Connections

Three components determine the longitudinal behavior of in-span hinges, namely elastomeric bearings, internal shear keys, and the hinge back wall. Lateral resistance of the bearing pads is assumed to follow the elastic-perfectly plastic behavior shown in Figure 2.9. The shear capacity of the bearings is controlled by the friction coefficient μ between the pads and the bearing seat, and the vertical force supported by each bearing N_b. For a single bearing, the yielding deformation is determined by dividing the yielding force V_{yb} for the bearing by its elastic stiffness k_b. According to Caltrans SDC [65], the maximum shear strain a bearing can sustain before failure Δ_{mb} is 1.5 in both tension and compression. In OpenSees, the force-deformation behavior of elastomeric pads is defined using the uniaxial bilinear material object `Steel01`.

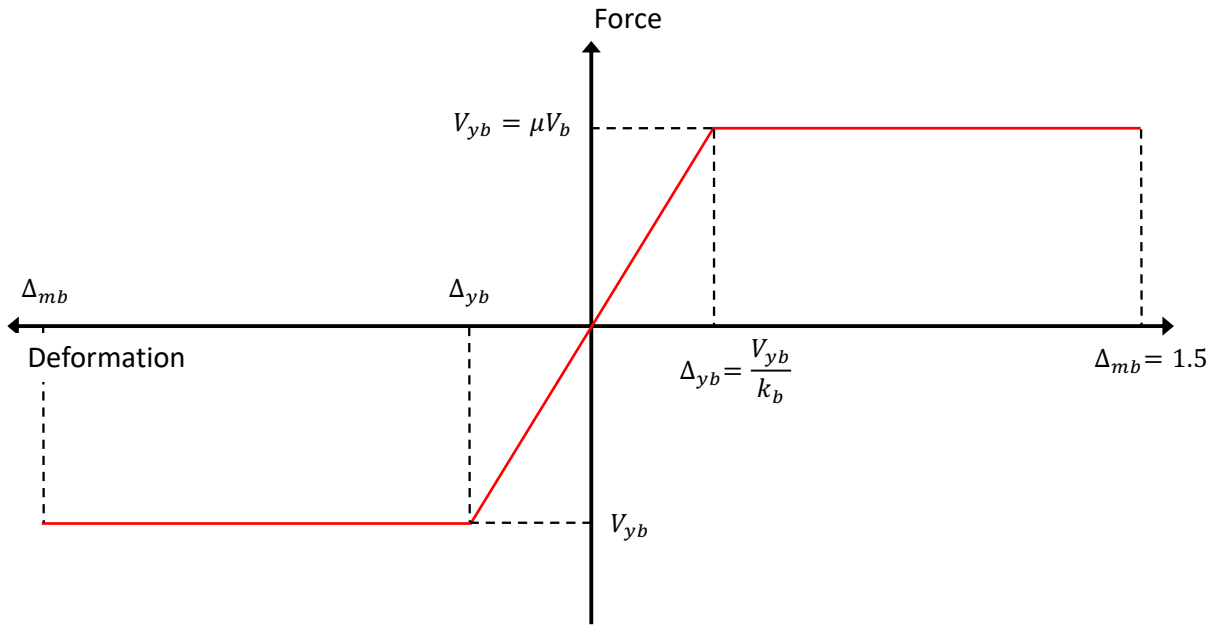

Figure 2.9: Lateral force-deformation behavior of elastomeric bearings

The behavior of shear keys is defined through a strain-softening gap material that follows the force-deformation relationship shown in 2.10, as suggested by Mangalathu [55]. The shear key capacity is determined as the product of the superstructure dead load at the in-

span hinge seat P_{dl} and the acceleration levels the shear key is designed to withstand β. The shear key lateral resistance is assumed to reach zero subsequent to plastic deformation of 3.5 inches. Note that plastic deformation is calculated as the difference between maximum permitted deformation Δ_{mk}, and the gap between the superstructure and shear key Δ_{gk}. In OpenSees, the force-deformation relationship for in-span hinge shear keys is defined using the elastic-perfectly plastic gap uniaxial material object `ElasticPPGap`.

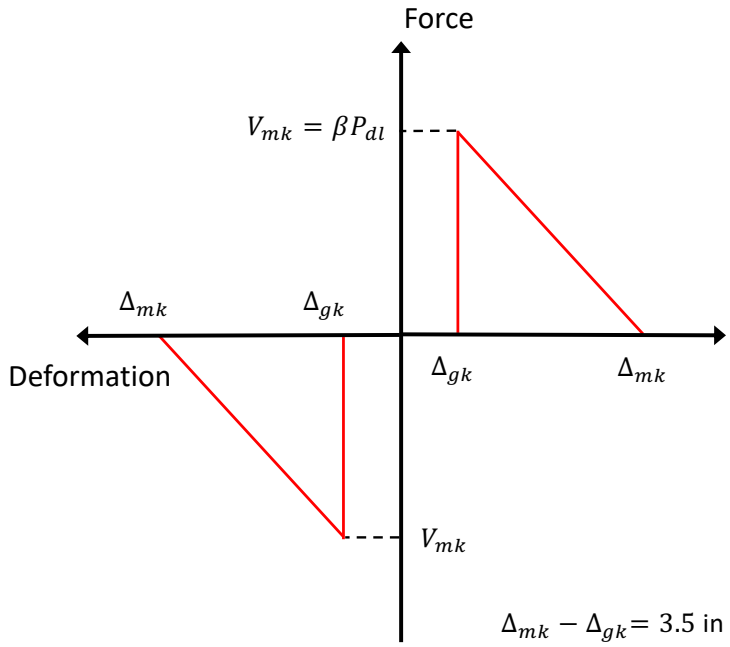

Figure 2.10: Force-deformation relationship for in-span hinge shear key elements

Longitudinal resistance of the seat back wall is modeled using the simplified impact model proposed by Muthukumar [61]. Force-deformation response of the back wall is characterized by the parameters: initial gap Δ_{gbw}, yield deformation Δ_{ybw}, maximum deformation Δ_{mbw}, initial stiffness k_{1bw}, and strain hardening stiffness k_{2bw}, as shown in 2.11. For the bridge models developed for this study, Δ_{ybw}, Δ_{mbw}, k_{1bw}, and k_{2bw} are assumed 0.1 in, 1 in, 1022.3 kip/ft, and 351.76 kip/ft, respectively. Back wall response is defined in OpenSees via the `ImpactMaterial` object.

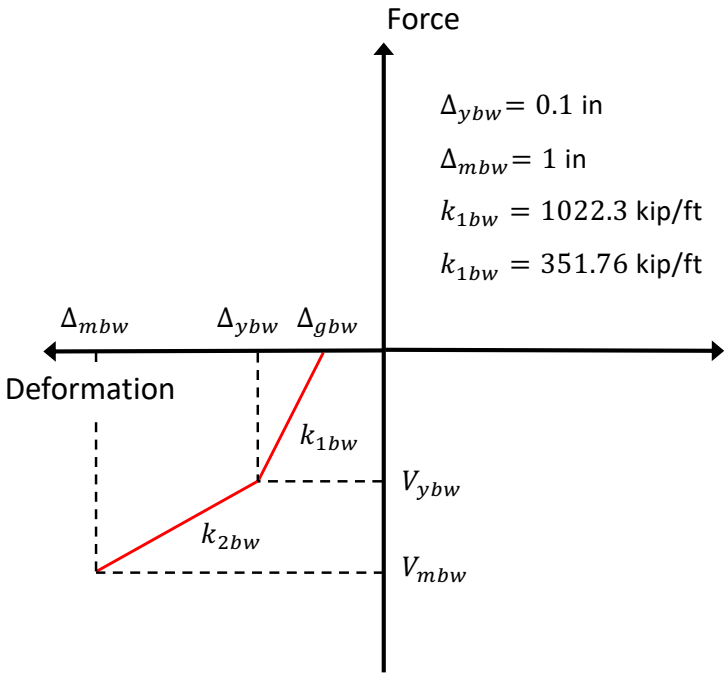

Figure 2.11: Force-deformation response of an in-span hinge back wall

2.3.3.2 Transverse Resistance of In-Span Hinge Connections

In-span hinge behavior in the transverse direction is controlled by the lateral resistance shear key and elastomeric bearing elements. The force-deformation behaviors of these elements are identical in longitudinal and transverse directions; hence they are not restated.

2.3.3.3 Vertical Resistance of In-Span Hinge Connections

The vertical resistance of an in-span hinge is defined by the seat total shear resistance, calculated by combining the contributions of reinforcing steel and concrete. Figure 2.12 shows the geometric parameters significant to the seat behavior.

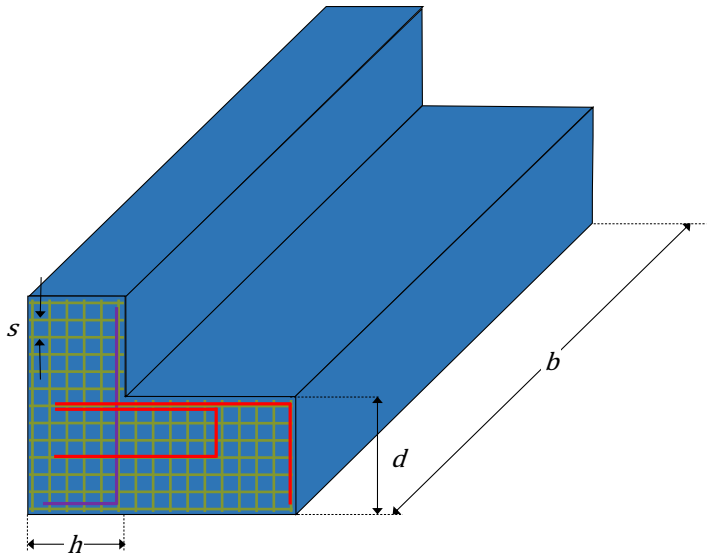

Figure 2.12: Typical in-span hinge seat reinforcement detailing

The force-deformation relationship for the reinforcing steel is determined by the reinforcement shear capacity V_{ss} and the initial deformation at which the shear capacity is reached Δ_{1s}, as shown in Figure 2.13. According to Hube and Mosalam [39],

$$V_{ss} = A_{s1} f_{ye} + A_{s2} f_{ye} \tag{2.14}$$

where A_{s1} and A_{s2} are the total steel areas for the tension tie (denoted as purple in Figure 2.12) and the first row of reinforcement crossing the back wall/seat interface (denoted as red in Figure 2.12), respectively. Megally et al. [58] recommend the use of the following expression to calculate the deformation value Δ_{1s}.

$$\Delta_{1s} = \sqrt{2}\epsilon_{ye} \left(L_d + L_a\right) \frac{h+d}{\sqrt{h^2+d^2}} \tag{2.15}$$

where, as defined in Figure 2.12, h and d denote seat height and back wall length, respectively. Experimental results indicate that the extent of the crack region is approximately equal to the seat width [58], i.e., $L_a = b$. On the other hand, the reinforcement development length L_d is given by Priestley at al. [71] as

$$L_d = \frac{d_b f_{ye}}{25\sqrt{f'_{ce}}} \tag{2.16}$$

where d_b is the nominal bar diameter in inches. In Eq. 2.16, both f_{ye} and f'_{ce} are defined in psi.

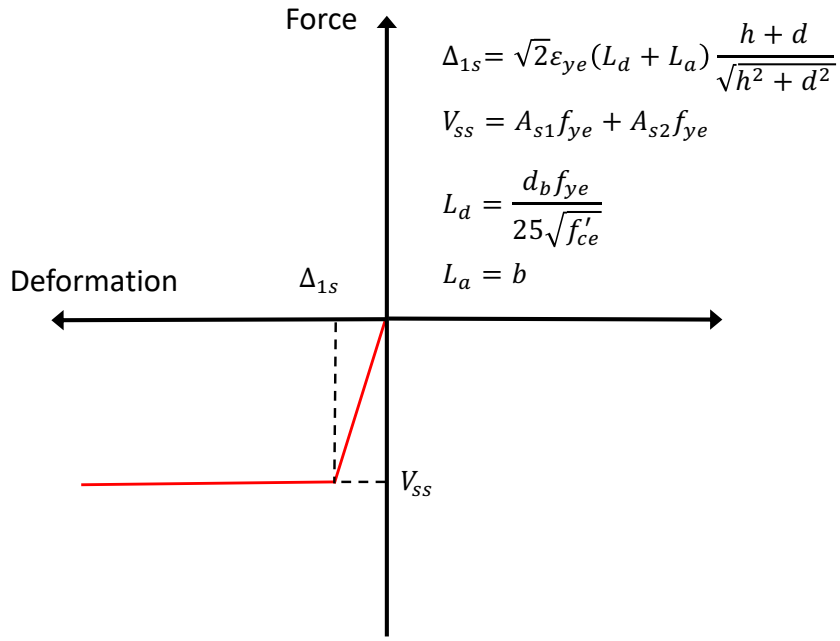

Figure 2.13: Force-deformation relationship for the contribution of steel reinforcement to the vertical resistance of an in-span hinge seat

The force-deformation relationship for the concrete is defined in terms of three parameters: concrete shear strength V_{cs}, the corresponding concrete deformation Δ_{2s}, and the deformation at which the shear capacity of concrete is reduced to zero Δ_{3s}, as shown in Figure 2.14. Concrete shear contribution V_{cs} is calculated as [1]

$$V_{cs} = 2.4\sqrt{f'_{ce}}bd \tag{2.17}$$

where f'_{ce} is defined in psi, and b and d denote the seat width and back wall length, respectively (see Figure 2.12). As reported by Megally et al. [58], Δ_{2s} is given by

$$\Delta_{2s} = \sqrt{2}\epsilon_{ye}\left(L_d + L_a\right)\frac{h+d}{s} \tag{2.18}$$

Lastly, according to Silva et al. [85], Δ_{3s} is determined through the relationship

$$\Delta_{3s} = \sqrt{2}\epsilon_3\left(L_d + L_a\right)\frac{h+d}{s} \tag{2.19}$$

In Eq. 2.18 and 2.19, s is the spacing for the reinforcement within the seat, $\epsilon_3 = 0.005$. The remaining parameters are as defined before.

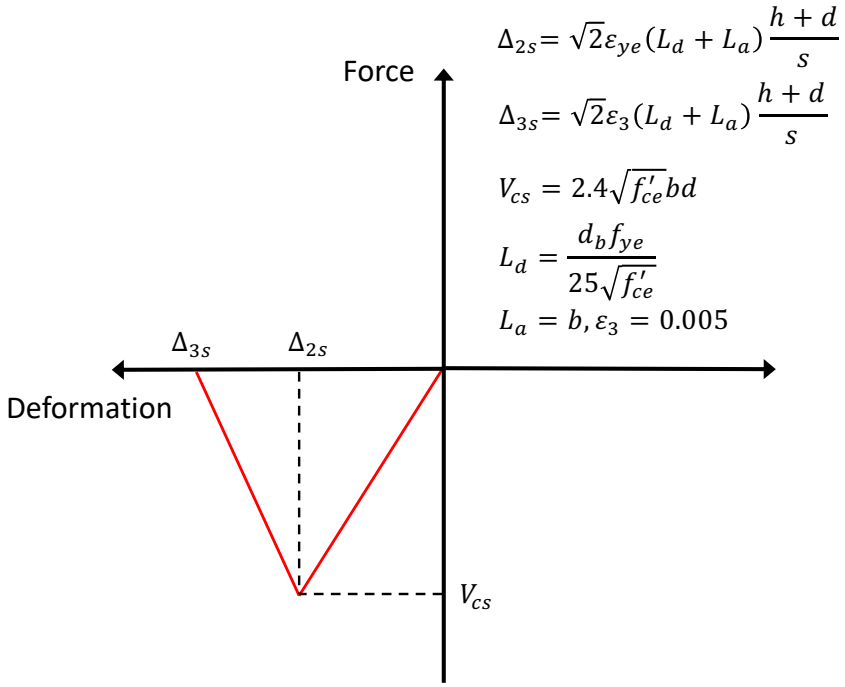

Figure 2.14: Force-deformation relationship for the contribution of concrete to the vertical resistance of an in-span hinge

By combining the contributions of the steel reinforcement and concrete in parallel, the force-deformation curve shown in Figure 2.15 is obtained for the vertical resistance of the in-span hinge seat. In OpenSees, the contribution to the vertical seat resistance by the reinforcing steel, shown in Figure 2.13, is defined using the uniaxial `Bilin` material object. The concrete contribution displayed in Figure 2.14 is defined using the uniaxial zero tensile strength concrete material object `Concrete01`. The force-deformation relationships for the steel reinforcement and concrete are combined in parallel using the `Parallel` uniaxial material object in OpenSees.

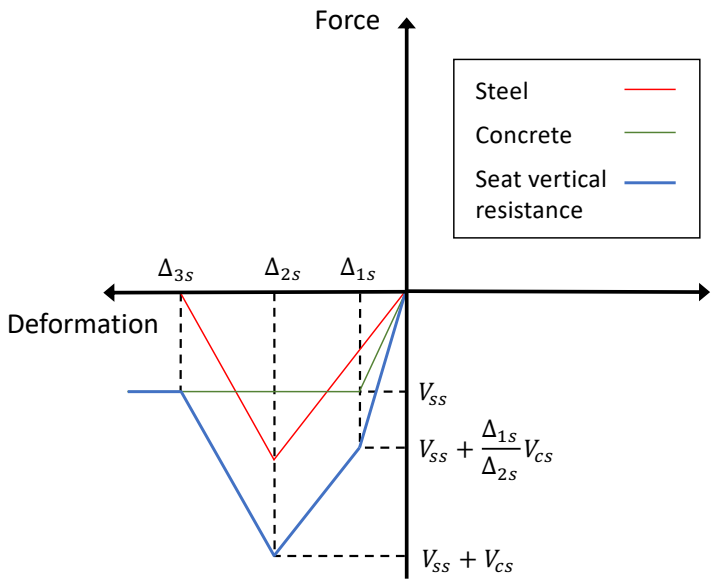

Figure 2.15: Force-deformation relationship for the vertical resistance of an in-span hinge

2.3.3.4 Zero-Length Element Assembly for Simulating In-Span Hinge Behavior

Figure 2.16 shows the final zero-length element assembly used to define nonlinear in-span hinge behavior. Note that weightless rigid elements (denoted as purple in Figure 2.16) are attached to the end nodes of each deck segment to consider the rotational response appropriately. Force-deformation characteristics of the in-span hinge back wall and seat are calculated as in Figures 2.11 and 2.15, and the determined resistances are equally divided among the respective spring elements. In order to define the elastomeric bearing and shear key resistances in the transverse direction, the total contribution of each component is calculated via scaling the relationships in 2.9 and 2.10 by the number of components, then the obtained resistances evenly distributed among the respective springs.

2.3.4 Abutments

At each end of a bridge, the superstructure is supported by abutments. The primary purpose of abutments is to transfer the vertical and horizontal loads from the superstructure to the

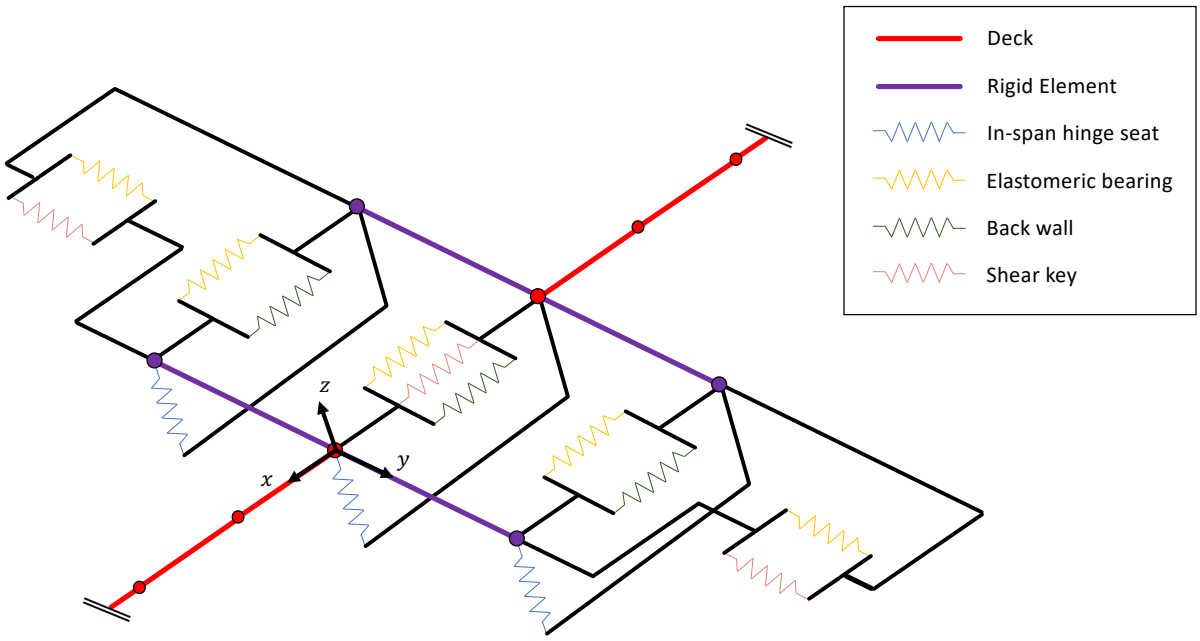

Figure 2.16: Zero-length element assembly for an in-span hinge connection

abutment foundations and retain the lateral loads from roadway embankment under both operational and extreme loading conditions. In terms of the rigidity of the connection to the superstructure, abutments are classified as integral and non-integral. Diaphragm and seat-type abutments are the most common examples of integral and non-integral abutments, respectively. Figure 2.17 shows the side views of these two abutment types. Figure 2.18 shows the components of a typical seat-type abutment.

The diaphragm abutment is built monolithic to the bridge superstructure. The abutment is connected straight to abutment foundations, and its diaphragm is in direct contact with the embankment. As a result of this simpler construction, diaphragm abutment induces lower initial construction costs. Its application, however, is limited to short-length bridges, since it is less amenable to large superstructure movements due to temperature variations, creep and shrinkage, and post-tensioning compared to non-integral abutment types.

The seat-type abutment is not integral to the superstructure and acts as an independent structural component of the bridge. In a seat abutment, the superstructure is supported by the bearings on the abutment seat. The lateral soil pressure is mostly resisted by the stem

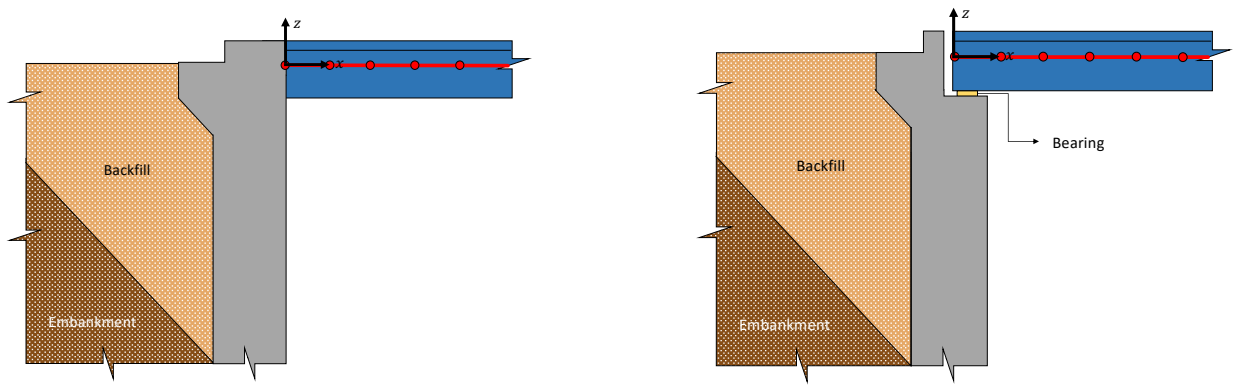

(a) Diaphragm abutment (b) Seat-type abutment

Figure 2.17: A side view of diaphragm (a) and seat-type (b) abutments. Note that, for clarity, abutment shear key is omitted in (b)

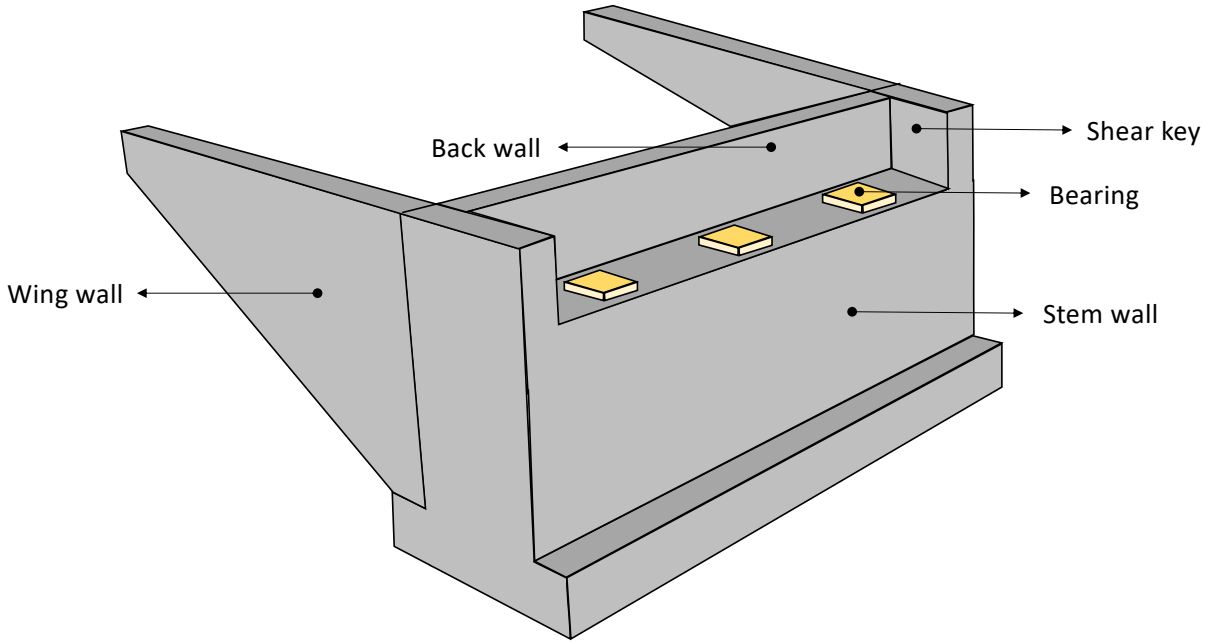

Figure 2.18: Components of a seat-type abutment

wall, with just the portion of the backfill above the seat level retained by the back wall. Superstructure movements in longitudinal and transverse directions are restrained by the back wall and the shear keys, respectively. Unlike in diaphragm abutments, the gap between the superstructure and back wall/shear keys provides added stress relief for temperature, creep and shrinkage, or post-tensioning induced deformations. That renders seat-type abutments more suitable to long, highly skewed, or curved bridges than diaphragm abutments. Unseating of the superstructure is a critical mode of failure for seat-type abutments, resulting in the collapse of the end span. Thus, to eliminate unseating, modern-day seat-type abutments are designed with large seat widths.

2.3.4.1 Abutment Behavior in Longitudinal Direction

The longitudinal behavior of a diaphragm abutment is characterized by the lateral resistance of abutment piles and the passive resistance of the abutment backfill. Following the approach presented by Mangalathu [55], lateral resistance of abutment piles is modeled using the trilinear force-deformation relationship displayed in Figure 2.19. The initial yield deformation Δ_{1p} and plastic yield deformation Δ_{2p} are set to 6 mm and 25 mm, respectively. The yield force V_{1p} is set equal to half the plastic yielding force V_{2p}. In OpenSees, the force-deformation behavior of abutment piles is captured using the uniaxial bilinear hysteretic material object `Hysteretic` with pinching factors during reloading for strain and stress set to 0.75 and 0.5, respectively, according to Ramanathan et al. [77].

Passive longitudinal resistance of abutment backfill is defined using the Generalized Hyperbolic Force–Displacement (GHFD) backbone curve proposed by Khalili-Tehrani et al. [44]. Figure 2.20 shows the force-deformation response of homogeneous backfill material as defined by GHFD. The change in lateral resistance of the backfill material $V_{bw}(\Delta)$ is defined in terms of lateral displacement Δ as

$$V_{bw} = f_{\delta} \frac{a_r \Delta}{\widehat{H} + b_r \Delta} \widehat{H}^{n_{bw}} \tag{2.20}$$

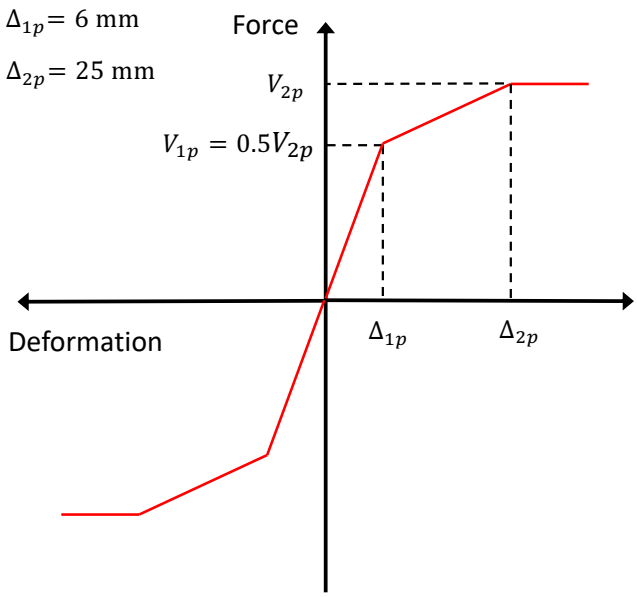

Figure 2.19: Force-deformation relationship for abutment piles

for

$$\widehat{H} = \frac{H_{bw}}{H_r} \tag{2.21}$$

$$a_r = \frac{1}{\beta_{bw}} (\eta - 1)\, \alpha \tag{2.22}$$

$$b_r = \frac{1}{\beta_{bw}} (\eta - 2) \tag{2.23}$$

where H_{bw} is the back wall height, H_r is the reference back wall height of 3.2808 ft, the wall friction adjustment factor $f_\delta = 1$, and

$$\beta_{bw} = \left[670.47 - 269.05\,(\tan\phi)^{1.23}\right] \varepsilon_{50} \tag{2.24}$$

$$\alpha = \left[60.49\,(\tan\phi)^2 + 5.74\right] \gamma + \left[34.71\,(\tan\phi)^{1.79} + 9.37\right] c \tag{2.25}$$

$$n_{bw} = \frac{0.13\,(\tan\phi)^{1.2} + 0.22}{\sqrt{c}} + 0.9 \tag{2.26}$$

$$\eta = 18.10 - 9.38\sqrt{tan\phi} \tag{2.27}$$

Recognizing that silty sand is the most common abutment backfill material [40], in the generated bridge models, unit weight γ, internal friction angle ϕ, cohesion c, and strain

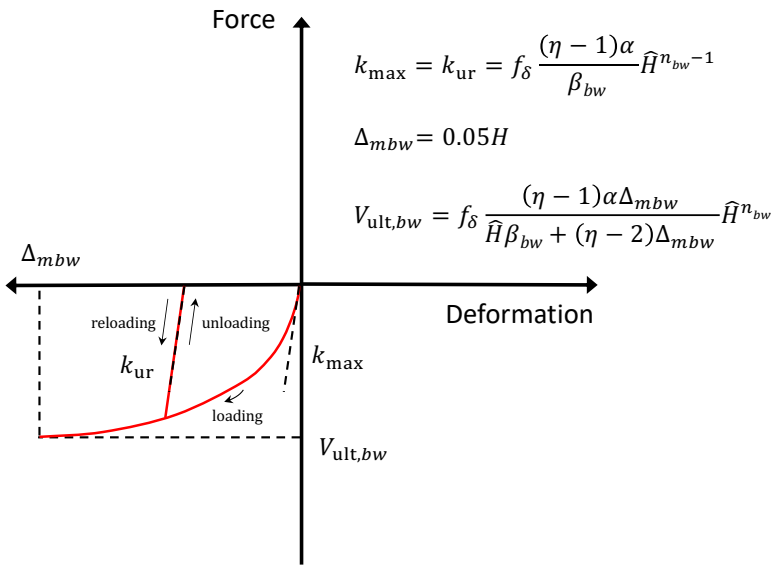

Figure 2.20: Force-deformation relationship for abutment backfill

at 50% ultimate strength ε_{50} are respectively set to 0.125 kcf, 40°, 0.3 ksf, and 0.5% after Stewart et al. [88].

In OpenSees, the backfill material is defined using the `HyperbolicGapMaterial` object with zero gap. The initial stiffness $k_{\max}$ and unloading/reloading stiffness k_{ur} of the hyperbolic material is determined using the relationship

$$k_{\max} = k_{\text{ur}} = f_\delta a_r \widehat{H}^{n_{bw}-1} \tag{2.28}$$

The ultimate strength $V_{\text{ult}_{bw}}$ of the material is calculated by setting Δ equal to the maximum deformation Δ_{mbw}. According to Shamsabadi et al. [83] Δ_{mbw} for silty sand backfill materials is determined as

$$\Delta_{mbw} = 0.05H \tag{2.29}$$

In seat-type abutments, lateral resistances of the abutment back wall and elastomeric bearings are also critical in resembling the longitudinal abutment behavior. Contributions of back wall and bearings are defined according to the force-displacement relationships described in Section 2.3.3.1.

2.3.4.2 Abutment Behavior in Transverse Direction

The transverse behavior of a diaphragm abutment is determined by the lateral resistance of abutment piles alone. Lateral abutment pile response is assumed identical in both longitudinal and transverse directions, hence it is modeled according to the force-deformation curve defined in Section 2.3.4.1.

In a seat-type abutment, however, elastomeric bearings and shear keys also contribute to the abutment resistance in the transverse direction. Bearings follow the elastic-perfectly plastic force-deformation behavior illustrated in Section 2.3.3.1. The transverse resistance of each shear key is defined as the combined shear resistance from the shear key reinforcing steel and concrete. The geometric parameters critical to shear key behavior are displayed in Figure 2.21.

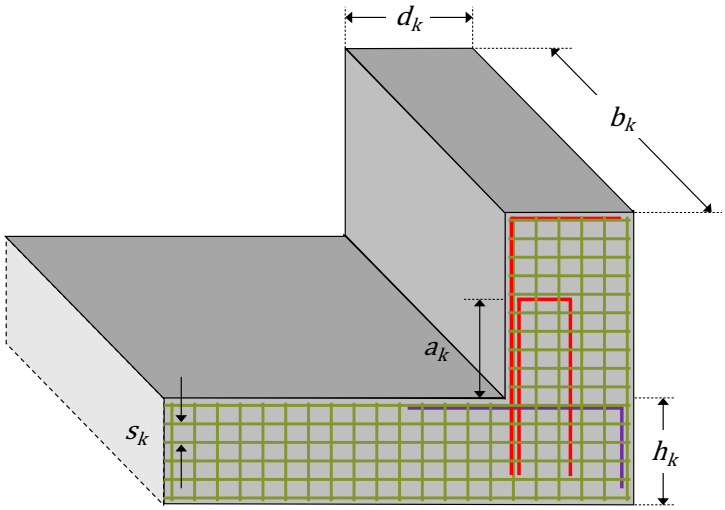

Figure 2.21: Typical abutment shear key reinforcement detailing

According to Silva et al. [85], the force-deformation relationship for the reinforcing steel is defined in terms of reinforcement shear capacity V_{sk}, initial deformation at which the shear capacity is reached Δ_{1k}, deformation corresponding to initial softening Δ_{4k}, and ultimate shear deformation Δ_{5k} as shown in Figure 2.22. The reinforcement shear capacity

is calculated as

$$V_{sk} = \frac{f_{ye}}{h_k + a_k} \left[(A_{k1} + A_{k2})\, h_k + \frac{A_{ks}}{2s_k} \left(n_v h_k^2 + n_h d_k^2 \right) \right] \tag{2.30}$$

where A_{k1}, A_{k2}, A_{ks} are the total steel areas for the tension tie (denoted as purple in Figure 2.21), the first row of reinforcement crossing the abutment seat/shear key interface (denoted as red in Figure 2.21), and the side reinforcement (denoted as green in Figure 2.21), respectively. n_h and n_v signify the numbers of side faces with horizontal and vertical side reinforcement, respectively. h_k, a_k, and s_k are as defined in Figure 2.21.

The following equations are utilized to calculate Δ_{1k}, Δ_{4k}, and Δ_{5k}.

$$\Delta_{1k} = \sqrt{2}\epsilon_{ye} \left(L_d + L_a \right) \frac{h_k + d_k}{\sqrt{h_k^2 + d_k^2}} \tag{2.31}$$

$$\Delta_{4k} = \sqrt{2}\epsilon_4 \left(L_d + L_a \right) \frac{h_k + d_k}{s_k} \tag{2.32}$$

$$\Delta_{5k} = \sqrt{2}\epsilon_5 \left(L_d + L_a \right) \frac{h_k + d_k}{s_k} \tag{2.33}$$

where, $L_a = b$, L_d is as defined in Eq. 2.16, $\epsilon_4 = 0.007$, and $\epsilon_5 = 0.01$.

The contribution of concrete to abutment shear key capacity is determined as defined in 2.3.3.3. The force-deformation relationship for the concrete contribution is as shown in Figure 2.14. Peak concrete contribution V_{ck}, Δ_{2k}, and Δ_{3k} are calculated using Eq. 2.17, 2.18, and 2.19, respectively.

Combining the contributions of the steel reinforcement and concrete in parallel, and connecting this material in series to an elastic no-tension material to account for the gap between the deck and shear keys, the force-deformation curve shown in Figure 2.23 is obtained for the lateral resistance of an abutment shear key. In OpenSees, the contribution of reinforcing steel, shown in Figure 2.22, is prescribed using the uniaxial `Bilin` material object. The force-deformation curve for concrete displayed in Figure 2.14 is implemented using the uniaxial zero tensile strength concrete material object `Concrete01`. Compression-only gap element was defined using the elastic-perfectly plastic gap uniaxial material object `ElasticPPGap` where tangent stiffness is set to a very high value. The force-deformation relationships for the steel reinforcement and concrete are combined in parallel using the `Parallel` uniaxial

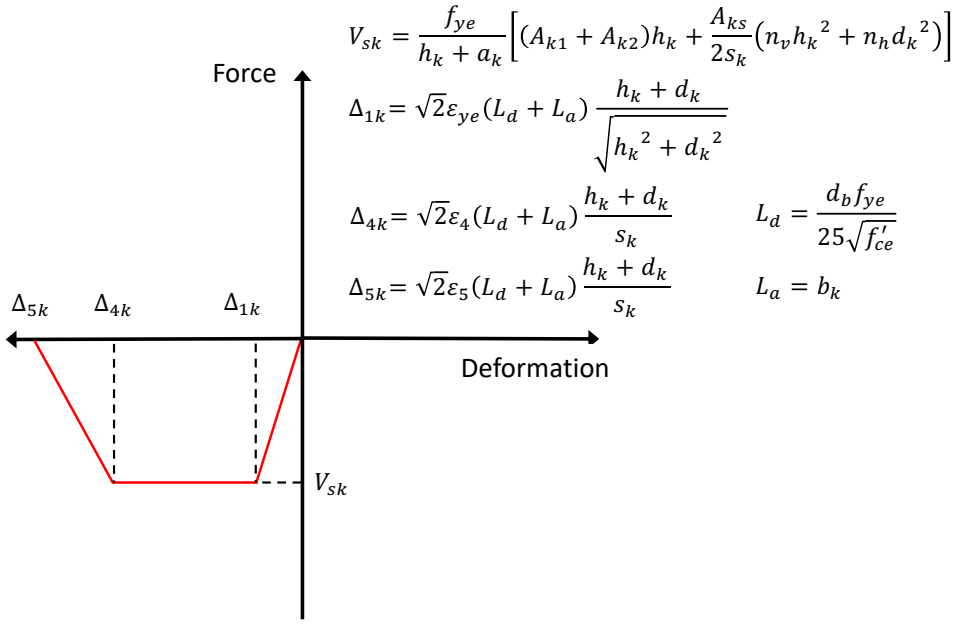

Figure 2.22: Force-deformation relationship for the contribution of steel reinforcement to the lateral resistance of an abutment shear key

material object. Combined concrete and steel material is connected in series with the gap element using the `Series` uniaxial material object in OpenSees.

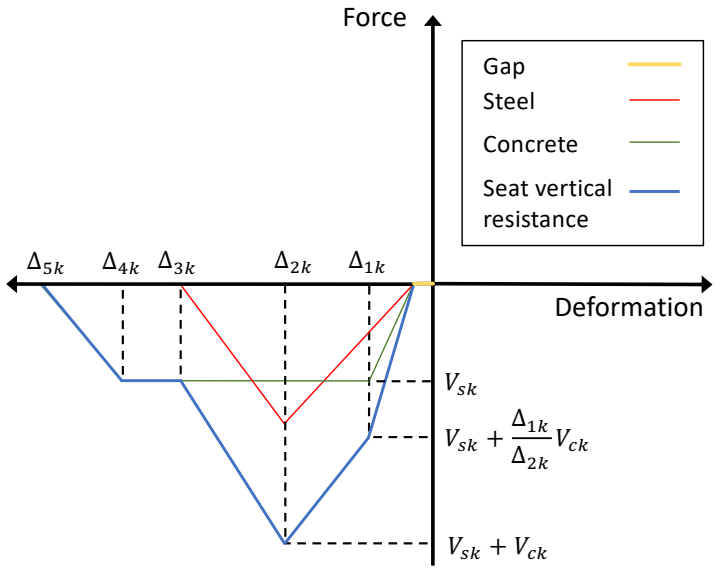

Figure 2.23: Force-deformation relationship for an abutment shear key

2.3.4.3 Zero-Length Element Assembly for Simulating Abutment Behavior

Figure 2.24 shows the final zero-length element assembly used to define nonlinear abutment behavior for diaphragm and seat-type abutments. Force-deformation characteristics of the abutment piles are calculated as in Figures 2.19 and multiplied by the deck width to determine the longitudinal and transverse resistances of pile spring elements. Longitudinal resistance of the backfill springs is calculated by multiplying the force-deformation relationship in Figure 2.20 by the width of the backwall. As in the case of in-span hinges, to define the elastomeric bearing and shear key spring resistances in the transverse direction, the total contribution of each component is calculated via scaling the relationships in Figures 2.9 and 2.23 by the number of components, then the calculated resistances are split among the respective springs.

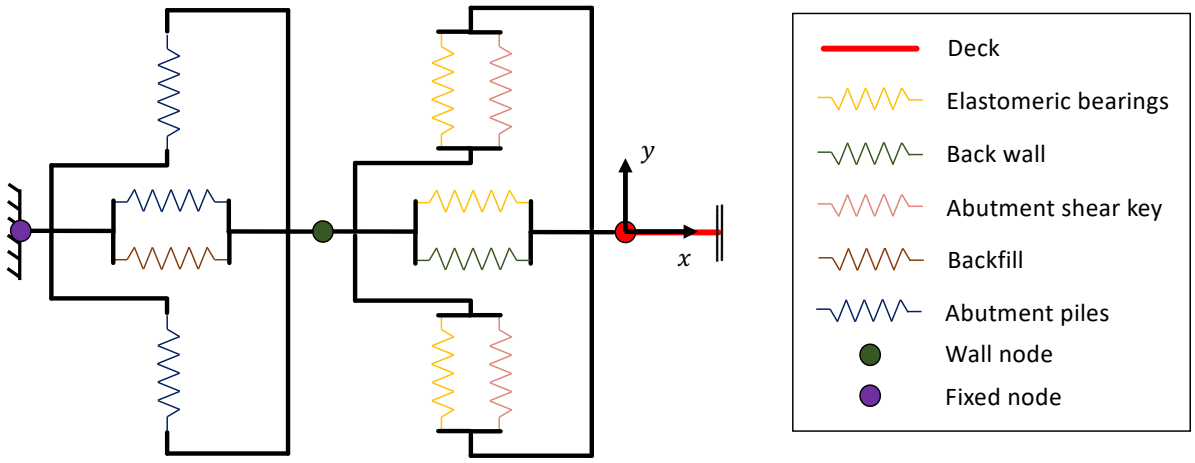

Figure 2.24: Zero-length element assembly for diaphragm (a) and seat-type abutments (b)

The translational and torsional masses for column elements were calculated as

$$M_{xc} = M_{yc} = M_{zc} = \rho_c A_c L_{\text{trib}} \tag{2.34}$$

$$M_{zz} = \frac{1}{8}\rho_c A_c L_{\text{trib}} D_c \tag{2.35}$$

where L_{trib} and D_c are as defined in Figure 2.25, and ρ_c and A_c are concrete density and column cross-sectional area, respectively.

The translational and torsional masses for deck segments were computed following the relationships

$$M_{xd} = M_{yd} = M_{zd} = \rho_c A_w L_{\text{trib}} \tag{2.36}$$

$$M_{cc} = \frac{1}{12}\rho_c A_w L_{\text{trib}} d_w \tag{2.37}$$

where L_{trib} and d_w are as defined in Figure 2.25, and A_w is the deck cross-sectional area, respectively.

To simulate structural damping, constant viscous damping ratios were sampled from a normal distribution with a mean of 4.5% and a standard deviation of 1.25% after Padgett citepadgett2007. Lower and upper bound damping ratios were set to 2% and 7%, respectively.

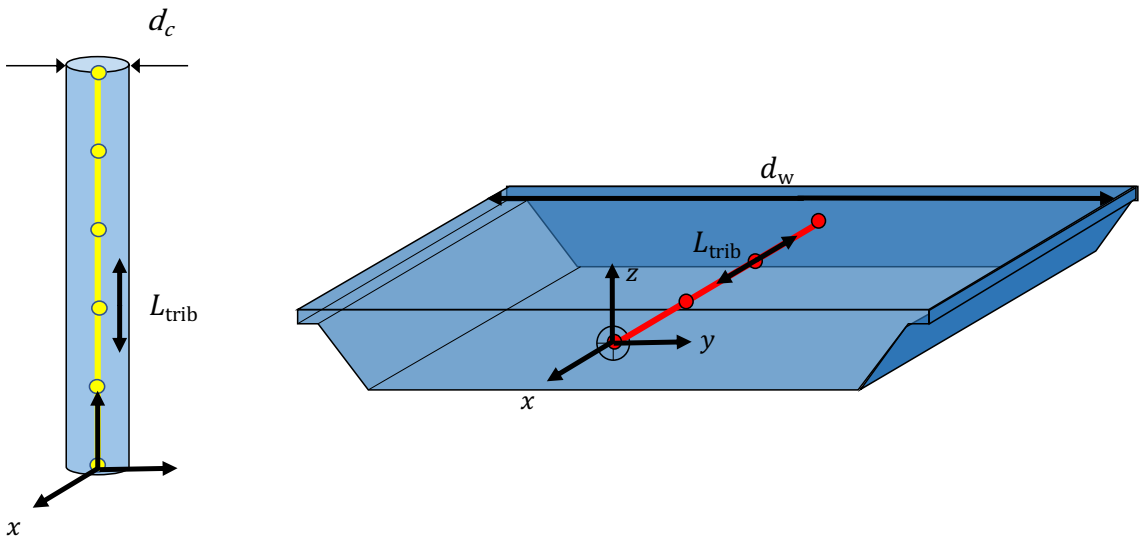

Figure 2.25: Zero-length element assembly for diaphragm (a) and seat-type abutments (b)

2.4 Model Properties

Model properties were assigned according to the class statistics suggested by Mangalathu [55]. Column properties were defined as in Table 2.2. Colum foundation properties were defined according to Table 2.3. Properties of elastomeric bearing were prescribed following Table 2.4. Abutment pile capacities were defined using 2.5. The gap between deck and shear

key elements was assumed to follow a uniform distribution with a mean of 0.75 in and a standard deviation of 0.19 in (Lower bound: 0, Upper bound: 1.590).

Table 2.2: Statistical distributions for column material and reinforcement paramaters

			Statistical Distribution				
Design Era	Parameter	Units	Type	Mean	SD	Lower Bound	Upper Bound
All	Longitudinal steel reinforcement ratio	N/A	U	2.00	0.33	1.0	3.0
	Concrete compressive strength	ksi	N	3.90	0.48	2.94	5.19
Pre-1971	Steel yield strength	ksi	N	57.3	4.5	49.0	67.0
	Transverse steel reinforcement ratio	N/A	4 at 12 in. irrespective of the cross-section				
	Concrete compressive strength	ksi	N	4.55	0.56	3.43	5.67
Post-1971	Steel yield strength	ksi	N	69.0	5.5	58.0	80.0
	Transverse steel reinforcement ratio	N/A	U	0.85	0.07	0.4	1.3

Table 2.3: Statistical distributions for column foundation spring parameters

			Transverse Direction					Transverse/Longitudinal Direction				
Design Era	Bent Type	Foundation Fixity	Type	Mean	SD	Lower Bound	Upper Bound	Type	Mean	SD	Lower Bound	Upper Bound
Translational stiffness (kip/in)												
	Single	Fixed	LN	1250.0	2.5	500.0	3125.0	LN	1.0	1.0	1.0	1.0
Pre-1971	Multiple	Pinned	LN	625.0	2.5	250.0	1562.5	LN	1.0	1.0	1.0	1.0
	Multiple	Fixed	LN	625.0	2.5	250.0	1562.5	LN	1.0	1.0	1.0	1.0
	Single	Fixed	LN	2000.0	2.5	800.0	5000.0	LN	1.0	1.0	1.0	1.0
1971-1990	Multiple	Pinned	LN	1000.0	2.5	400.0	2500.0	LN	1.0	1.0	1.0	1.0
	Multiple	Fixed	LN	1000.0	2.5	400.0	2500.0	LN	1.0	1.0	1.0	1.0
	Single	Fixed	LN	2500.0	2.5	1000.0	6250.0	LN	1.0	1.0	1.0	1.0
Post-1990	Multiple	Pinned	LN	1000.0	2.5	400.0	2500.0	LN	1.0	1.0	1.0	1.0
	Multiple	Fixed	LN	1000.0	2.5	400.0	2500.0	LN	1.0	1.0	1.0	1.0
Rotational stiffness ($\times 10^6$kip-in/rad)												
	Single	Fixed	LN	25.0	2.5	10	62.5	LN	1.5	1.5	1.0	2.25
Pre-1971	Multiple	Pinned	LN	2.5	2.5	1.0	6.3	LN	1.0	1.5	0.67	1.50
	Multiple	Fixed	LN	4.0	2.5	1.6	10.0	LN	1.0	1.5	0.67	1.50
	Single	Fixed	LN	80.0	2.5	32.0	200.0	LN	1.5	1.5	1.0	2.25
1971-1990	Multiple	Pinned	LN	12.0	2.5	4.8	30.0	LN	1.0	1.5	0.67	1.50
	Multiple	Fixed	LN	18.0	2.5	7.2	15.0	LN	1.0	1.5	0.67	1.50
	Single	Fixed	LN	190.0	2.5	76.0	475.0	LN	1.15	1.15	1.00	1.32
Post-1990	Multiple	Pinned	LN	20.0	2.5	8.0	50.0	LN	1.20	1.25	0.96	1.50
	Multiple	Fixed	LN	30.0	2.5	12.0	75.0	LN	1.20	1.25	0.96	1.50

Table 2.4: Statistical distributions for elastomeric bearing parameters

			Statistical Distribution				
Design Era	Parameter	Units	Type	Mean	SD	Lower Bound	Upper Bound
Pre-1971	Stiffness/deck width	kip/in/ft	LN	0.40	0.35	0.70	3.0
	Coefficient of friction	N/A	N	0.30	0.10	0.10	0.50
1971-1990	Stiffness/deck width	kip/in/ft	LN	0.77	0.52	0.7	6.0
	Coefficient of friction	N/A	N	0.30	0.10	0.10	0.50
Post–1990	Stiffness/deck width	kip/in/ft	LN	0.00	0.45	0.4	2.5
	Coefficient of friction	N/A	N	0.30	0.10	0.10	0.50

Table 2.5: Statistical distributions for lateral abutment pile capacity per deck width for all construction eras

		Statistical Distribution				
Abutment type	Units	Type	Mean	SD	Lower Bound	Upper Bound
Diaphragm	kip/ft	LN	1.79	0.35	2.5	12.0
Seat	kip/ft	LN	2.08	0.35	4.0	16.0

2.5 Bridge-Specific Fragility Functions

Component demand thresholds required to compute the fragility function for each damage class is defined according to Ramanathan et al. [77]. Dispersion value for all components and CDT levels are assumed 0.35. For abutment seat classification method please refer to the referenced paper.

Table 2.6: Component demand threshold (CDT) values used in computing fragility functions

Component	EDP	Units	$M_{\text{CDT-0}}$	$M_{\text{CDT-1}}$	$M_{\text{CDT-2}}$	$M_{\text{CDT-3}}$
Columns						
Pre-1971	Curvature ductility	N/A	0.8	0.9	1.0	1.2
1971-1990	Curvature ductility	N/A	1.0	2.0	3.5	5.0
Post-1990	Curvature ductility	N/A	1.0	4.0	8.0	12.0
Abutment Seat						
AS1-S	Displacement	Inches	0.5	1.0	2.0	3.0
AS2-S	Displacement	Inches	1.0	3.0	6.0	9.0
AS3-S	Displacement	Inches	1.0	3.0	10.0	15.0
AS3-L	Displacement	Inches	2.0	6.0	10.0	15.0
AS4-S	Displacement	Inches	1.0	3.0	14.0	21.0
AS4-L	Displacement	Inches	2.0	6.0	14.0	21.0
Abutment Deformation						
Passive	Displacement	Inches	3.00	10.00	N/A	N/A
Active	Displacement	Inches	1.50	4.00	N/A	N/A
Transverse	Displacement	Inches	1.00	4.00	N/A	N/A
Joint Seal						
Type A	Displacement	Inches	0.5	N/A	N/A	N/A
Type B	Displacement	Inches	1.0	N/A	N/A	N/A
Strip	Displacement	Inches	2.0	5.0	N/A	N/A
Modular	Displacement	Inches	4.0	10.0	N/A	N/A
Bearings	Displacement	Inches	1.0	4.0	N/A	N/A
Restrainers	Displacement	Inches	1.5	4.0	N/A	N/A
Shear keys	Displacement	Inches	1.5	5.0	N/A	N/A
Deck	Displacement	Inches	4.0	12.0	N/A	N/A
Bent Foundation						
Translation	Displacement	Inches	1.00	4.00	N/A	N/A
Rotation	Rotation	Radian	1.50	6.00	N/A	N/A

CHAPTER 3

Framework for Image-Based Modeling of Bridge Structures

3.1 Overview

At the highest level, the image-based modeling framework consists of five steps:

1. Automated identification of bridge location
2. Semi-automated development of bridge wireframe model
3. Semi-automated determination of deck properties
4. Automated extraction of column geometries
5. Semi-automated determination of in-span hinge properties

These key steps are described in further detail in the following sections, followed by a case study comparing the performance of a model generated through the framework against a structural model of the same bridge established using as-built drawings.

3.2 Identification of Bridge Location and Centerline Curve

The framework is capable of automatically identifying bridge locations based on the approximate coordinate information available in the National Bridge Inventory (NBI) [28]. The program first sends a query through OpenStreetMap's Overpass API [67] and searches for all the bridges fully or partially covered within a circle of a mile-radius centered at the NBI

coordinates of the considered bridge. It then reads the route information of all the bridges selected through the query and keeps the one(s) that match this information. Then, the program randomly samples two points along the centerline curves of each of the selected bridges and cross-checks both the route and direction information of the selected bridges. At this step, the results are narrowed down to a single match, and the centerline information necessary for wireframe model construction is established. Figure 3.1 summarizes the described bridge location and centerline identification procedure.

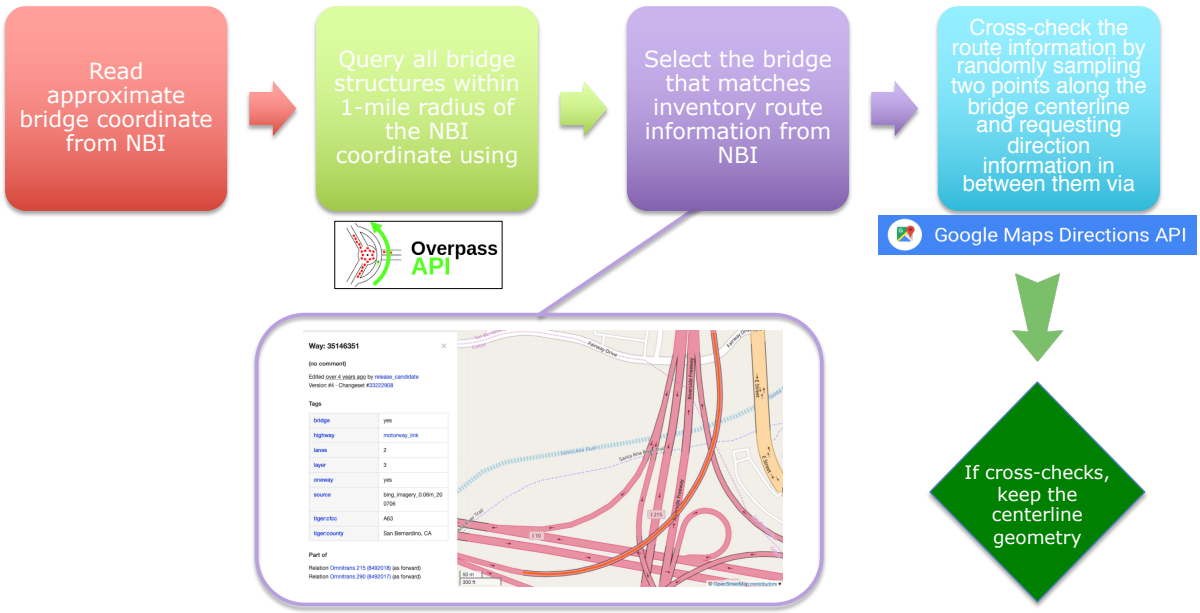

Figure 3.1: Bridge location and centerline identification

3.3 Developing the Bridge Wireframe Model

Developing the bridge wireframe model requires identification of ground surface level, pier locations, and the distance from the ground surface to the top of the deck. The framework captures ground elevations by automatically creating a minimum of 1000 sampling points along the bridge centerline curve, then querying ground elevations at those points via Google Maps Elevation API. Determining pier locations and the normal between the ground surface and deck top surface is somewhat more involved. First, two lines (curves rather) of virtual

cameras are created offset from the bridge centerline by a distance proportional to the length of the bridge, and all Google Street View images along this line are harvested. Then images are semantically segmented so that all areas belonging to column and deck elements are clearly marked. Next, based on their order of occurrence along the centerline, each column element is assigned a number. Then images including each column element are placed in separate batches, and by performing auto-calibration, camera parameters for the images are determined. Next, column bottom edges and deck's top edges are detected and the length of the normal line that links these two edges is measured for each column. Last, a camera image fully aligned with the bridge is selected, its principal vertical plane is marked on the image, and the shortest distance between the plane and the columns in the image are measured to obtain the column locations. This last step is repeated until all column locations are determined. Even if this process requires minimal user interruption, it is not fully automated due to occasional inaccuracies in semantic segmentation and edge detection procedures. Figure 3.2 summarizes the wireframe model development procedure.

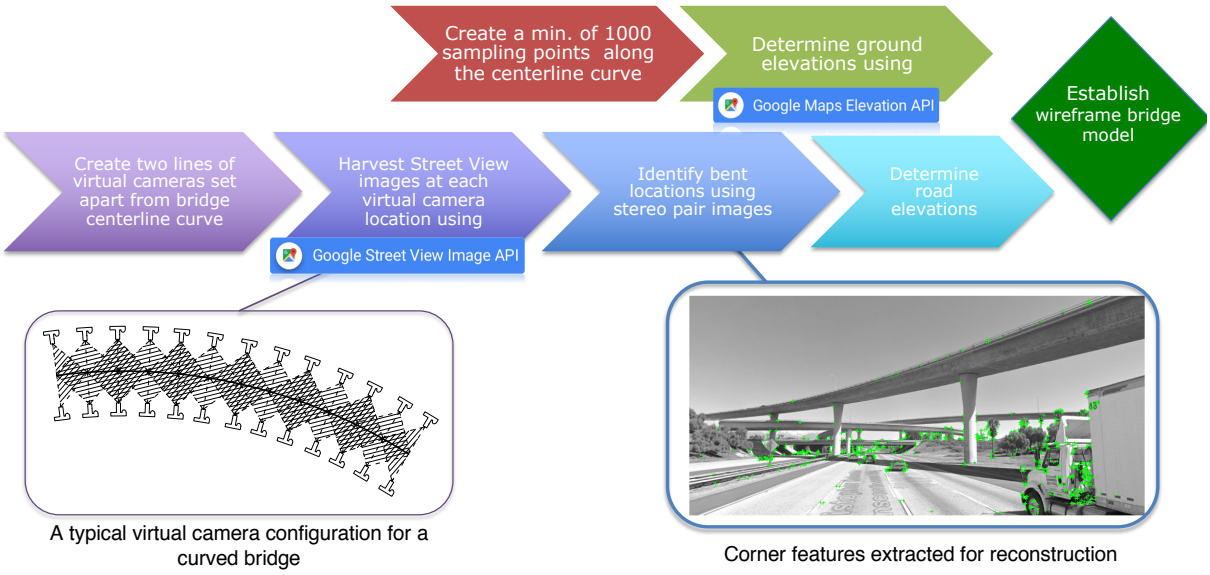

Figure 3.2: Developing the bridge wireframe model

3.4 Determination of Deck Properties

The primary assumption in defining the deck is that it remains elastic under earthquake shaking. Hence, as long as a valid estimation of the gross area of the deck can be made, the geometric properties extracted from Street View images shall be sufficient. Deck reconstruction starts with reading the deck metadata fields from NBI. One of the NBI fields gives the top width of the bridge deck. The bottom width of the deck is extracted from auto-calibrated images from the previous step. Then the horizontal alignment of the deck is extracted by automatic lookup of AASHTO code for the design year of the bridge and back-calculated based on the posted speed limit for the bridge (obtained from Google Directions API). Figures 3.3 and 3.4 summarize the deck reconstruction process.

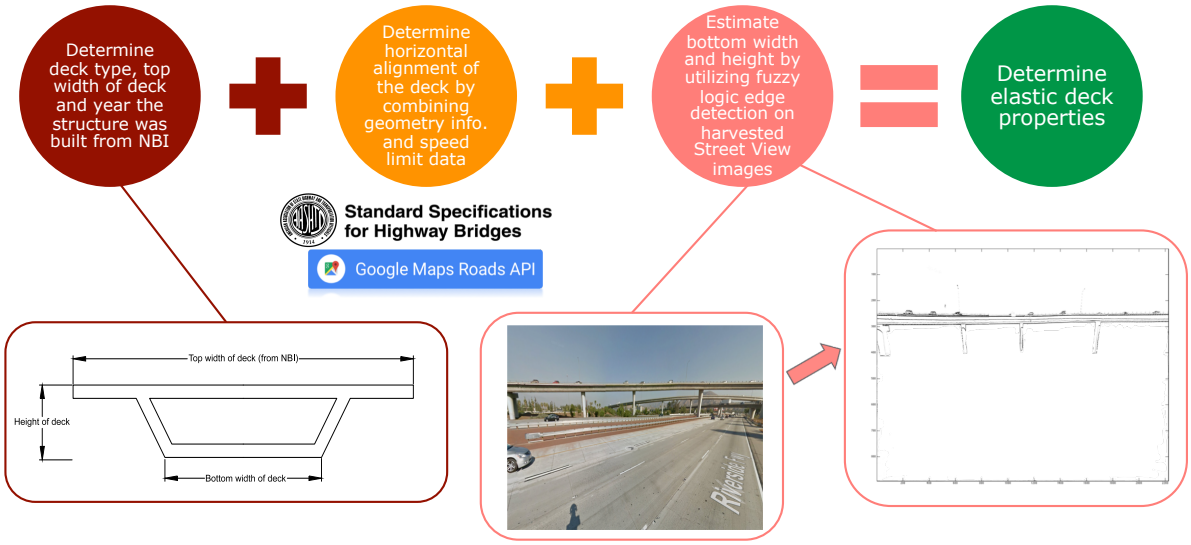

Figure 3.3: Determination of deck properties: general procedure

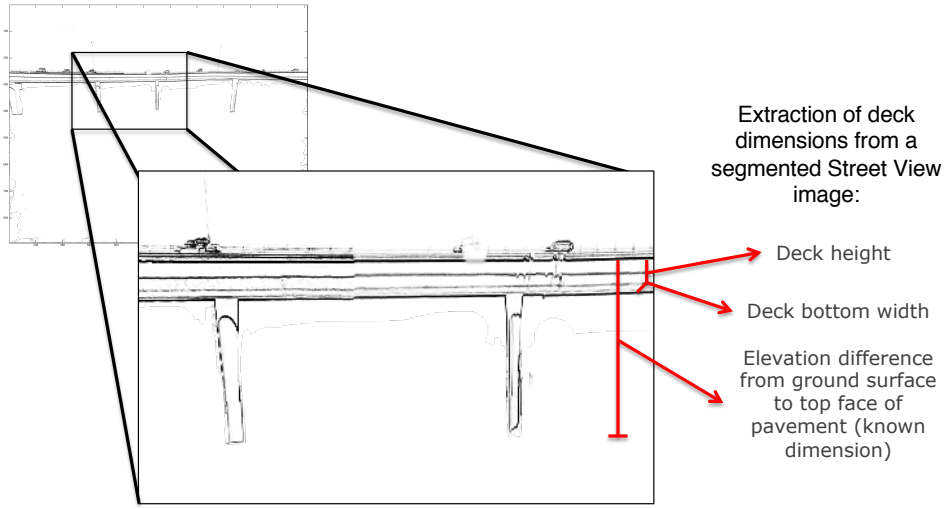

Figure 3.4: Determination of deck properties: closeup

3.5 Extraction of Column Properties

The automated extraction of column geometries consists of three primary steps. First, an edge detection algorithm is executed on segmented column patches, and the number of edges is counted (e.g., two edges if circular, three edges if rectangular). Then column heights and widths are sampled at numerous intervals to determine the column dimensions. Then using class statistics for bridge columns [55], longitudinal and transverse rebar locations are calculated. Figure 3.5 summarizes the process for extracting column shape and dimensions.

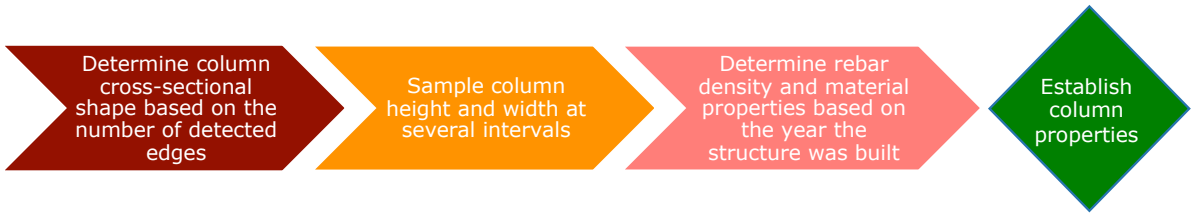

Figure 3.5: Automated extraction of column properties

3.6 Determination of in-span hinge properties

The determination of in-span hinge locations is performed identically to column location determination. The main difference is the difficulty in determining the location and gap size. Segmented patches for the deck are evaluated with a gradient change detector for location identification. However, the filter is not flawless, so seldom user interruption is required.

3.7 Case Study: Interstate-10E/Interstate-210N Interchange Bridge

A structural model of the Interstate-10E/Interstate-210N interchange bridge was developed based on the bridge's as-built drawings, and several geometric and structural characteristics were compared against its image-based model. Figures 3.6 through 3.11 display the intermediate steps of image-based modeling process as well as the final model.

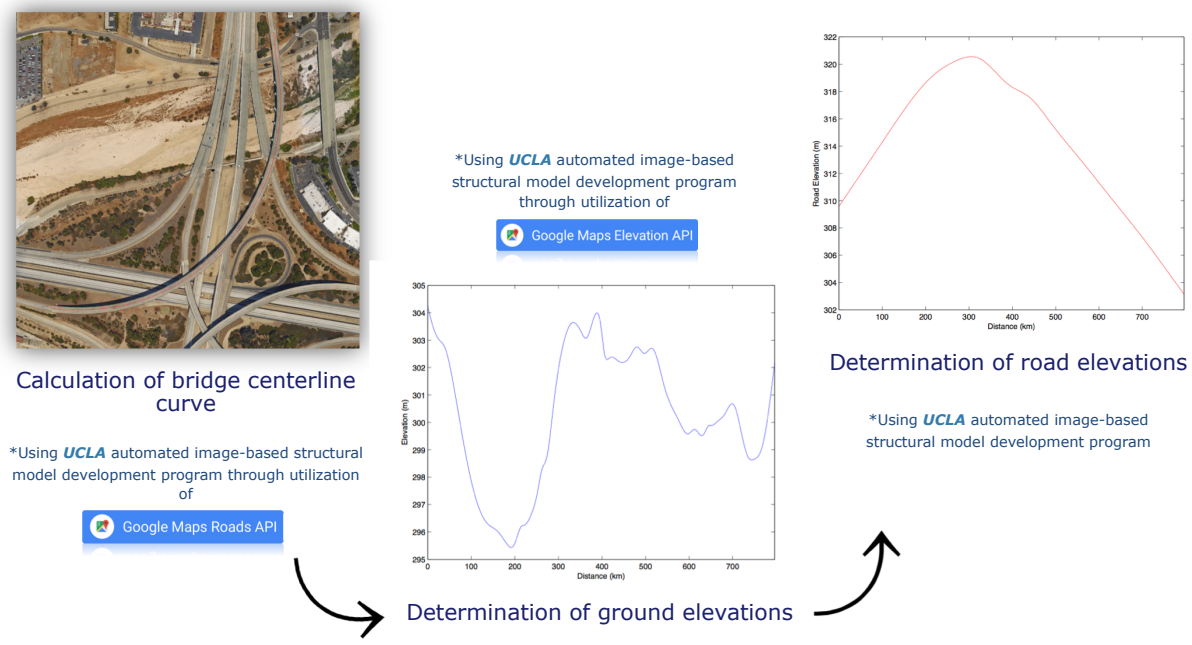

Figure 3.6: I-10E/I-210N Interchange: determination of centerline, ground and deck elevation

Identification of bent locations

*Using ***UCLA*** automated image-based structural model development program via *Image Analyzer Module*

*Using ***UCLA*** automated image-based structural model development program via *Wireframe Model Builder Module*

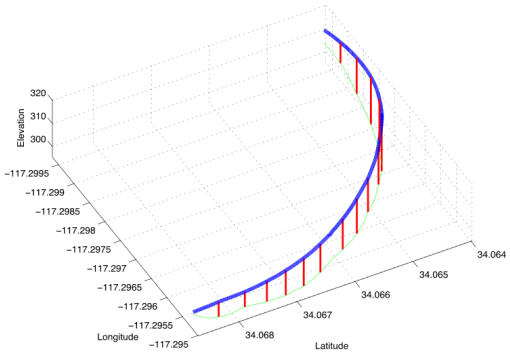

Establishing of wireframe model

Figure 3.7: I-10E/I-210N Interchange: identification of column locations, and the resulting wireframe model

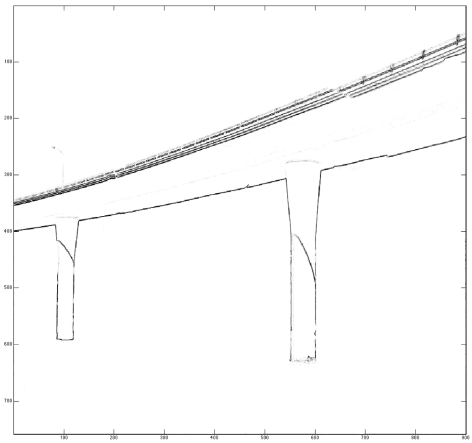

Detection of column edges

*Using ***UCLA*** automated image-based structural model development program via *Fuzzy Logic Edge Detection Module*

*Using ***UCLA*** automated image-based structural model development program via *Pixel Counter Module*

Determination of column dimensions

Figure 3.8: I-10E/I-210N Interchange: column edge detection and dimension extraction

Figure 3.9: I-10E/I-210N Interchange: identification of in-span hinge locations

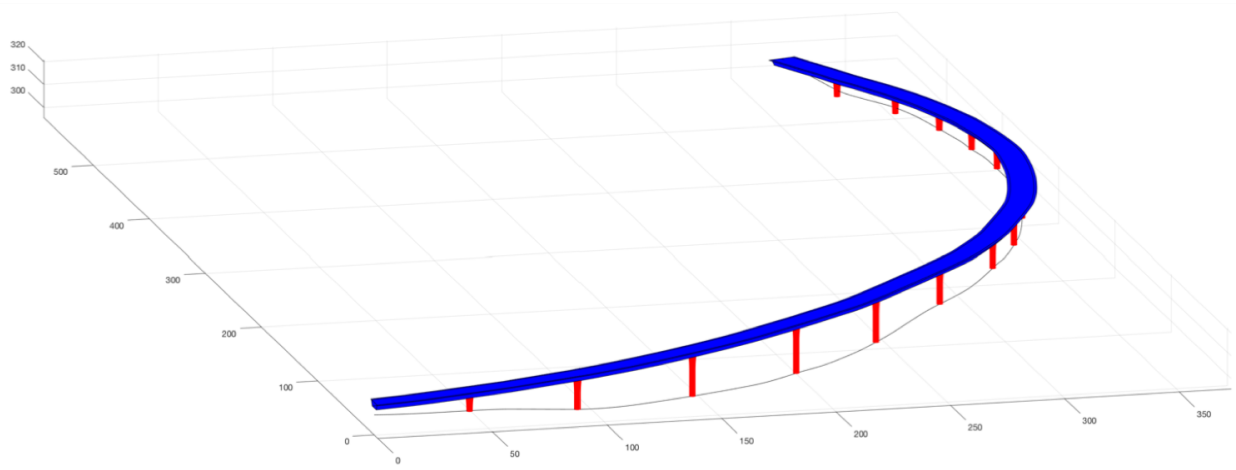

Figure 3.10: I-10E/I-210N Interchange: Full 3-D Model

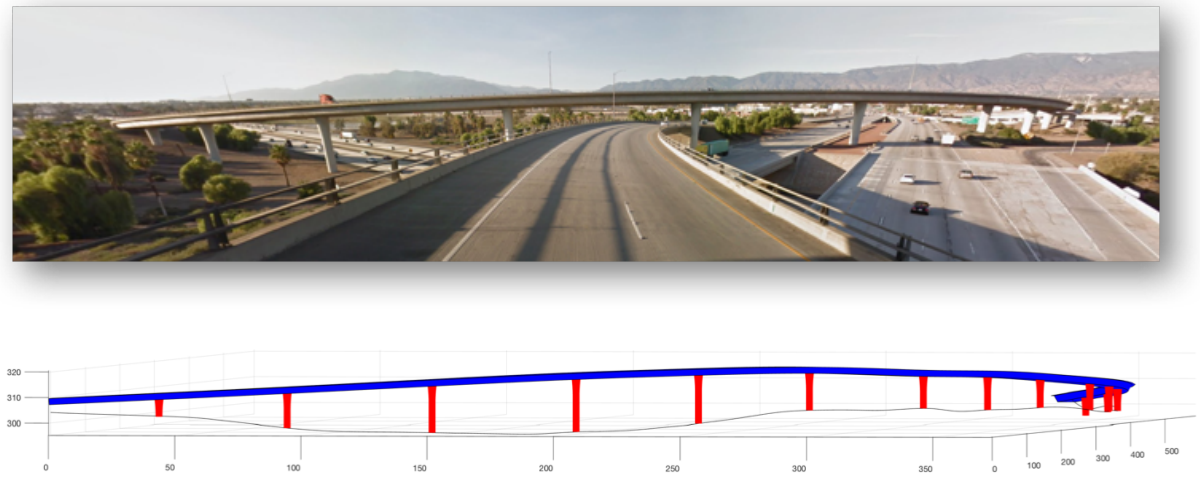

Figure 3.11: I-10E/I-210N Interchange: Full 3-D Model visual comparison against Street View image

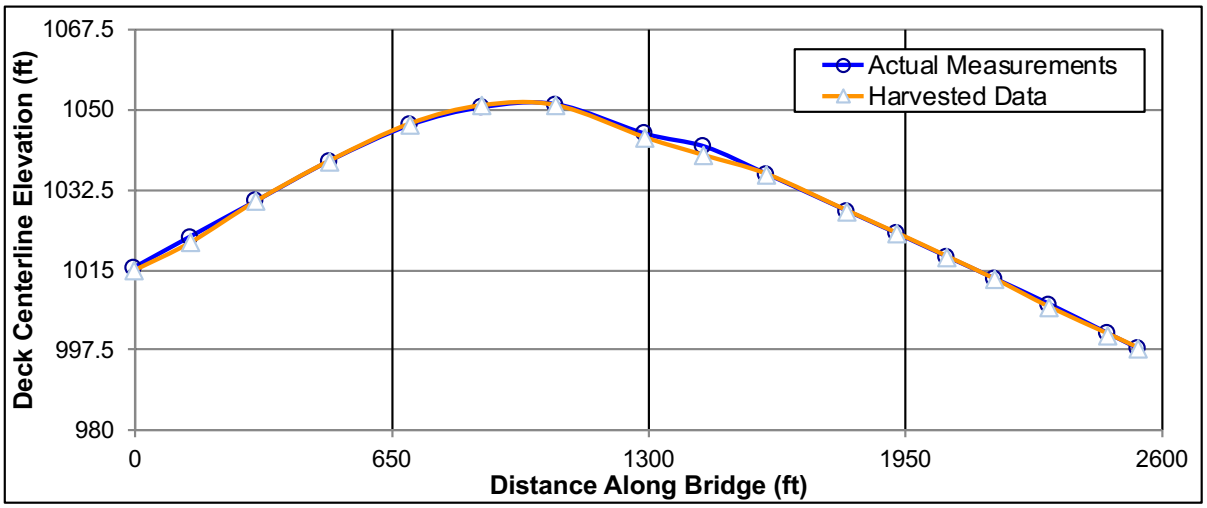

Figure 3.12: I-10E/I-210N Interchange: image-based vs. as-built deck elevation

Figures 3.12 through 3.14 compare the geometric features of the image-based model vs. the as-built model. Table 3.1 makes a comparison between the modal periods and Figure 3.15 compares collapse fragilities of the image-based model vs. the as-built model. As evident from the results, image-based results almost perfectly match the as-built geometry and closely approximates the as-built structural behavior.

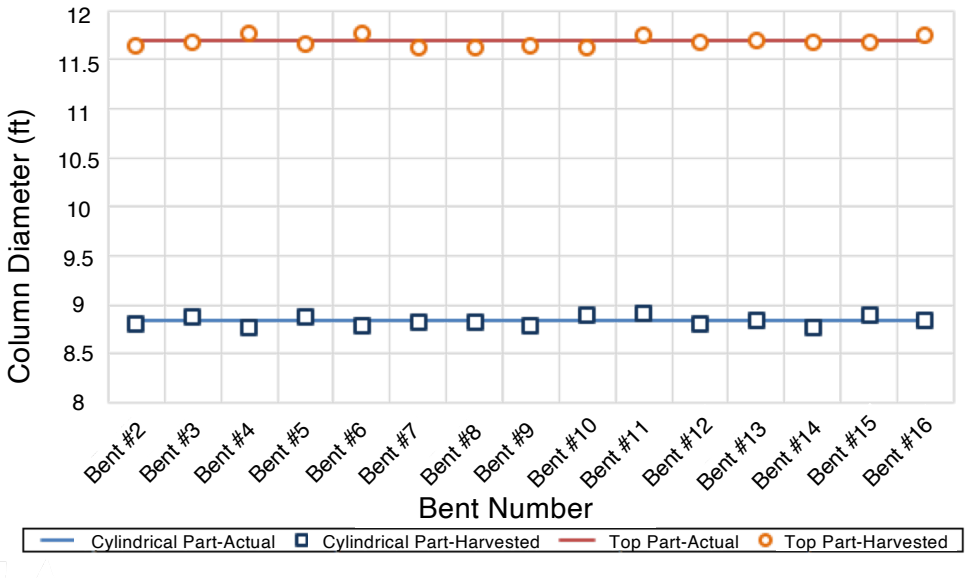

Figure 3.13: I-10E/I-210N Interchange: image-based vs. as-built column diameters

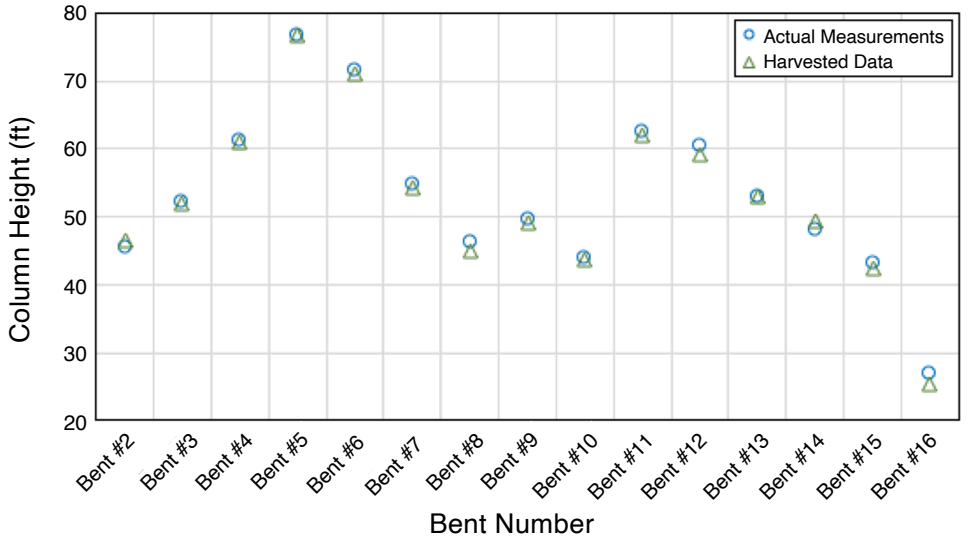

Figure 3.14: I-10E/I-210N Interchange: image-based vs. as-built column heights

Table 3.1: Image-based versus as-built: Modal Periods

	$T_{\text{image-based}}$	$T_{\text{as-built}}$
Mode 1	1.36	1.53
Mode 2	1.18	1.29
Mode 3	1.03	1.09
Mode 4	0.95	1.02
Mode 5	0.89	0.94
Mode 6	0.84	0.88
Mode 7	0.78	0.80
Mode 8	0.75	0.79

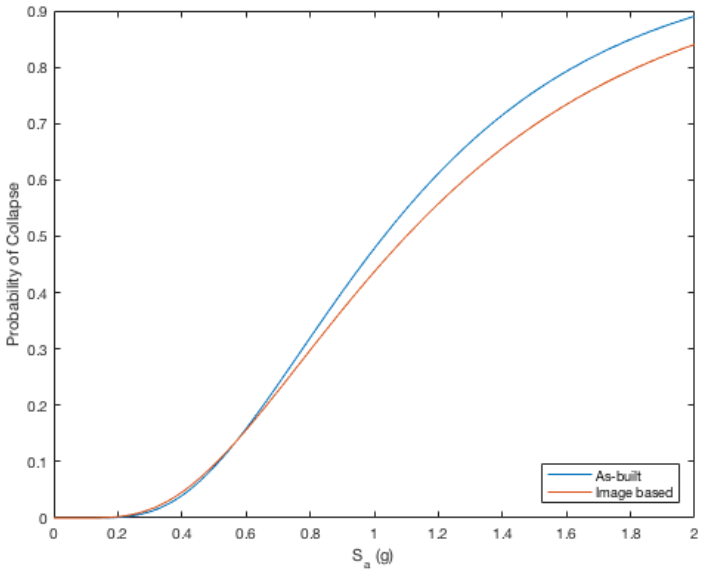

Figure 3.15: I-10E/I-210N Interchange: image-based vs. as-built collapse fragility functions

CHAPTER 4

An Investigation of Seismic Resilience of the Transportation Network Serving Los Angeles Metropolitan Area

This chapter rephrases the findings of a study performed by the author for a paper in consideration for publication [17]. At the time this document was published, the mentioned paper was under review.

4.1 Seismic Loss Assessment

Converting seismic hazards to direct physical damage comprise three main steps: (i) quantifying scenario hazard controlling the studied region, (ii) combining the ground motion intensity measures (IMs) due to the scenario event with component fragility functions to calculate the damage state probabilities for each component, and (iii) coupling the probabilities for each damage state with the corresponding recovery functions to estimate the downtime for each network component.

Computing the scenario hazard at a site requires first identifying all the events that contribute to the seismic hazard at the studied region—a process termed probabilistic seismic hazard analysis (PSHA) [56]. Subsequently, the probabilistic seismic hazard (PSH) results can be deaggregated to obtain the relative contributions of all seismic sources to that hazard for all possible magnitude and distance measures [11]. Scenario hazard is identified as the event with the highest contribution. The last step in quantifying the scenario hazard is to compute the IMs due to the determined earthquake event. This process is typically carried

out by use of ground motion prediction equations (GMPEs), such as the ones developed through the NGA-West 2 [87], and NGA East [32] projects. In general, GMPEs define the natural logarithm of a IM ($\ln Y$) in terms of a convolution of a source function (F_E), path function, (F_P), site function (F_S), and a residual term $\varepsilon_n \sigma(.)$ as

$$\ln Y = F_E(\mathbf{M}, mech) + F_P(R, \mathbf{M}, region) + F_S(V_{S30}, R, \mathbf{M}, region, Z_x) + \varepsilon_n \sigma(\mathbf{M}, R, V_{S30}) \quad (4.1)$$

where $\mathbf{M}$ is the earthquake moment magnitude, R is the rupture distance in km, V_{S30} is the time-averaged shear-wave velocity in the top 30 m of the site in m/sec, Z_x is the basin depth in km, *mech* is the fault mechanism parameter, and *region* denotes the regional correction parameter.

The main outputs of GMPEs are the IMs peak ground acceleration (PGA), peak ground velocity (PGV), and 5%-damped elastic pseudo-absolute spectral acceleration (PSA). Combining PGA with information such as liquefaction susceptibility, the ground displacement demand expected at a site can also be calculated. Each of these IMs correlate with a particular type of seismic demand and the corresponding damage to individual network components. During an earthquake, the primary factors that contribute to bridge losses are ground and structural failures, which are typically well-correlated with PGA and PSA [53], [68], respectively. Damages to tunnels, on the other hand, are caused by ground shaking, ground failure due to liquefaction, fault displacement, or slope instabilities. As such, tunnel seismic damage levels are well correlated to (and thus can be described as a function of) PGA and PGD [6].

The relationship between network components and IMs are defined using fragility functions. Fragility functions are log normally-distributed functions that give the probability of reaching or exceeding different damage states for a given IM. In performance-based earthquake engineering (PBEE) practice, damage to a network component is categorized into five damage states: no damage (ds_1), slight (ds_2), moderate (ds_3), extensive (ds_4), and complete (ds_5)[47]. Each fragility function corresponds to one of these damage states and is characterized by a median value IM (M), and a log-normal standard deviation value (β). The generic

form of a fragility function is given by

$$\Pr(D^k \geq \mathrm{ds}_j) = 1 - \Phi_j^k \left(\frac{\ln(x^k/M)}{\beta} \right) \tag{4.2}$$

where k is the index for IMs, j is the index for PBEE damage states, D^k is the damage state of network component due to IM k, Φ is the normal cumulative distribution function, and x^k is the IM k at the site of the network component. Note that the probability of a system being in or exceeding the no damage, ds_1, state is always 1 ($\Pr(D^k \geq \mathrm{ds}_1) = 1$).

An essential input for resilience assessment is the downtime estimates. Thus, for resilience studies, damage probabilities computed using fragility functions are converted into this metric. Translating bridge fragilities to downtime requires calculating the probability of network components being in one of the five damage states, and aggregating these probability measures to restoration functions that correspond to individual damage states. Open literature on restoration functions is particularly limited, and the restoration functions published by FEMA [27] are the main tool used for tying component damage information to downtime estimates. For a set of IMs, the probability of a network component being in a damage state (P_j^k) is calculated as

$$\mathrm{P}_j^k = \begin{cases} \Pr(D^k \geq \mathrm{ds}_j) - \Pr(D^k \geq \mathrm{ds}_{j+1}) & j = 1, 2, 3, 4 \\ \Pr(D^k \geq \mathrm{ds}_5) & j = 5 \end{cases} \tag{4.3}$$

For a set of IMs, expected downtime ($\mathrm{E}[D^k]$) is defined with respect to P_j^k as in

$$\mathrm{E}[D^k] = \sum_{j=1}^{5} \mathrm{P}_j^k \cdot RC_j \tag{4.4}$$

where RC_j is the recovery function corresponding to the damage state denoted by index j.

One of the novel contributions of this study is its use of detailed bridge fragility functions generated using the image-based modeling approach. The method establishes structural models of bridges via a fusion of geotagged street-level and satellite imagery, OpenStreetMaps centerline curves [67], 2018 version of National Bridge Inventory (NBI) metadata [28], Shuttle Radar Topography Mission (SRTM) 1 Arc-Second Global data [95], and class statistics for

bridge structural properties available in the literature [55]. The central premise of the method is that through auto-calibration from multiple uncalibrated street-level images, the camera matrix can be determined. Also, by semantic segmentation, individual components of a bridge can be identified in images. Subsequently, by measuring the distance between the back-projection of image origin and the image locations of components, world coordinates of the components can be computed and superimposed on the bridge centerline. Furthermore, object dimensions and deck height can be extracted, and a geometric model of the bridge can be computed. The geometric model can then be laid over the SRTM digital elevation model and populated with class statistics to attain a comprehensive structural model of the bridge.

The process of obtaining fragility functions for a bridge structure for ground shaking involves performing incremental dynamic analysis (IDE) [96] of the bridge model. By calculating the seismic response of the bridge for multiple ground motions at a range of $\mathrm{PSA}_{1.0}$ levels and comparing the demands determined for each realization against the corresponding damage thresholds for each damage, IDE computes the $\Pr(D^k \geq \mathrm{ds}_j)$. The choice of ground motion records and the damage thresholds for each damage state depends on a variety of factors. In selecting ground motions, it is crucial to use a dataset consisting of waveforms from earthquakes with magnitude and distance measures compatible with the scenario earthquake and covering a broad band of frequencies.

The key aspect of determining damage thresholds, on the other hand, is to ascertain that they are applicable to the structural systems that comprise the bridge. In this study the ground motion dataset suggested by Baker [8] and the threshold values employed by Ramanathan et al. [76] are utilized. Figure 4.1 shows several Google Street View images, 3D geometric model, and the fragility curves obtained for one of the many bridges modeled for this study.

(a) Google Street View images

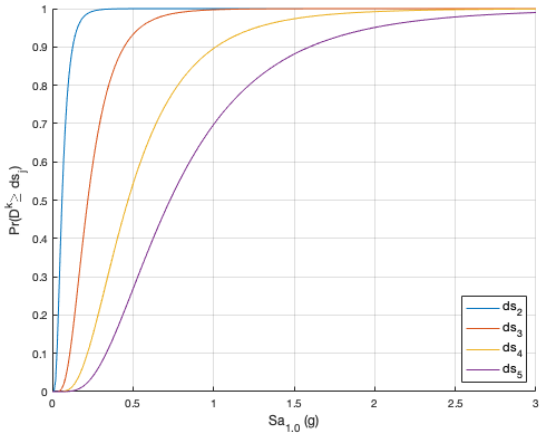

(b) Bridge fragility functions

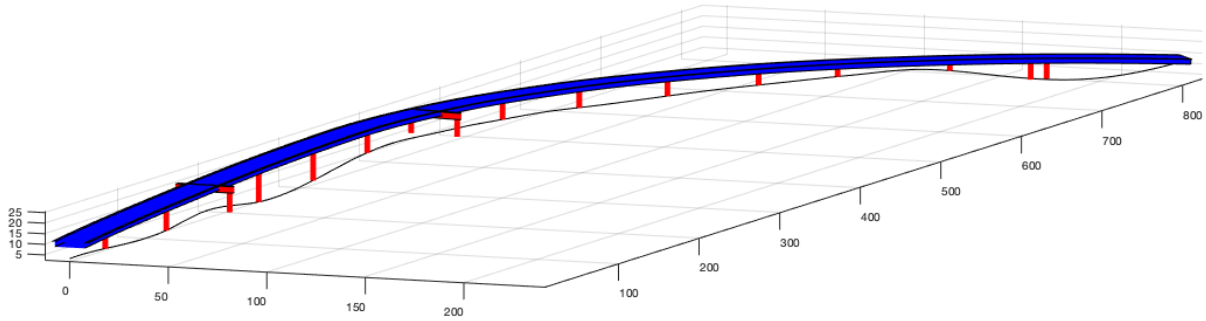

(c) 3-D geometric model

Figure 4.1: Sample Google Street View images (a), fragility functions (b), and geometric model (c) obtained for a bridge considered in this study

4.2 Network Disruptions due to Physical Damage and Its Impacts on Resilience

By using the physical damage estimates, the analysis of the transportation network disruption is realized with a multi-county scale 4-step travel demand model. Specifically, the

operational suitability of damaged system components is evaluated with respect to a threshold functionality level to simulate the post-disaster decisions made by local authorities. If the functionality level of a bridge drops beyond the specified threshold, the link corresponding to that bridge in the network model is fully closed for traffic. Physical damage data is time-dependent and explicitly considers the component-level recovery. With this information, several network topologies can be modeled to capture a timeline of the network conditions throughout the disruptions. Initial skim matrices are computed to find the OD costs for Traffic Analysis Zone (TAZ) pairs. These costs, coupled with trip production and trip attraction models, enable estimation of the number of trips generated into and from all TAZs. These trips are then balanced and distributed throughout the region among different travel modes. The calculated travel demand is then binned into individual time windows and used to assign loads into the network to solve for the traffic assignment problem.

4.2.1 Defining Network Resilience

In evaluating network-level system resilience, the following mathematical definition by Frangopol and Bocchini [30] is adopted.

$$R = \frac{1}{h}\int_0^h Q(t)dt \tag{4.5}$$

In Eq. 4.5, t denotes time in days, h is the investigated time horizon in days, and $Q(t)$ is system's functionality level at time t with respect to the baseline, i.e., pre-event network configuration. Integrating functionality over time in this manner yields the network resilience metric, R. Here, $Q(t)$ is defined in terms of percent functionality of baseline network $\Gamma(0)$ as

$$Q(t) = 1 - \frac{|\Gamma(t) - \Gamma(0)|}{\Gamma(0)}; \quad Q(t)\epsilon[0,1] \tag{4.6}$$

A number of functionality indicators, Γ, based on the total travel time spent or total travel distance covered in the system by all users are proposed in literature. In this study VHT (Vehicle-Hours-Traveled) and VHD (Vehicle-Hours-Delayed) are utilized. For each of these

indicators, Γ_i(t) can be calculated as

$$\Gamma(t) = \sum_{k=1}^{\#\text{ of links}} \gamma_k(t); \quad \gamma_k(t) \epsilon \mathbb{R}^+ \tag{4.7}$$

4.2.2 SCAG Regional Travel Demand Model

The transportation system analyses were performed using the regional travel demand model (RTDM) developed by the Southern California Association of Governments (SCAG) [86]. The peer-reviewed model is validated with a number of independent sources of travel data including automobile and truck traffic counts, transit boarding counts, Vehicle Miles of Travel (VMT) from Highway Performance Monitoring System (HPMS), and speed data from Freeway Performance Measurement System (PeMS). Figure 4.2 provides a sample of the high resolution in SCAG RTDM. It encompasses an vehicle ownership model, advanced mode and destination choice models, a highly granular 2-tier TAZ system containing the 11,000 TAZs in the 6-county SCAG study region, trip market strata defined by car sufficiency, and household income groups used throughout the entire demand models for 10 trip purposes. It is calibrated with respect to the California Household Travel surveys and other major data sources. It provides a Heavy Duty Truck model and contains a high-occupancy-vehicle (HOV) diversion model splitting carpool trips from vehicles on the general purpose lanes. For detailed discussions regarding the data sources and the modeling efforts related to SCAG RTDM, readers are referred to the model validation report published by SCAG [86].

4.3 Case Study: Magnitude 7.3 Earthquake on Palos Verdes Fault

4.3.1 Hazard Characterization

Without losing generality, a scenario earthquake that poses a significant seismic risk to the Ports of Los Angeles and Long Beach (also known as San Pedro Bay port complex) is considered. The port complex forms one of the world's busiest seaport handling more containers per ship call than any other port complex in the world. The complex comprises 32% of the

Figure 4.2: High resolution, multi-modal network model underlying the SCAG RTDM

total national market; hence, potential interruptions to its operations bear significance to more than just the City of Los Angeles. In order to quantify the scenario hazard controlling the area where the port facilities are located, the PSH results from the 2014 version of U.S. Conterminous Seismic Hazard Maps [69] are deaggregated. Based on the deaggregation of the PSH for a 975-year return period (Figure 4.3b, the Palos Verdes fault was found to govern the seismic hazard for the complex. Palos Verdes fault is a predominantly right-lateral strike-slip fault system extending in northwest-southeast direction for more than 100 km [14]. According to the deaggregated hazard results, the moment magnitude with the highest contribution to the overall hazard is determined as 7.3. As such, throughout the scenario hazard calculations conducted for this study, a magnitude 7.3 earthquake generated by a

portion of the Palos Verdes fault line is used. Figure 4.3(a) displays the PSHA results for the epicentral location of the defined scenario event.

In order to simplify that calculation of damages resulting from the scenario event, the effect of earthquakes are limited to ground shaking only. Thus, the IMs required for direct damage analyses consisted of 0.3 sec and 1.0 sec spectral accelerations ($SA_{0.3}$ and $PSA_{1.0}$ respectively) for HAZUS predictions and $PSA_{1.0}$ and for image-based model predictions for the physical damage. The weighted average of the median SA values computed from 2013 GMPEs by Abrahamson et al., Boore et al., Campbell and Bozorgnia, Chiou and Youngs, and Idriss with weights for the first four equations set to 0.22 and the last one set 0.12. Site effects are taken into account using the slope-based V_{S30} proxy method suggested by Wald, whereas the basin effects were neglected for all site locations. Given the V_{S30} map computed by Thompson et al. [90], and the position of the study region on the Los Angeles basin, both of these assumptions are warranted. Figures 4.4a and 4.4b show maps of the $PSA_{1.0}$ resulting from the scenario event.

4.3.2 Damage Assessment

For the assessment of physical damage, 98 bridges in the immediate periphery of the port complex were modeled using the image-based modeling procedure mentioned above (Figure 4.5). For all other bridges in the area, HAZUS fragility functions [27], created using the 2018 NBI data [28], are utilized. Damage state probabilities for each bridge in the study region are computed using Eq. (4.3) for ds_1 through ds_5. Subsequently, HAZUS bridge restoration functions [27] and Eq. (4.4) are utilized to calculate the downtime associated with the defined scenario event. Figures 4.6a and 4.6d show maps of the computed downtimes. It is observed that the bridge downtimes are highest around the rupture port facilities due to the proximity of the scenario event to the complex. However, it is possible to observe bridge closures as far as the Marina Del Rey area. Authors believe that the reason for such damage occurrences is because of the coupled effect of increased ground shaking levels due to the presence of softer soil deposits and pre-1971 construction of the structures.

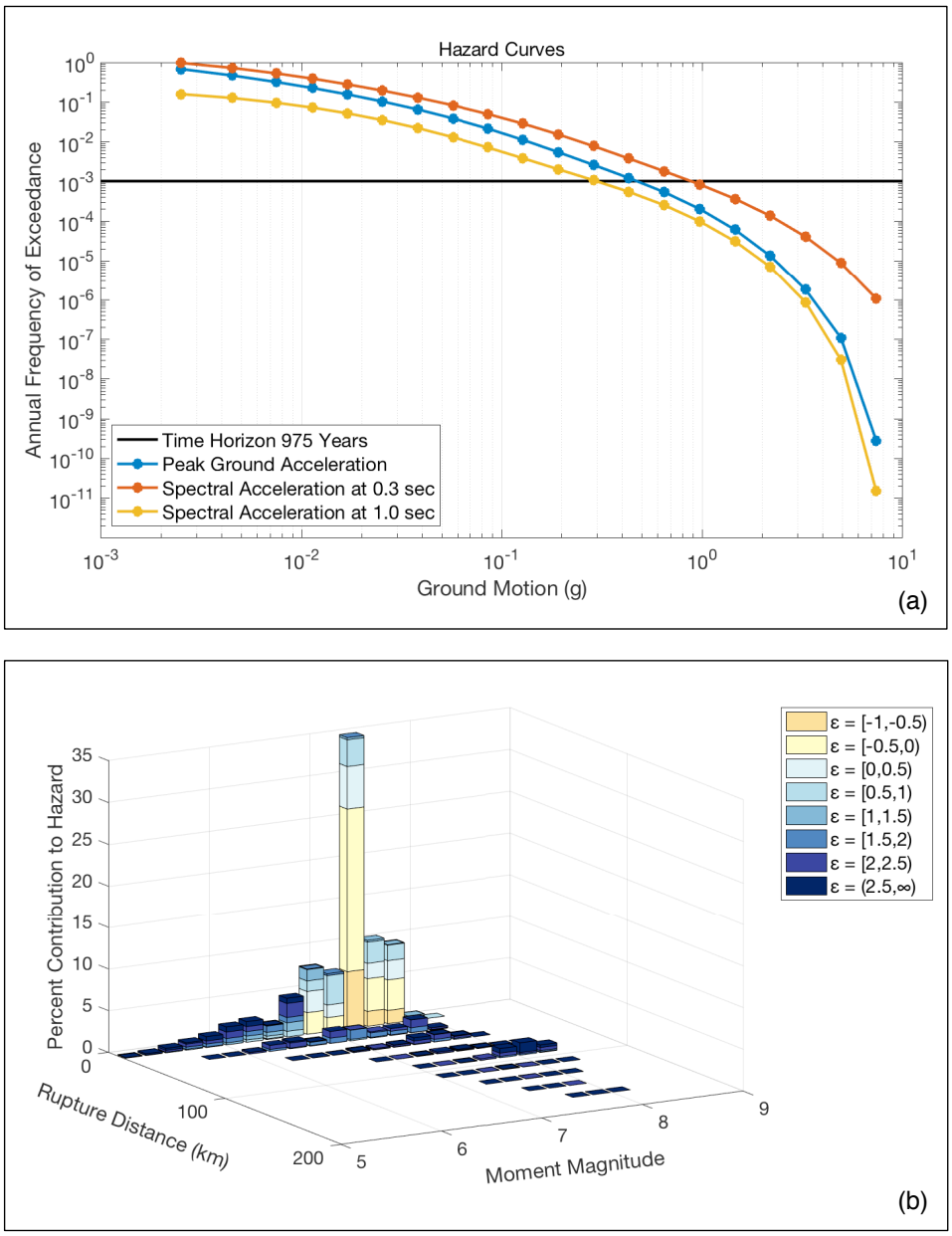

Figure 4.3: (a) PSHA results for the Ports of Los Angeles and Long Beach, and (b) their deaggregation

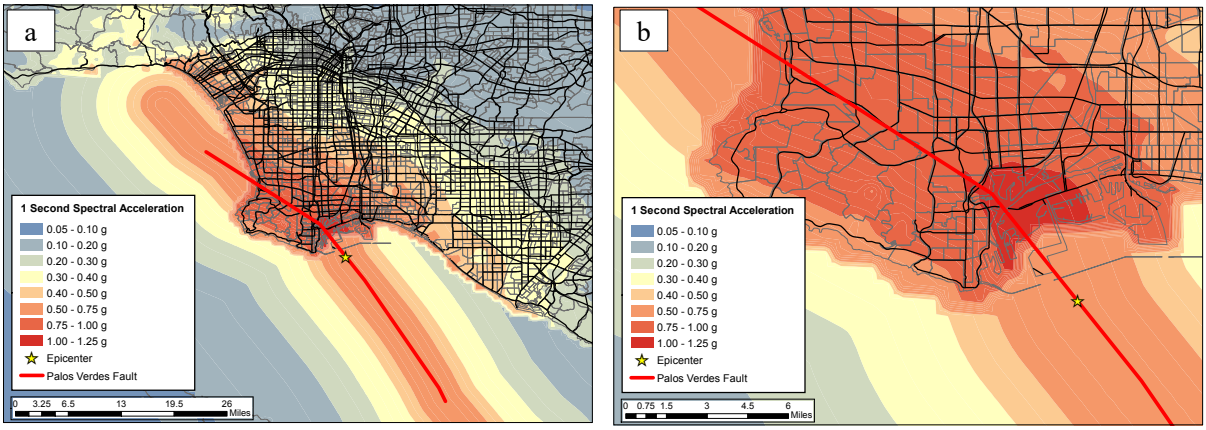

Figure 4.4: Scenario-based hazard results for 1.0 sec spectral accelerations at the general study region level (a), and 1.0 sec spectral acceleration results around the rupture length (b)

4.3.3 Transportation Network Analysis

Based on the functionality levels determined from the scenario hazard for each bridge, baseline network topology was modified to reflect the damages expected for Days 1, 7, 30, 90, and 104 after the earthquake. In other words, in each of the five network versions, any link with the functionality less than 75% was considered closed for traffic, as defined in Gordon et al. [31], and the remaining links were preserved as-is. Based on this criterion, the number of bridge closures at each time instant is determined as summarized in Table 4.1. On Day 105, full recovery of network components is achieved and baseline network functionality re-established.

Table 4.1: Number of bridges closed at evaluated time instants

Instant After Earthquake	Number of Bridges Closed
Day 1	137
Day 7	62
Day 30	58
Day 90	45
Day 104	19

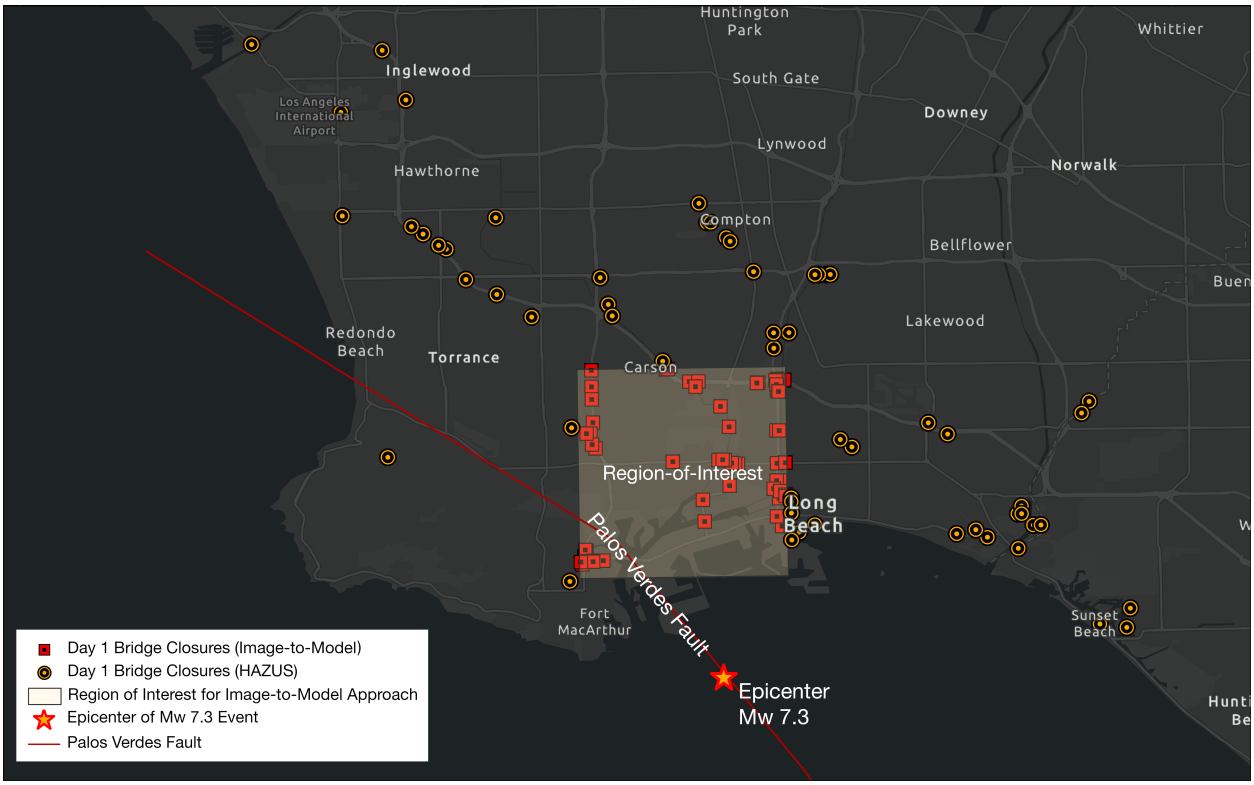

Figure 4.5: Modeled bridge closures on Day 1. Region-of-Interest contains bridges modeled with the image-to-model methodology discussed in Chapters 2 and 3

In order to compute the changes in system functionality, including the baseline network, six distinct complete traffic distribution and assignment problems are solved. In this study, system functionality is only quantified in terms of travel time indicators VHT and VHD.

Figures 4.7 and 4.8 display system functionality, $Q(t)$, based on VHT and VHD, respectively. Functionality levels are presented for all six counties within the SCAG study region as well as the entire Los Angeles metro area. Evidently, counties located far away from the epicenter of the scenario earthquakes experience far less significant disruptions. In terms of VHT, performed analyses estimate a total of $850,000$ hours/day additional travel time for morning commuters, corresponding to a 6.52% decrease in network functionality. As exhibited in Figure 4.8, Los Angeles County bears most of this functionality loss with a 37.89% peak loss in functionality.

Figures 4.9 and 4.10 illustrate the reconfiguration of vehicle flow during the peak morning

Figure 4.6: The location of damaged bridges within the general study region (a), and along the rupture length color-coded in terms of downtimes (b)

traffic on Days 1 and 7 after the event, in comparison to the baseline network conditions. It is observed that detours resulting from bridge closures on high volume corridors (e.g., Interstate highways 110, 710, and 405) around the ports shift the flow to the surface streets, thereby forcing high volume traffic to drive through neighbourhoods surrounding the ports.

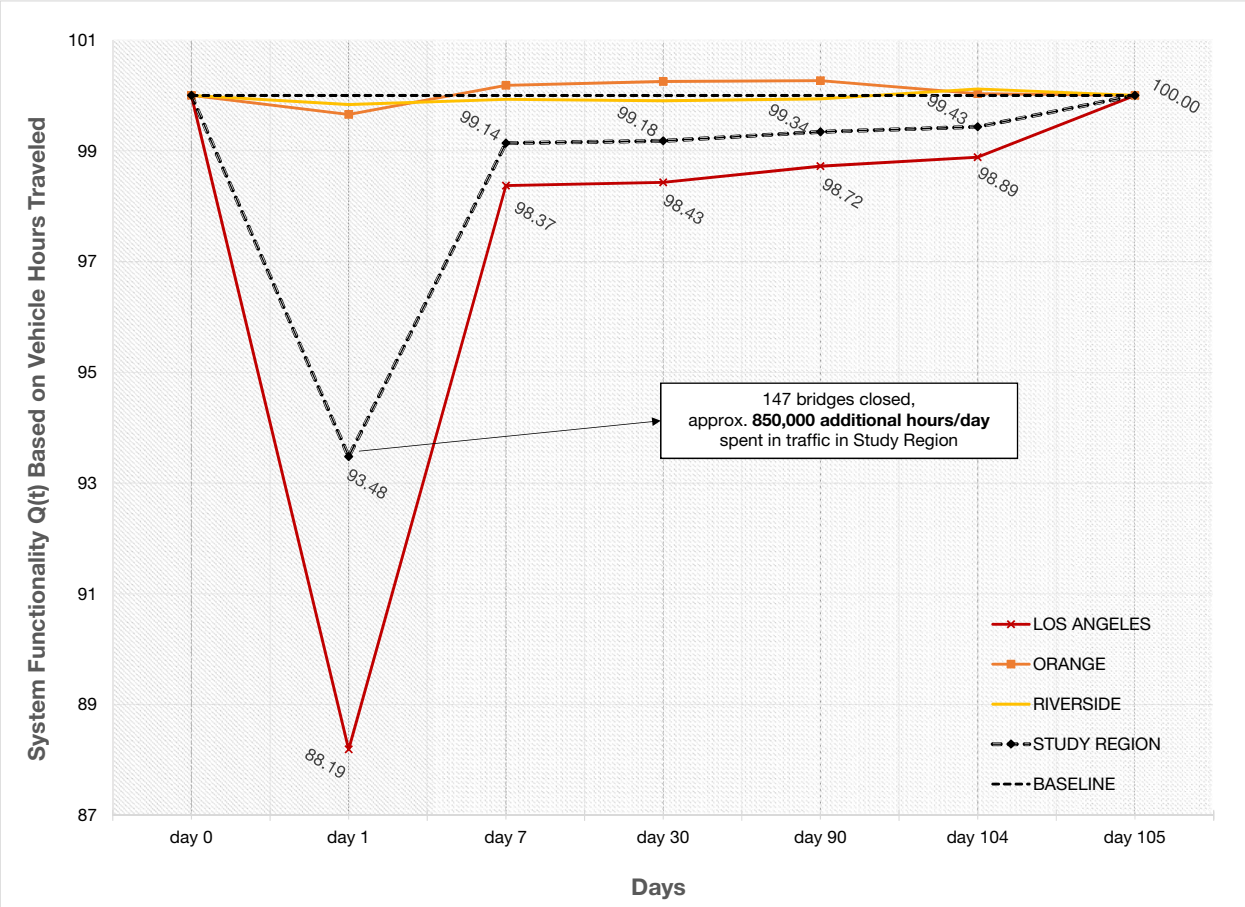

Figure 4.7: System functionality based on Vehicle Hours Traveled

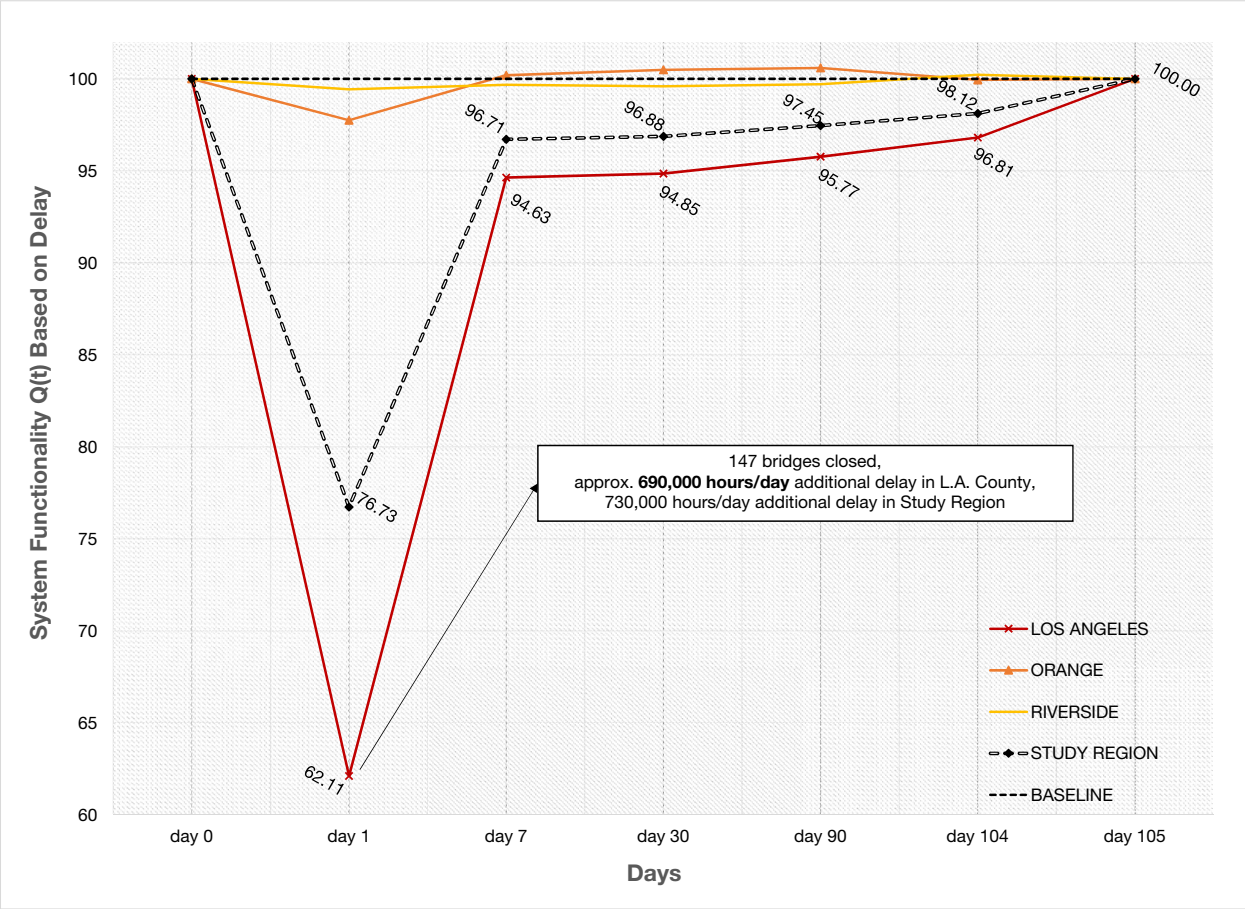

Figure 4.8: System functionality based on Vehicle Hours Delayed

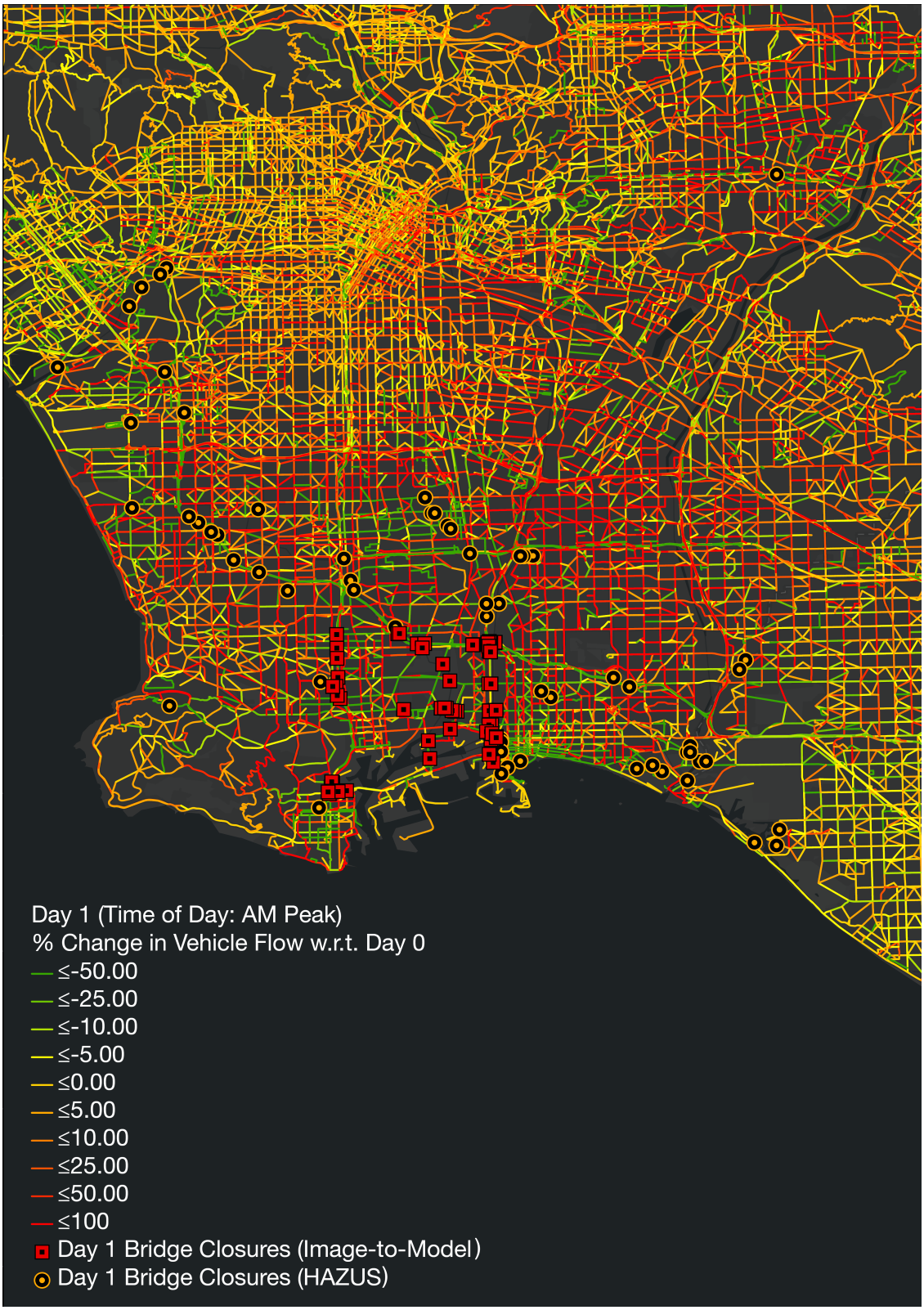

Figure 4.9: Changes in morning peak vehicle flow with respect to baseline traffic conditions on the day after the event

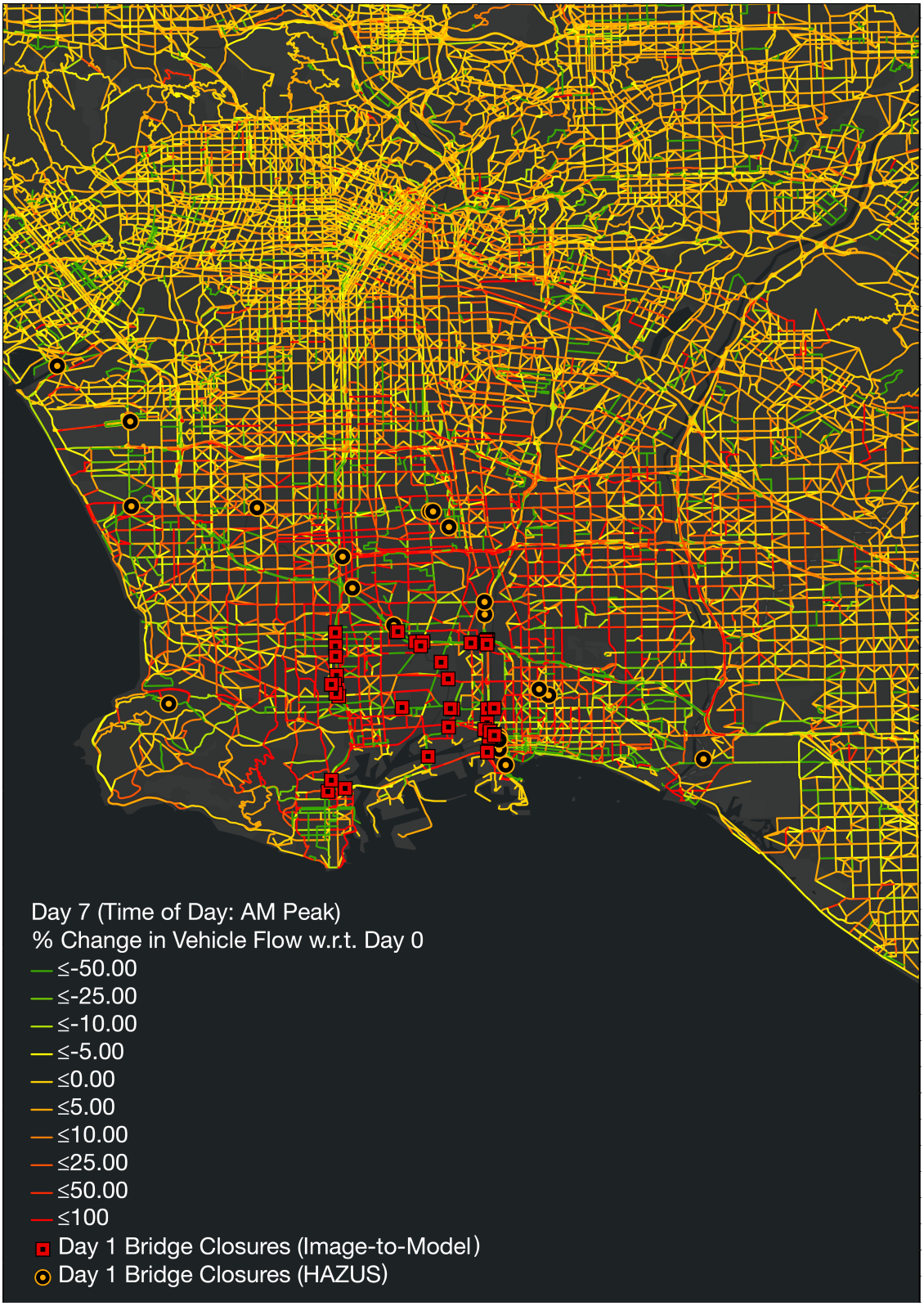

Figure 4.10: Changes in morning peak vehicle flow with respect to baseline traffic conditions seven days after the event

CHAPTER 5

Conclusions and Future Directions

In this study, a framework for developing image-based models of bridge structures was established, and its potential use for regional hazard assessment applications was presented. Based on the verification study performed to test the accuracy of the models generated using the framework, it was concluded that the framework is capable of generating extremely accurate bridge models, both from geometric and structural standpoint. Furthermore, a case study for Ports of Los Angeles and Long beach was presented to demonstrate a practical use for the bridge inventory data that can be developed through the proposed framework. For the case study, infrastructure damage determined using image-based methodology was coupled with the highly granular regional travel demand model developed by SCAG for the Los Angeles Metropolitan Area. As expected, the impact of the port traffic was mostly observed in the City of Los Angeles. Nonetheless, although not as significant, the repercussions of the disruptions around the port to other counties were also successfully captured.

The procedures and results presented here form the groundwork of a framework for improving the accuracy of regional-level hazard assessment studies. At the time this study was presented, the framework was not capable of generating models in a fully automated way. Thus a critical advancement to the methodology could be to enhance the utilized segmentation procedures. Although not directly related to the model generation process, translating fragility information to physical damage and functionality is another aspect of the framework that requires improvements. At its current state, seismic soil behavior is represented using lumped elements. Given the framework is able to capture surface topology in detail, developing finite elements coupled with the structural bridge models is another future aspiration for the framework. Finally, the author believes that the bridge capacity

can be better modeled in developing fragility functions using a stress-based approach (as opposed to using damage threshold values to compute damage state probabilities).

BIBLIOGRAPHY

[1] ACI-ASCE Committee 426. The Shear Strength of Reinforced Concrete Members. *Journal of the Structural Division*, 99(6):1091–1187, 1973.

[2] Panos Achlioptas, Olga Diamanti, Ioannis Mitliagkas, and Leonidas Guibas. Learning Representations and Generative Models for 3D Point Clouds, jul 2017.

[3] Charu C. Aggarwal. *Outlier Analysis*. Springer International Publishing, Cham, Switzerland, 2017.

[4] Timothy D. Ancheta, Robert B. Darragh, Jonathan P. Stewart, Emel Seyhan, Walter J. Silva, Brian S. J. Chiou, Katie E. Wooddell, Robert W. Graves, Albert R. Kottke, David M. Boore, Tadahiro Kishida, and Jennifer L. Donahue. PEER NGA-West2 Database. Technical Report 2013/03, Pacific Earthquake Engineering Research Center, Berkeley, CA, 2013.

[5] Applied Technology Council. FEMA P-646: Guidelines for Design of Structures for Vertical Evacuation from Tsunamis. Technical report, FEMA, Washington D.C., 2019.

[6] SA Argyroudis and KD Pitilakis. Seismic fragility curves of shallow tunnels in alluvial deposits. *Soil Dynamics and Earthquake Engineering*, 35:1–12, 2012.

[7] Ady Aviram, Kevin R. Mackie, and Bozidar Stojadinovic. Guidelines of Nonlinear Analysis of Bridge Structures in California. Technical Report 2008/03, Pacific Earthquake Engineering Research Center, Berkeley, CA, 2008.

[8] Jack W. Baker, Ting Lin, Shrey K Shahi, and Nirmal Jayaram. New Ground Motion Selection Procedures and Selected Motions for the PEER Transportation Research Program. Technical Report 2011/03, Pacific Earthquake Engineering Research Center, Berkeley, CA, 2011.

[9] D. H. Ballard. Generalizing the Hough transform to detect arbitrary shapes. *Pattern Recognition*, 13(2):111–122, 1981.

[10] Herbert Bay, Andreas Ess, Tinne Tuytelaars, and Luc Van Gool. Speeded-Up Robust Features (SURF). *Computer Vision and Image Understanding*, 110(3):346–359, jun 2008.

[11] Paolo Bazzurro and C. Allin Cornell. Disaggregation of seismic hazard. *Bulletin of the Seismological Society of America*, 89(2):501–520, 1999.

[12] Paul J. Besl and Ramesh C. Jain. Segmentation Through Variable-Order Surface Fitting. *IEEE Transactions on Pattern Analysis and Machine Intelligence*, 10(2):167–192, 1988.

[13] Josep Miquel Biosca and José Luis Lerma. Unsupervised robust planar segmentation of terrestrial laser scanner point clouds based on fuzzy clustering methods. *ISPRS Journal of Photogrammetry and Remote Sensing*, 63(1):84–98, jan 2008.

[14] Daniel S. Brothers, James E. Conrad, Katherine L. Maier, Charles K. Paull, Mary McGann, and David W. Caress. The Palos Verdes Fault offshore Southern California: Late Pleistocene to present tectonic geomorphology, seascape evolution, and slip rate estimate based on AUV and ROV surveys. *Journal of Geophysical Research: Solid Earth*, 120(7):4734–4758, jul 2015.

[15] N. Bruno and R. Roncella. Accuracy Assessment of 3D Models Generated from Google Street View Imagery. In *ISPRS Annals of the Photogrammetry, Remote Sensing and Spatial Information Sciences*, volume 42-2/W9, pages 181–188. Copernicus GmbH, jan 2019.

[16] Richard J. Campbell. Weather-Related Power Outages and Electric System Resiliency. Technical report, Congressional Research Service, Washington D.C., 2012.

[17] Barbaros Cetiner, Rose Adam Koc, Eyuphan, Lucio Soibelman, Ertugrul Taciroglu, and Dan Wei. CRAFT: Comprehensive Resilience Assessment for Transportation Systems in Metropolitan Areas. In review.

[18] Gilberto Axel Chang and John B. Mander. Seismic Energy Based Fatigue Damage. Analysis of Bridge Columns: Part 1 - Evaluation of Seismic Capacity. Technical report, National Center for Earthquake Engineering Research, Buffalo, NY, 1994.

[19] Ondřej Chum and Jiří Matas. Matching with PROSAC - Progressive sample consensus. In *2005 IEEE Computer Society Conference on Computer Vision and Pattern Recognition (CVPR 2005)*, volume I, pages 220–226. IEEE Computer Society, 2005.

[20] Riley Chung. January 17, 1995 Hyogoken-Nanbu (Kobe) Earthquake: Performance of Structures, Lifelines, and Fire Protection Systems (NIST SP 901). Technical report, National Institute of Standards and Technology, Gaithersburg, MD, 1996.

[21] Dorin Comaniciu and Peter Meer. Mean shift: A robust approach toward feature space analysis. *IEEE Transactions on Pattern Analysis and Machine Intelligence*, 24(5):603–619, may 2002.

[22] Elkin Díaz and Henry Arguello. An algorithm to estimate building heights from Google street-view imagery using single view metrology across a representational state transfer system. In Kevin G Harding and Song Zhang, editors, *Dimensional Optical Metrology and Inspection for Practical Applications V*, volume 9868, pages 58–65. International Society for Optics and Photonics, SPIE, 2016.

[23] Michael L. Dolfman, Solidelle Fortier Wasser, and Bruce Bergman. The Effects of Hurricane Katrina on the New Orleans Economy. *Monthly Labor Review*, 130(3):3–18, 2007.

[24] Sander Oude Elberink, Jantien Stoter, Hugo Ledoux, and Tom Commandeur. Generation and dissemination of a national virtual 3D city and landscape model for the Netherlands. *Photogrammetric Engineering and Remote Sensing*, 79(2):147–158, 2013.

[25] Federal Emergency Management Agency. *Hazus–MH 2.1 Hurricane Model Technical Manual*. Washington D.C., 2003.

[26] Federal Emergency Management Agency. Summary Report on Building Performance: Hurricane Katrina 2005. Technical Report FEMA 548, FEMA, Washington D.C., 2006.

[27] FEMA. *Hazus-MH 2.1 Technical Manual: Earthquake Model*. Federal Emergency Management Agency, Washington, DC, 2003.

[28] FHWA. Recording and coding guide for the structure inventory and appraisal of the nation's bridges. Technical Report FHWA-PD-96-001, Department of Transportation, Federal Highway Administration, Washington, D.C., 1995.

[29] Martin A. Fischler and Robert C. Bolles. Random sample consensus: A Paradigm for Model Fitting with Applications to Image Analysis and Automated Cartography. *Communications of the ACM*, 24(6):381–395, jun 1981.

[30] Dan Frangopol and Paolo Bocchini. Resilience as Optimization Criterion for the Rehabilitation of Bridges Belonging to a Transportation Network Subject to Earthquake. *Structures Congress*, pages 2044–2055, 2011.

[31] Peter Gordon, James E Moore II, Harry W Richardson, Masanobu Shinozuka, Donghwan An, and Sungbin Cho. Earthquake Disaster Mitigation for Urban Transportation Systems: An Integrated Methodology that Builds on the Kobe and Northridge Experiences. *Modeling Spatial and Economic Impacts of Disasters*, pages 205–232, 2004.

[32] Christine Goulet, Yousef Bozorgnia, Norman Abrahamson, Nicolas Kuehn, Linda Al Atik, Robert Youngs, Robert Graves, and Gail Atkinson. Central and Eastern North America Ground-Motion Characterization - NGA-East Final Report. Technical Report 2018/08, Pacific Earthquake Engineering Research Center, Berkeley, CA, 2018.

[33] Pedro Hermosilla, Tobias Ritschel, Pere Pau Vázquez, Àlvar Vinacua, and Timo Ropinski. Monte Carlo convolution for learning on non-uniformly sampled point clouds. *ACM Transactions on Graphics*, 37(6):Article 235, dec 2018.

[34] Francis Begnaud Hildebrand. *Introduction to Numerical Analysis*. Dover Publications, New York, NY, 2 edition, 1987.

[35] Heiko Hirschmüller. Stereo processing by semiglobal matching and mutual information. *IEEE Transactions on Pattern Analysis and Machine Intelligence*, 30(2):328–341, feb 2008.

[36] Thomas L. Holzer. The 1995 Hanshin-Awaji (Kobe), Japan, Earthquake. *GSA TODAY*, 5(8):154–167, 1995.

[37] Harold Hotelling. Analysis of a complex of statistical variables into principal components. *Journal of Educational Psychology*, 24(6):417–441, 1933.

[38] Hui Huang, Shihao Wu, Minglun Gong, Daniel Cohen-Or, Uri Ascher, and Hao Richard Zhang. Edge-aware point set resampling. *ACM Transactions on Graphics*, 32(1), jan 2013.

[39] Matias A. Hube and Khalid M. Mosalam. Experimental and Computational Evaluation of Current and Innovative In-Span Hinge Details in Reinforced Concrete Box-Girder Bridges - Part 1: Experimental Findings and Pre-Test Analysis. Technical Report 2008/103, Pacific Earthquake Engineering Research Center, Berkeley, CA, 2008.

[40] Earth Mechanics Inc. Field Investigation Report for Abutment Backfill Characterization. Technical Report SSRP-05/02, University of California, San Diego, Los Jolla, CA, 2005.

[41] Yigit Isbiliroglu, Ricardo Taborda, and Jacobo Bielak. Coupled soil-structure interaction effects of building clusters during earthquakes. *Earthquake Spectra*, 31(1):463–500, feb 2015.

[42] I. Demir Karsan and James O. Jirsa. Behavior of Concrete Under Compressive Loadings. *ASCE Journal of the Structural Division*, 95(12):2543–2564, 1969.

[43] Peyman Kaviani, Farzin Zareian, and Ertugrul Taciroglu. Performance-Based Seismic Assessment of Skewed Bridges. Technical Report 2014/01, Pacific Earthquake Engineering Research Center, Berkeley, CA, 2014.

[44] Payman Khalili-Tehrani, Anoosh Shamsabadi, Jonathan P. Stewart, and Ertugrul Taciroglu. Backbone curves with physical parameters for passive lateral response of homogeneous abutment backfills. *Bulletin of Earthquake Engineering*, 14(11):3003–3023, nov 2016.

[45] Yong Chul Kim, Akihito Yoshida, and Yukio Tamura. Influence of Surrounding Buildings on Wind Loads Acting on Low-Rise Building. *Journal of Structural Engineering*, 139(2):275–283, feb 2013.

[46] Charles A. Kircher, Robert V. Whitman, and William T. Holmes. HAZUS Earthquake Loss Estimation Methods. *Natural Hazards Review*, 7(2):45–59, may 2006.

[47] Anne Kiremidjian, J. Moore, Yue Yue Fan, Nesrin Basoz, Ozgur Yazali, and Meredith Williams. Highway Demonstration Project. Technical Report 2006/02, Pacific Earthquake Engineering Research Center, Berkeley, CA, 2006.

[48] Hannes Kisner and Ulrike Thomas. Segmentation of 3D point clouds using a new spectral clustering algorithm without a-priori knowledge. In *Proceedings of the 13th International Joint Conference on Computer Vision, Imaging and Computer Graphics Theory and Applications (VISIGRAPP 2018)*, volume 4, pages 315–322. SciTePress, 2018.

[49] Florent Lafarge and Clément Mallet. Creating large-scale city models from 3D-point clouds: A robust approach with hybrid representation. *International Journal of Computer Vision*, 99(1):69–85, aug 2012.

[50] Carsten Lange and Konrad Polthier. Anisotropic smoothing of point sets. *Computer Aided Geometric Design*, 22(7):680–692, 2005.

[51] Yangyan Li, Rui Bu, Mingchao Sun, Wei Wu, Xinhan Di, and Baoquan Chen. PointCNN: Convolution On X-Transformed Points. In S Bengio, H Wallach, H Larochelle, K Grauman, N Cesa-Bianchi, and R Garnett, editors, *Advances in Neural Information Processing Systems 31 (NIPS 2018)*, pages 820–830. Curran Associates, Inc., 2018.

[52] David G. Lowe. Object recognition from local scale-invariant features. In *Proceedings of the IEEE International Conference on Computer Vision*, volume 2, pages 1150–1157. IEEE, 1999.

[53] Kevin Mackie and Božidar Stojadinović. Probabilistic seismic demand model for california highway bridges. *Journal of Bridge Engineering*, 6(6):468–481, 2001.

[54] John B. Mander, Michael John Nigel Priestley, and Ro Park. Theoretical Stress-Strain Model for Confined Concrete. *Journal of Structural Engineering*, 114(8):1804–1826, sep 1988.

[55] Sujith Mangalathu. *Performance based grouping and fragility analysis of box-girder bridges in California*. PhD thesis, Georgia Institute of Technology, 2017.

[56] Robin K McGuire. Probabilistic seismic hazard analysis and design earthquakes: closing the loop. *Bulletin of the Seismological Society of America*, 85(5):1275–1284, 1995.

[57] Frank McKenna. OpenSees: A framework for earthquake engineering simulation. *Computing in Science Engineering*, 13(4):58–66, July 2011.

[58] Sami Megally, Pedro F. Silva, and Frieder Seible. Seismic Response of Sacrificial Shear Keys in Bridge Abutments. Technical Report SSRP–2001/23, University of California, San Diego, San Diego, CA, 2001.

[59] Branislav Mičušík and Jana Košecká. Piecewise planar city 3D modeling from street view panoramic sequences. *2009 IEEE Computer Society Conference on Computer Vision and Pattern Recognition Workshops, CVPR Workshops 2009*, 2009 IEEE:2906–2912, 2009.

[60] Jack Moehle and Gregory G. Deierlein. A framework methodology for performance-based earthquake engineering. In *Proceedings of the 13th World Conference on Earthquake Engineering*, pages 3812–3814, 2004.

[61] Susendar Muthukumar. *A Contact Element Approach with Hysteresis Damping for the Analysis and Design of Pounding in Bridges*. PhD thesis, Georgia Institute of Technology, 2003.

[62] Ansgar Neuenhofer and Filip C. Filippou. Evaluation of Nonlinear Frame Finite-Element Models. *Journal of Structural Engineering*, 123(7):958–966, 1997.

[63] Joachim Niemeyer, Franz Rottensteiner, and Uwe Soergel. Contextual classification of lidar data and building object detection in urban areas. *ISPRS Journal of Photogrammetry and Remote Sensing*, 87:152–165, 2014.

[64] Xiaojuan Ning, Xiaopeng Zhang, Yinghui Wang, and Marc Jaeger. Segmentation of architecture shape information from 3D point cloud. In *8th International Conference on Virtual Reality Continuum and its Applications in Industry*, pages 127–132, Yokohama, Japan, 2009.

[65] State of California Department of Transportation. *Caltrans Seismic Design Criteria Version 2.0*. Caltrans, 2019.

[66] American Association of State Highway and Transportation Officials. *AASHTO LRFD Bridge Design Specifications*. American Association of State Highway and Transportation Officials, Washington, DC, 8 edition, 2017.

[67] OpenStreetMap contributors. Planet dump retrieved from https://planet.osm.org . `https://www.openstreetmap.org`, 2019.

[68] Jamie E Padgett, Bryant G Nielson, and Reginald DesRoches. Selection of optimal intensity measures in probabilistic seismic demand models of highway bridge portfolios. *Earthquake Engineering & Structural Dynamics*, 37(5):711–725, 2008.

[69] Mark D. Petersen, Morgan P. Moschetti, Peter M. Powers, Charles S. Mueller, Kathleen M. Haller, Arthur D. Frankel, Yuehua Zeng, Sanaz Rezaeian, Stephen C. Harmsen, Oliver S. Boyd, Ned Field, Rui Chen, Kenneth S. Rukstales, Nicolas Luco, Russell L. Wheeler, Robert A. Williams, and Anna H. Olsen. Documentation for the 2014 Update of the United States National Seismic Hazard Maps. Technical report, U.S. Geological Survey, Reston, VA, 2014.

[70] Sandor Popovics. A numerical approach to the complete stress-strain curve of concrete. *Cement and Concrete Research*, 3(5):583–599, sep 1973.

[71] Michael John Nigel Priestley, Frieder Seible, and Gian Michele Calvi. *Seismic Design and Retrofit of Bridges*. John Wiley and Sons, New York, NY, 1996.

[72] Charles R. Qi, Li Yi, Hao Su, and Leonidas J. Guibas. PointNet++: Deep Hierarchical Feature Learning on Point Sets in a Metric Space. In *31st Conference on Neural Information Processing Systems (NIPS 2017)*, Long Beach, CA, 2017.

[73] R. Qi, Charles, Hao Su, Mo Kaichun, and Leonidas J. Guibas. PointNet: Deep Learning on Point Sets for 3D Classification and Segmentation. In *2017 IEEE Conference on Computer Vision and Pattern Recognition (CVPR)*, pages 77–85, Honolulu, HI, jul 2017. IEEE.

[74] Tahir Rabbani, Frank A. Van Den Heuvel, and George Vosselman. Segmentation of Point Clouds Using Smoothness Constraint. In *The International Archives of the Photogrammetry, Remote Sensing and Spatial Information Sciences*, volume 36-5, pages 248–253, Dresden, Germany, 2006.

[75] Marie-Julie Rakotosaona, Vittorio La Barbera, Paul Guerrero, Niloy J. Mitra, and Maks Ovsjanikov. PointCleanNet : Learning to Denoise and Remove Outliers from Dense Point Clouds. *Computer Graphics Forum*, pages 1–19, jun 2019.

[76] Karthik Ramanathan, Jamie E. Padgett, and Reginald DesRoches. Temporal evolution of seismic fragility curves for concrete box-girder bridges in California. *Engineering Structures*, 97:29–46, aug 2015.

[77] Karthik Narayan Ramanathan. *Next Generation Seismic Fragility Curves for California Bridges Incorporating the Evolution in Seismic Design Philosophy*. PhD thesis, Georgia Institute of Technology, 2012.

[78] Ellen M. Rathje, Clint Dawson, Jamie E. Padgett, Jean-Paul Pinelli, Dan Stanzione, Ashley Adair, Pedro Arduino, Scott J. Brandenberg, Tim Cockerill, Charlie Dey, Maria Esteva, Fred L. Haan Jr, Matthew Hanlon, Ahsan Kareem, Laura Lowes, Stephen Mock, and Gilberto Mosqueda. DesignSafe: New Cyberinfrastructure for Natural Hazards Engineering. *Natural Hazards Review*, 18(3):06017001, 2017.

[79] Radu Bogdan Rusu and Steve Cousins. 3D is here: Point Cloud Library (PCL). In *2011 IEEE International Conference on Robotics and Automation*, pages 1–4. IEEE, may 2011.

[80] Aparajithan Sampath and Jie Shan. Segmentation and reconstruction of polyhedral building roofs from aerial lidar point clouds. *IEEE Transactions on Geoscience and Remote Sensing*, 48(3 Part 2):1554–1567, 2010.

[81] Jonathan Sauder and Bjarne Sievers. Self-Supervised Deep Learning on Point Clouds by Reconstructing Space, jan 2019.

[82] Alena Schmidt, Joachim Niemeyer, Franz Rottensteiner, and Uwe Soergel. Contextual classification of full waveform lidar data in the wadden sea. *IEEE Geoscience and Remote Sensing Letters*, 11(9):1614–1618, 2014.

[83] Anoosh Shamsabadi, Kyle M Rollins, and Mike Kapuskar. Nonlinear Soil-Abutment-Bridge Structure Interaction for Seismic Performance-Based Design. *Journal of Geotechnical and Geoenvironmental Engineering*, 133(6):707–720, 2007.

[84] Roman Shapovalov, Er Velizhev, and Olga Barinova. Nonassociative markov networks for 3d point cloud classification. The. In *The International Archives of the Photogrammetry, Remote Sensing and Spatial Information Sciences*, volume 38, Part 3, pages 103–108, 2010.

[85] Pedro F. Silva, Sami Megally, and Frieder Seible. Seismic Performance of Sacrificial Exterior Shear Keys in Bridge Abutments. *Earthquake Spectra*, 25(3):643–664, aug 2009.

[86] Southern California Association of Governments. Regional Transportation Plan, 2019.

[87] Jonathan P. Stewart, David M. Boore, Emel Seyhan, and Gail M. Atkinson. NGA-West2 equations for predicting vertical-component PGA, PGV, and 5%-damped PSA from shallow crustal earthquakes. *Earthquake Spectra*, 32(2):1005–1031, 2016.

[88] Jonathan P. Stewart, Ertugrul Taciroglu, John W. Wallace, Eric R. Ahlberg, Anne Lemnitzer, Changsoon Rha, Payman Khalili Tehrani, Steve Keowen, Robert L. Nigh-bor, and Alberto Salamanca. Full Scale Cyclic Testing of Foundation Support Systems for Highway Bridges. Part II: Abutment Backwalls. Technical Report UCLA-SGEL 2007/02, University of California, Los Angeles, Los Angeles, CA, 2007.

[89] Yujing Sun, Scott Schaefer, and Wenping Wang. Denoising point sets via L0 minimization. *Computer Aided Geometric Design*, 35-36:2–15, mar 2015.

[90] E. M. Thompson, D. J. Wald, and C. B. Worden. A VS30Map for California with geologic and topographic constraints. *Bulletin of the Seismological Society of America*, 104(5):2313–2321, 2014.

[91] Vasily V. Titov and Frank I. Gonzalez. Implementation and testing of the method of splitting tsunami (MOST) model. Technical report, NOAA/Pacific Marine Environmental Laboratory, Seattle, WA, 1997.

[92] Philip H.S. Torr and Andrew Zisserman. MLESAC: A new robust estimator with application to estimating image geometry. *Computer Vision and Image Understanding*, 78(1):138–156, 2000.

[93] Bill Triggs, Philip F. McLauchlan, Richard I. Hartley, and Andrew W. Fitzgibbon. Bundle Adjustment – A Modern Synthesis. In *Lecture Notes in Computer Science (including subseries Lecture Notes in Artificial Intelligence and Lecture Notes in Bioinformatics)*, volume 1883, pages 298–372. Springer Verlag, 2000.

[94] Shimon Ullman. The interpretation of structure from motion. *Proceedings of the Royal Society of London. Series B, Containing papers of a Biological character. Royal Society*, 203(1153):405–426, 1979.

[95] USGS. Shuttle Radar Topography Mission (SRTM) 1 Arc-Second Global. `http://dx.doi.org/10.5066/F7PR7TFT`, 2015.

[96] Dimitrios Vamvatsikos and C. Allin Cornell. Incremental dynamic analysis. *Earthquake Engineering & Structural Dynamics*, 31(3):491–514, mar 2002.

[97] Anh Vu Vo, Linh Truong-Hong, Debra F. Laefer, and Michela Bertolotto. Octree-based region growing for point cloud segmentation. *ISPRS Journal of Photogrammetry and Remote Sensing*, 104:88–100, jun 2015.

[98] George Vosselman, Ben G. H. Gorte, George Sithole, and Tahir Rabbani. Recognising Structure in Laser Scanner Point Clouds. In *The International Archives of the Photogrammetry, Remote Sensing and Spatial Information Sciences*, volume 36-8/W2, pages 33–38, 2004.

[99] David J. Wald, Kishor S. Jaiswal, Douglas B. Bausch, and Michael G. Hearne. PAGER — Rapid Assessment of an Earthquake's Impact. Technical Report U.S. Geological Survey Fact Sheet 2010–3036, U.S. Geological Survey, Golden, CO, 2010.

[100] Sara B. Walsh, Daniel J. Borello, Burcu Guldur, and Jerome F. Hajjar. Data Processing of Point Clouds for Object Detection for Structural Engineering Applications. *Computer-Aided Civil and Infrastructure Engineering*, 28(7):495–508, aug 2013.

[101] Michael Wand, Alexander Berner, Martin Bokeloh, Philipp Jenke, Arno Fleck, Mark Hoffmann, Benjamin Maier, Dirk Staneker, Andreas Schilling, and Hans Peter Seidel. Processing and interactive editing of huge point clouds from 3D scanners. *Computers and Graphics (Pergamon)*, 32(2):204–220, apr 2008.

[102] Jun Wang, Kai Xu, Ligang Liu, Junjie Cao, Shengjun Liu, Zeyun Yu, and Xianfeng David Gu. Consolidation of Low-quality Point Clouds from Outdoor Scenes. *Computer Graphics Forum*, 32(5):207–216, aug 2013.

[103] Miao Wang and Yi-Hsing Tseng. Incremental segmentation of lidar point clouds with an octree-structured voxel space. *The Photogrammetric Record*, 26(133):32–57, mar 2011.

[104] David W. Wanik, Emmanouil N. Anagnostou, Marina Astitha, Brian M. Hartman, Gary M. Lackmann, Jaemo Yang, Diego Cerrai, Jichao He, and Maria E. B. Frediani. A Case Study on Power Outage Impacts from Future Hurricane Sandy Scenarios. *Journal of Applied Meteorology and Climatology*, 57(1):51–79, jan 2018.

[105] David E. Wildasin. Disasters: Issues for State and Federal Government Finances. Institute for Federalism & Intergovernmental Relations working paper, 2006.

[106] Junhao Xiao, Jianhua Zhang, Benjamin Adler, Houxiang Zhang, and Jianwei Zhang. Three-dimensional point cloud plane segmentation in both structured and unstructured environments. *Robotics and Autonomous Systems*, 61(12):1641–1652, dec 2013.

[107] Cheng Yi, Yuan Zhang, Qiaoyun Wu, Yabin Xu, Oussama Remil, Mingqiang Wei, and Jun Wang. Urban building reconstruction from raw LiDAR point data. *CAD Computer Aided Design*, 93:1–14, dec 2017.

[108] Maciej Zamorski, Maciej Zięba, Piotr Klukowski, Rafał Nowak, Karol Kurach, Wojciech Stokowiec, and Tomasz Trzciński. Adversarial Autoencoders for Compact Representations of 3D Point Clouds, nov 2018.

[109] Liqiang Zhang, Zhuqiang Li, Anjian Li, and Fangyu Liu. Large-scale urban point cloud labeling and reconstruction. *ISPRS Journal of Photogrammetry and Remote Sensing*, 138:86–100, feb 2018.

[110] Qian Yi Zhou and Ulrich Neumann. Fast and extensible building modeling from airborne LiDAR data. In *GIS: Proceedings of the ACM International Symposium on Advances in Geographic Information Systems*, pages 43–50, 2008.

[111] Qian Yi Zhou and Ulrich Neumann. 2.5D dual contouring: A robust approach to creating building models from aerial LiDAR point clouds. *Lecture Notes in Computer Science (including subseries Lecture Notes in Artificial Intelligence and Lecture Notes in Bioinformatics)*, 6313 LNCS(Part 3):115–128, 2010.